

Inaugural dissertation
for
obtaining the doctoral degree
of the
Combined Faculty of Mathematics, Engineering and Natural Sciences
of the
Ruprecht – Karls – University
Heidelberg

presented by
M.Sc. Miriam Lisa Schäfer
born in Heidelberg, Germany
Oral examination: 07.11.2022

Interactome and proteome studies

**reveal new insights into the impact of a MnPV infection on the host
cell and subsequent viral carcinogenesis**

Referees:

Prof. Dr. Martin Müller

Prof. Dr. Frank Rösl

Eidesstattliche Erklärung

Ich erkläre hiermit, dass ich die vorliegende Dissertation selbst verfasst und mich keiner anderen als der von mir ausdrücklich bezeichneten Quellen und Hilfsmittel bedient habe. Diese Dissertation wurde in dieser oder anderer Form weder bereits als Prüfungsarbeit verwendet noch einer anderen Fakultät als Dissertation vorgelegt. An keiner anderen Stelle ist ein Prüfungsverfahren beantragt.

Heidelberg,

Miriam Lisa Schäfer

Für Papa

Table of Content

Zusammenfassung der Arbeit	1
Summary of the work.....	2
1 Introduction.....	3
1.1 Mucosal and cutaneous papillomaviruses.....	3
1.2 Genome organization and life cycle of HPV	4
1.3 The two oncoproteins E6 and E7.....	8
1.4 The promotion of the development of non-melanoma skin cancer (NMSC) by cutaneous HPVs	11
1.5 The preclinical animal model <i>Mastomys coucha</i>	12
1.6 Aims of the study	15
2 Results	16
2.1 Proteomic studies reveal insights into virus-host interactions.....	17
2.2 Semi-spatial proteomics of <i>Mastomys coucha</i> tumor tissue reveal strong differences on the entire proteome when compared to uninfected skin control	17
2.2.1 MnPV-infected areas within a tumor display weaker expression of differentiation marker keratin 10 compared to uninfected areas.....	25
2.3 <i>In vitro</i> proteomics provides new insights into the interplay between MnPV and host cells	26
2.3.1 <i>In vitro</i> proteomics using infected murine keratinocytes.....	26
2.3.2 Wwp2 and Cullin7 are downregulated in the presence of MnPVE7	32
2.3.3 HPV38 oncoprotein-expressing keratinocytes.....	33
2.4 Interactome studies uncover host cellular interaction partners of cutaneous PVs oncoproteins	37
2.4.1 BioID for MnPV and cutaneous HPV38 oncoproteins.....	37
2.4.2 Analysis of the interactome of the two oncoproteins MnPV E6 and E7 using IP	41
2.5 Deeper understanding of the influence of MnPV oncoproteins on the host cell - Investigation of the influence of MnPV on the HIPPO signaling pathway.....	44
2.5.1 PtpN14 reduction under the influence of PVE7	44
2.5.2 Downstream effects of PtpN14 downregulation- Investigating the localization of Yap/Taz.....	45
3 Summary of results.....	47
4 Discussion	48
4.1 Proteomic analyses provide new in-depth insights into the virus-host cell interplay of MnPV	49

4.1.1	Proteomic analyses of MnPV-infected cells provide insights into canonical pathways which are altered by infection.....	52
4.1.2	The expression of MnPV and HPV38 oncoproteins affects the entire host cell proteome	53
4.2	Interactome analyses of MnPV and HPV38 oncoproteins reveal interaction sites of oncoproteins with cellular proteins	57
4.2.1	Confirmation of MnPVE6 interaction with Maml1 and newly discovered interaction with Smad2/3.....	58
4.2.2	PtpN14 is a novel discovered interaction partner of MnPVE7.....	60
4.3	Influence of MnPVE7 on the HIPPO pathway through the binding to PtpN14	61
5	Summary of the Discussion.....	66
6	Material.....	67
6.1	Chemicals and reagents.....	67
6.2	Reagents for Bacteria Cultivation	69
6.3	Reagents for cell culture	69
6.4	Kits	70
6.5	DNA and protein size markers	70
6.6	Universal enzymes	71
6.7	Restriction enzymes.....	71
6.8	Consumables.....	71
6.9	Laboratory equipment.....	72
6.10	Cell lines.....	74
6.11	Bakteria.....	75
6.12	Oligonucleotides	76
6.13	Plasmids	77
6.14	Antibodies	79
6.15	Software, programs and bioinformatic tools	81
7	Methods.....	82
7.1	Cultivation and treatment of cells	82
7.1.1	Cultivation of cell lines.....	82
7.1.2	Passaging and seeding of cells	82
7.1.3	Counting of cells.....	83
7.1.4	Cryopreservation and thawing of cells	83
7.1.5	Transient transfection	83

7.1.6	Lentivirus production and transduction of NOK cells, MaFi132 and 308 keratinocytes ..	83
7.1.7	Verification of transduction.....	84
7.1.8	Generation of MnPV infected 308 keratinocytes	84
7.2	Cloning and Analysis of Oligonucleotides.....	85
7.2.1	RNA Extraction from cells.....	85
7.2.2	Reverse transcription of RNA	86
7.2.3	Semi-quantitative polymerase chain reaction.....	87
7.3	Protein extraction.....	87
7.3.1	Protein extraction from cells	87
7.3.2	Nuclear/ cytosol protein extraction from cells.....	88
7.3.3	Protein extraction from FFPE Tissue	89
7.4	Quantification of protein concentration by Bradford assay.....	90
7.5	Protein separation and visualization	91
7.5.1	SDS- PAGE.....	91
7.5.2	Western Blot.....	92
7.5.3	Immunofluorescence (IF).....	92
7.5.4	Immunohistochemistry (IHC)	93
7.6	Protein-protein interaction studies	94
7.6.1	BioID	94
7.6.2	Immunoprecipitation (IP)	95
7.7	Protein purification.....	95
7.7.1	Streptavidin Pull down	95
7.7.2	Protein purification using SP3-method	96
7.7.3	Peptide analysis using mass spectrometry analysis.....	96
7.8	Visualization of MnPV DNA by <i>In-situ</i> hybridization (ISH)	97
8	Supplemental Figures.....	99
9	Supplemental Tables	101
10	List of Figures	105
11	List of Tables.....	107
12	References.....	108
13	Abbreviation	122
14	Danksagungen	124

Zusammenfassung der Arbeit

Nicht-melanozytärer-Hautkrebs (Non-Melanoma Skin Cancer, NMSC) ist die häufigste bösartige Erkrankung in der hellhäutigen Bevölkerung und stellt insbesondere für Empfänger von Organtransplantaten sowie für Patienten, die an *Epidermodysplasia verruciformis* leiden eine enorme Einschränkung der Lebensqualität dar. Epidemiologische Studien belegen eine Rolle der humanen Papillomviren (HPV) bei der Entstehung von NMSC. In der hier vorgelegten Studie wird die Afrikanische Vielzitzenmaus *Mastomys coucha*, welche auf natürliche Weise mit dem wirtsspezifischen *Mastomys natalensis* Papillomavirus (MnPV) infiziert ist, als präklinisches Modellsystem verwendet. Es ist bereits bekannt, dass MnPV zusammen mit UV Licht durch einen „Hit-and-Run“ Mechanismus an der Ausbildung von NMSC in *Mastomys* beteiligt ist. Bislang war jedoch unbekannt, welche Prozesse in der Zelle diesem Effekt zugrunde liegen.

Im Rahmen der hier vorgestellten Arbeit wurden neue Einblicke in das Zusammenspiel zwischen MnPV und der Zielzelle aufgedeckt. So wurden erstmals Proteome verschiedener NMSC Subtypen im Kontext der Tumorerogenität räumlich verordnet und analysiert. Hier ergaben sich große Unterschiede in den Proteinexpressionsmustern der einzelnen Subtypen. Dies lieferte neue und tiefgreifende Einblicke in die inter- und intratumorale Heterogenität von NMSCs. Zudem konnten durch, basierend auf *in vitro* Proteom Studien, der Einfluss von MnPV Onkoproteinen auf Signaltransduktionswege verschiedenster zelluläre Prozesse gezeigt werden. Interaktomstudien ergaben mehrere wirtszelluläre Interaktoren der MnPV-Onkoproteine E6 und E7. Dabei konnten bereits bekannte Bindungspartner (Mam1 von MnPVE6) bestätigt, aber auch neue Interaktionspartner wie Smad2/3 (MnPVE6) und PtpN14 (MnPVE7) erstmals beschrieben werden. Mithilfe eines Top-Down-Ansatzes wurde in MnPV-infizierten Zellsystemen eine Wirkung von MnPV auf den HIPPO-Signalweg beobachtet. In einem weiteren *in vitro* System konnte dieser Effekt auf das Onkoprotein E7 zurückgeführt werden, welches sich reduzierend auf die Expression von PtpN14, eine zum HIPPO-Signalweg gehörende Phosphatase, auswirkt. Die Haupteffektoren dieses Signalweges Yap/Taz, wurden in MnPVE7- und MnPVE6E7-exprimierenden Zellen aufgrund der verringerten PtpN14 Expression verstärkt in den Zellkern verlagert. Dieser Effekt konnte im Rahmen dieser Arbeit zum ersten Mal für einen kutanen PV-Typ gezeigt werden.

Zusammenfassend zeigt diese Arbeit neue Erkenntnisse über die Interaktion zwischen MnPV und der Wirtszelle. Diese Aspekte einer kutanen PV-Infektion stellen interessante, neue Ansatzpunkte für die weitere Untersuchung der Genese von NMSCs dar.

Summary of the work

Non-melanoma skin cancer (NMSC) is the most common malignancy in the fair-skinned population and represents a tremendous limitation in the quality of life, especially for organ transplant recipients and in patients suffering from *Epidermodysplasia verruciformis*. Epidemiological studies support a role of human papillomavirus (HPV) in the development of NMSC. In the study presented here, the African multimammate mouse *Mastomys coucha*, which is naturally infected with the host-species specific *Mastomys natalensis* papillomavirus (MnPV), is used as a preclinical model system. It is already known that MnPV, together with UV light, is involved in the formation of NMSC in *Mastomys* through a "hit-and-run" mechanism. However, until now it was unknown which processes in the cell underlie this effect.

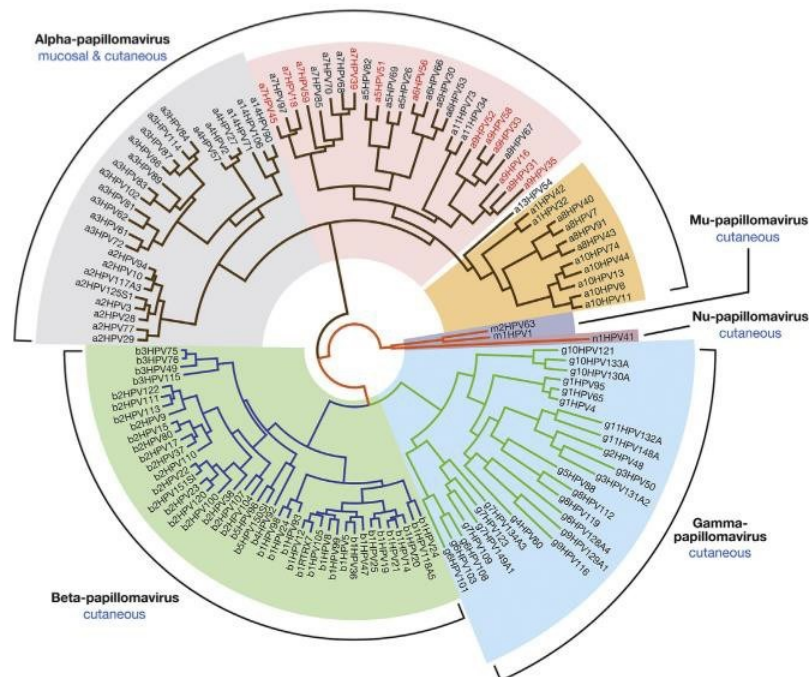
In the work presented here, new insights into the interplay between MnPV and the target cell were uncovered. Thus, for the first time, spatial proteomes of different NMSC subtypes were analyzed in the context of tumor heterogeneity. Here, large differences in protein expression patterns between subtypes emerged. This provides novel and profound insights into the inter- and intra-tumor heterogeneity of NMSCs. Moreover, based on *in vitro* proteomic studies, the influence of MnPV oncoproteins on signal transduction pathways of diverse cellular processes could be demonstrated. Interactome studies revealed several host cellular interactors of the MnPV oncoproteins E6 and E7. Previously known binding partners (Mam11 of MnPVE6) were confirmed but also new interaction partners such as Smad2/3 (MnPVE6) and PtpN14 (MnPVE7) were described for the first time. Using a top-down approach, an effect of MnPV on the HIPPO pathway was observed in MnPV-infected cell systems. In another *in vitro* system, this effect could be attributed to the oncoprotein E7, which has a reducing effect on the expression level of PtpN14, a phosphatase belonging to the HIPPO pathway. The main effectors of this signaling pathway Yap/Taz, were increasingly translocated to the nucleus in MnPVE7- and MnPVE6E7-expressing cells due to reduced PtpN14 expression. This effect was demonstrated for the first time for a cutaneous PV type in this work.

In summary, this work reveals new insights into the interaction between MnPV and the host cell. These aspects of cutaneous PV infection represent interesting new starting points for further investigation of the genesis of NMSCs.

1 Introduction

1.1 Mucosal and cutaneous papillomaviruses

Papillomaviruses (PVs) are non-enveloped double-stranded DNA viruses with a genome size of approximately 8 kb. To date, more than 400 PVs have been described infecting multiple different animals like fish, reptiles, birds and mammals [10, 11]. Over 200 of these papillomaviridae infect humans (HPV) [12]. Based on differences in the L1 genes, they are classified into five different groups (alpha-, beta-, gamma-, nu-, and mu- papillomavirus, respectively) which is shown in the Figure 1 as a phylogenetic tree [7]. The alpha genus can be subdivided into high-risk types (e.g., HPV16, 18, 31, 33, 45, 58) and low-risk types (e.g., HPV6, 11). While infection with low-risk types is associated with genital warts, the infection with high-risk HPVs can be found in 99% of cervical cancers and other cancers like head-and-neck cancer as well as penile, vulvar, and vaginal cancer [13]. Prophylactic vaccines against high-risk alpha types have been available since 2006. After consequential implementation of vaccination programs, the rate of HPV-induced cancers has already been significantly minimized [14, 15].



Introduction

The cutaneous types of the beta and gamma genera can infect cutaneous epithelia. Genus beta contains 54 HPV types, which can be subdivided into five different species [16]. BetaHPV infections occur in the entire human population [17-19]. Serological studies showed that 52% of the Dutch and 67% of the Italian population had already been exposed to an infection in their lifetime [19]. Initial infection can already be detected in young children and a similar distribution of subtypes can be found within a family, suggesting infection through skin-to-skin contact within the family [20-22]. DNA of the cutaneous types is detected in hair follicle stem cells, which serve as a reservoir for the viruses [23, 24].

Cutaneous squamous cell carcinoma (SCC) are particularly common in immunosuppressed patients (e.g. organ transplant recipients) [25, 26] as well as in patients with the rare hereditary disease *Epidermodysplasia verruciformis* (EV). In particular, HPV 5 and 8 were isolated from SCCs of EV patients. Due to their oncogenic potential, these beta types belonging to species $\beta 1$ are also referred to as high-risk cutaneous types [27].

1.2 Genome organization and life cycle of HPV

The HPV genome codes for six early proteins (E1, E2, E4, E5, E6, and E7), while cutaneous PV lack the E5 gene. The two structural late proteins (L1 and L2) finally, form the capsid [7] (Figure 2). The early proteins E1 and E2 are mainly responsible for viral replication and viral gene expression. They are able to bind to the upstream regulatory region (URR), which is located within the HPV genome between the early gene E6 and the late L1 gene [28, 29]. Host cellular transcription factors can also bind to this site and thus influence the expression of viral genes. E4 causes virion release by perturbing the cyokeratin network [30]. E5 can inhibit the immune response by modulating the antigen presentation as well as inflammatory pathways [31, 32]. The two oncoproteins E6 and E7 prevent bind to tumor suppressors and are able to enhance host cell proliferation. The viral capsid consists of 72 capsomers each formed by pentamers of L1 proteins and stabilized by disulfide bonds and calcium ions [33]. Transcription of viral genes starts at an early promoter located within a locus control region (LCR) (early genes) or from the late promoter located in the E7 ORF (late genes) [7]. The differentiation status of the host cell is the decisive factor which promoter is used. This allows differential expression of the viral proteins in the different skin layers [7, 34, 35].

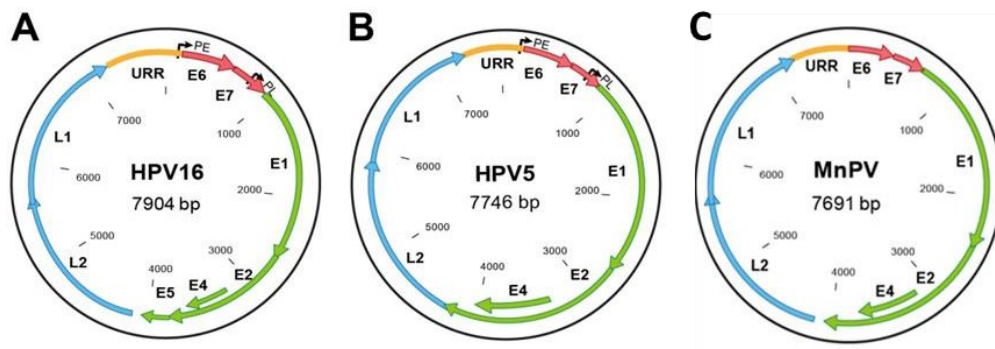


Figure 2: Schematic genome organization of HPVs and MnPV. A) HPV16 as an example for mucosal alpha types contains an E5 ORF. B) HPV5, a cutaneous beta-HPV, lacks the E5 ORF. C) Like cutaneous HPVs, MnPV lacks the E5 ORF. The picture was adapted from: [2]

The PV lifecycle completely depends on the host cell differentiation. The term differentiation refers to a developmental process in which cells acquire the ability to change their phenotype and take on a more specialized function [36]. Differentiation processes take place in the skin, for example, where they enable continuous renewal of the epidermis. This contributes to the function of the skin as a barrier to the environment as well as to wound healing.

Differentiation is subject to a strictly regulated process: both intrinsic factors such as the genetic background (precursor cells) and extrinsic factors such as hormones and the microenvironment of the cells play an important role in the homeostasis [37, 38]. Epidermal cells develop from stem cells in the basal layer (*stratum basale*) to the suprabasal epidermal layers (*stratum spinosum* and *stratum lucidum*), which consist of differentiating cells. The uppermost layer of the skin, the *stratum corneum*, is formed by terminally differentiated and dead cells. In the skin, well-described differentiation markers indicate distinct degree of cellular differentiation levels. Certain keratins, e.g. keratin 10 (K10) [39] and keratin 14 (K14) [40], are expressed in differentiated epidermal layers, whereas involucrin [41], is expressed exclusively in the uppermost layer of the epidermis, allowing the identification of terminally differentiated areas of the skin [42]. Terminal differentiation begins when cells withdraw from the cell cycle and lose their ability to adhere to the basal membrane zone [43].

Observations in the context of cancer show that the differentiation process can be reversed and that malignant cells show a dedifferentiate phenotype [44]. The differentiation status of tumor cells is an important aspect in assessing their malignant potential and aggressiveness. In general, a high degree of differentiation indicates a better prognosis than a low degree [45]. Highly differentiated tumor tissue means that the neoplasm is morphologically similar to the original organ, while a low stage of

Introduction

differentiation indicates that cells are gradually losing their structural organization [45]. This has been shown in many tumor types such as neuroblastoma, prostate cancer and in SCC as in criterion for a more severe course of the disease [45-48].

Infection with HPV begins with virus entry into the basal epithelial layer through micro-injuries of the epithelium allowing HPV to access the single-layered basal keratinocytes. Papillomaviruses bind to heparan sulphate proteoglycans (HSPGs) on the cell surface of basal keratinocytes *via* their L1 capsid proteins. Binding of the virus to the target cell triggers a conformational change of the capsid, which is mediated by cyclophilin B. This conformational change exposes the N-terminus of the minor capsid protein L2, allowing the virus to enter the cell *via* furin cleavage-mediated endocytosis [49].

When the viral DNA enters the nucleus, viral gene expression is initiated [50]. The gene expression of papillomaviruses is closely linked to the differentiation state of its host cell [51]. Initially, the two early proteins E1 and E2 are activated, which amplify the viral genome [52]. E2, which contains a DNA-binding domain binds the URR of the viral genome and regulates PV gene expression. E2 also binds the viral DNA helicase E1 and recruits it to the viral origin of replication to initiate genome amplification[53]. The two proteins E1 and E2 are thus responsible for the viral genome replication at this stage [54].

In the late phase of HPV infection, E4 which is the most abundant transcript of PVs, is expressed by infected cells in the G2 phase in the upper epithelial layers [55]. The two capsid proteins L2 and L1 are subsequently produced and encapsulate the viral DNA, resulting in the formation of new infectious virus particles. The E4 protein is involved in the release of virions by facilitating the disintegration of cytokeratin filaments, thus enabling passive viral shedding [56].

The early protein E5 is absent in all cutaneous PVs. This oncoprotein of the subtype HPV16 for instance, has transforming properties in fibroblasts and keratinocytes [57-59]. It is thought to have

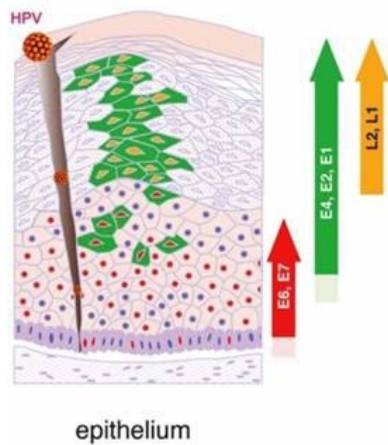


Figure 3: Protein expression map of high-risk mucosal HPVs. Oncoproteins E6 and E7 (red arrow) are expressed in the basal layer of the epidermis. E4, E2 and E1 (green arrow) are expressed in almost the whole epidermis. Capsid proteins L1 and L2 (yellow arrow) are regulated from the late promoter and expressed only in upper layers of the epidermis. Viral capsids are formed in the highest, almost keratinized areas. Figure adapted from: [3]

the ability to influence apoptosis [60] and intracellular trafficking [61, 62]. It is also able to suppress of the presentation of the viral antigen *via* the MHC-complex by downregulating its expression [32].

In high-risk PV, such as HPV16, amplified viral genomes persistent in initially infected keratinocytes. They are maintained and passed on as episomes to the daughter cells during cell division [63]. In high-risk types such as HPV16 and 18, many cellular processes have already been described that are influenced by the expression of the two oncoproteins E6 and E7, whereby these proteins play a central role in the impairment of cell homeostasis. These include, for example, cell proliferation, initiation of apoptosis and the retention of the cell in the cell cycle [11, 64, 65]. A schematic overview of the protein expression of mucosal HPV types is shown in Figure 3.

Introduction

1.3 The two oncoproteins E6 and E7

The oncogenic potential of the two proteins E6 and E7 was first described for HPV16 in 1986 [66]. Both have transforming properties in primary rodent cells [67, 68], making them key drivers in HPV-mediated cellular transformation.

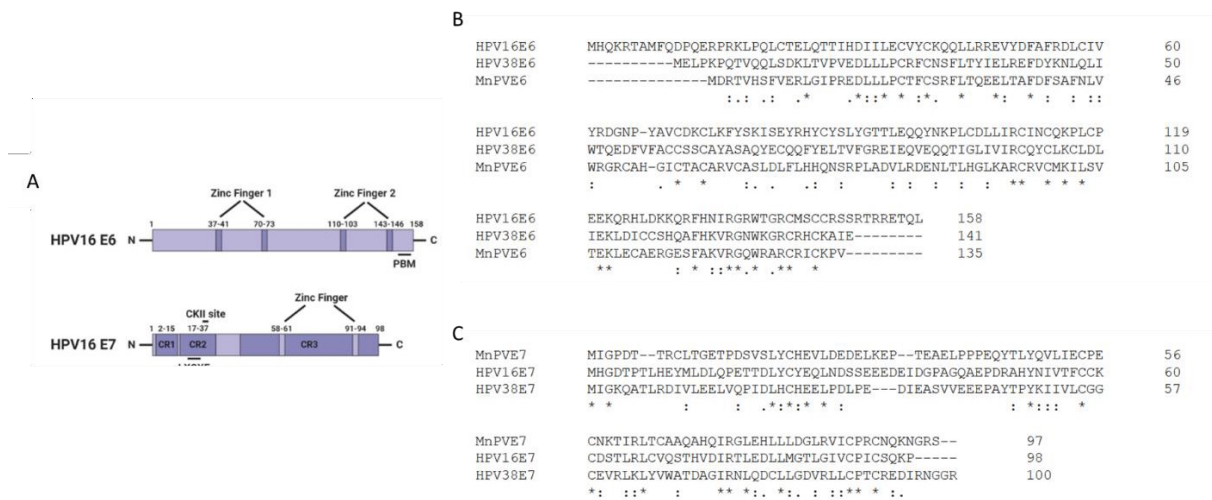


Figure 4: The two HPV oncoproteins E6 and E7. A) Schematic illustration of HPV16 oncoprotein structure. Numbers indicate amino acid position. CR: conserved region, TM: transmembrane domain, CKII: Casein kinase II. Figure adapted from: [1]. B) and C) show multiple sequence alignment of oncoprotein sequences of different PV types using CLUSTAL Omega. B) Alignment of HPV16 HPV38 and MnPV E6. C) Alignments of HPV16, HPV38 and MnPV E7 oncoproteins.

Immortalization of human keratinocytes is also enabled by the expression of these PV proteins [69-71], with co-expression of both genes, E6 and E7 together, necessary for the immortalization of these cells [71, 72]. The oncogenic potential of HPV16 E6 and E7 could also be demonstrated *in vivo*. Transgenic mice expressing HPV16 E6 and E7 under the control of the keratin14 promoter developed cervical tumors [69, 70]. Since the K14 promoter is active in the basal keratinocytes, these mice also developed skin tumors. Interestingly, HPV16 E7 appears to be the dominant oncogene in this system. Its expression was sufficient to lead to the formation of reproductive tract tumors in combination with estrogen treatment [73, 74]. However, this was not the case for HPV16 E6. Nevertheless, combined expression of both oncoproteins led to the formation of significantly larger tumors when compared to the tumors developed under the influence of E7 expression only [71, 72].

HPV16 E6 has several zinc finger domains, which are crucial for the oncogenic potential of the virus [75]. E7 is characterized by three different conserved regions (CR). CR1 and CR2 are homology domains and conserved between different HPV E7 proteins [76]. A schematic representation of these protein structures can be seen in Figure 4 A). Furthermore, Figure 4 B) and C) show the similarities and differences of these proteins between different PV types by alignment. If one compares different PV oncoproteins against each other, only a few sequential similarities can be found.

The expression of HPV16E7 can keep the cell in a proliferative stage by activating the G1/S-phase checkpoint of the host cells [64]. A transition into the differentiation phase of keratinocytes is thus bypassed, which favors viral replication in proliferative cells. In addition, it has already been extensively described that E7 of diverse HPVs can bind to the family of pocket proteins such as pRb, p107 and p130 [77]. This binding leads to conformational change of the pocket proteins, which results in the release of E2F transcription factors. The subsequent expression of cyclin A and cyclin E is thus increased and leads to the cell entering the S phase of the cell cycle [78]. It should be noted that the interactome of the respective oncoproteins and its effects on the host cell differ greatly between high- and low-risk HPVs. For example, both high and low risk HPV types show binding between E7 and the pocket protein Rb1, but there are strong differences in the binding affinity and the resulting effect. High-risk types are able to achieve proteasomal degradation of Rb1 through binding, while low-risk types bind but do not degrade Rb1 [79, 80].

E6 can target cell proteins and cause disturbances of cell homeostasis. To avoid induction of apoptosis, cells infected with the high-risk types HPV16 and 18 E6 oncoproteins can bind to the E3-ubiquitin ligase E6AP to induce proteasomal degradation of p53 [81]. In addition, E6 proteins of these HPV types can directly inhibit the transcriptional activity of p53 by binding to p300 [82]. The interaction of the two oncoproteins E6 and E7 can allow cell proliferation to continue and apoptosis initiation to be suppressed.

In addition, the expression of E6 was shown to influence the initiation of the host immune response. Interleukin 1 beta (IL-1 β), a proinflammatory cytokine involved in B- and T-cell activation and antibody production, is able to reduce UV-induced DNA damage [83]. Reduced expression allows UV-induced DNA damage to accumulate and may thus promote cancer formation. This cytokine is degraded in the presence of E6 which has been shown *in vivo* in a transgenic animal model with cutaneous HPV38E6 [84, 85]. Many studies show the mechanisms by which cutaneous HPVs are involved in skin carcinogenesis: Like high-risk HPVs, cutaneous types are also able to inhibit the function of p53

Introduction

through the functions of oncoprotein E6. However, this occurs *via* different mechanisms than in the high-risk types of the alpha genus [86]. For example, HPV38 has been shown to induce the expression of deltaNp73, an inhibitor of p53 [87]. In addition, E6 from beta-HPVs can indirectly disrupt DNA damage responses by reducing levels of cellular p300, ATM and ATR [88-91]. This allows p53 to initially accumulate in the cell, leading to a blockade of cell cycle progression [92].

In addition, E6 also plays an important role in apoptosis, which is induced by toxic UV radiation. In uninfected cells, toxic doses of UV radiation lead to perforation of the outer mitochondrial membrane, triggered by the pro-apoptotic protein Bak, followed by the activation of the caspase cascade and the initiation of apoptosis [93]. After UV exposure, E6 is able to bind Bak by promoting its degradation [94-96], thereby blocking the intrinsic apoptotic pathway. Its inhibition protects the cell from apoptosis allowing continued cell division and virus replication in these altered cells. In addition to E6, the second oncoprotein E7 also plays an important role in disrupting the cell homeostasis by arresting the cell cycle progression. E7 can bind to a region of the retinoblastoma protein (Rb) at a site essential for its function as a tumor suppressor [97, 98]. This binding occurs in high risk as well as in cutaneous PVs but it leads to different outcome. While high-risk HPV type 16 E7 binding to Rb leads to its degradation and in the following cell cycle progression, binding of HPV38 E7 does not lead to cell cycle progression [99]. Furthermore, expression of the HPV8 E7 leads to an increase in terminal differentiation and hyperproliferation, allowing dermal fibroblasts to migrate and invade the dermis [100]. In addition, keratinocytes expressing the complete early genomic region (CER) of HPV8 were shown to have a profound loss of CHK1 proteins, which are an important regulator of the cell cycle and DNA damage response [101]. The two junctional bridging proteins β -catenin and ZO-1 are strongly upregulated by the E7 oncoproteins of HPV5 and HPV8 in keratinocytes grown in organotypic skin cultures, which probably contributes to the oncogenic potential of these viruses [102].

Overall, HPV oncoproteins have demonstrated their ability to interfere with their host cell in a variety of ways to prolong the cell cycle, inhibit apoptosis, delay differentiation, and find ways to bypass the immune system of the host.

1.4 The promotion of the development of non-melanoma skin cancer (NMSC) by cutaneous HPVs

Non-melanoma skin cancer (NMSC) is the most common malignancy in the fair skinned population and can be classified into various subtypes [103]. The most common ones are basal cell carcinomas (BCC, approximately 80%) SCC (approximately 20%) [104]. SCCs are among the most frequent solid cancers in humans (Cancer Facts and Figures 2022, American Cancer Society). The precursor of these forms of skin cancer is actinic keratosis (AK). It is caused by long-term UV exposure and is the most common precancerous condition that forms on skin [105, 106]. Although mortality rate is quite low, the development of NMSC displays a big burden for the patients themselves. The combined charges for direct and indirect costs of occupational NMSC cases is \$28.9 million (\$15.9 million for BCC and \$13.0 million for SCC) in Canada in 2011 [107]. In Australia, the costs of care for NMSC in 2015 for the entire population was estimated to exceed AUD\$700 million [108]. In 1972, it was postulated that cutaneous HPVs might play a role in the development and progression of skin cancer [109]. Although UV radiation is considered as the main risk factor for SCC, the synergistic effect of HPV is still debated [110, 111]. An overview presentation of the risk factors for NMSC formation is shown in Figure 5.

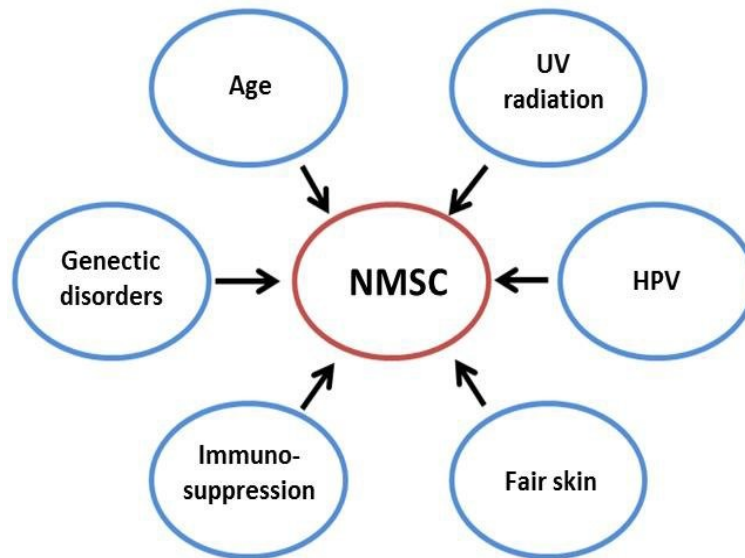


Figure 5: Risk factors for cutaneous squamous cell carcinoma (SCC). Figure modified from [6].

Epidemiological studies have found an association of SCCs and actinic keratosis (AKs) with certain HPV types [112, 113], which was also confirmed in a 2014 meta-study [114]. Nevertheless, the role of HPV infection in the development of SCCs is still not 100% clear due to the ubiquitous presence of

Introduction

cutaneous HPVs in the population [7, 115]. Furthermore, the absence of detectable HPV mRNA in SCCs also raises questions about its role in the development of NMSCs. While the viral DNA load in AKs is high, indicating productive infection, SCCs or metastases have only one copy of viral DNA in one or two thousand infected cells [116], which may suggest that viral DNA is lost during progression from precursors to SCC. Copy numbers of cutaneous HPVs in lesions are much higher when compared to normal skin [117, 118], and HPV genomes are frequently found in lesions of OTRs [119-122]. Therefore, it has been suggested that HPV infection may be important for the initiation but not the further development of NMSC [123], which is referred to as the "hit and run"-mechanism. Currently, cutaneous HPVs are thought to play a role in the development of SCC by promoting proliferation, preventing DNA repair and apoptosis, leading to an accumulation of mutations in host cell DNA and potential changes in cellular geno- and phenotype [124]. This needs to be proven in further studies to gain deeper insight into the specific virus- host cell relationship. As mentioned above, the development of SCC can be promoted by cutaneous HPVs, but the impact of the oncoproteins E6 and E7 on the development of the forementioned subtypes of SCC is not completely understood at this time and needs to be further investigated.

1.5 The preclinical animal model *Mastomys coucha*

The African multimammate rodent *Mastomys coucha* is a very attractive animal model system for the investigation of papillomaviruses. *Mastomys coucha* belongs, like *Mus musculus* to the family Muridae (Figure 6 A). They are distributed throughout sub-Saharan Africa. The animal samples used in this thesis, originate from the *Mastomys* colony of the German Cancer Research Center and are naturally and persistently infected with two different papillomaviruses [125, 126]. Additionally, samples from experimentally infected animals were used in this work [44]. The animals of the naturally infected colony are hosts of *Mastomys coucha* papillomavirus 2 (McPV2, pi genus), and *Mastomys natalensis* papillomavirus (MnPV), the latter will be the focus of the present study. The naming of the two viruses dates back to the 1970s. At that time *Mastomys coucha* was wrongly classified as *Mastomys natalensis*, which was revised decades later and henceforth the species *Mastomys natalensis* and *Mastomys coucha* were distinguished. These are morphologically very similar and can only be clearly discriminated on the basis of the number of chromosome sets. While *M. natalensis* has only 32 chromosomes, *M. coucha* has 36 [127].

Naturally MnPV-infected *Mastomys coucha* at the German Cancer Research Center spontaneously develop benign skin lesions compared to a virus-free colony housed in parallel after long-term UV-irradiation. These lesions can develop into SCCs (Figure 6 B and C) [44]. Etiologically, these lesions

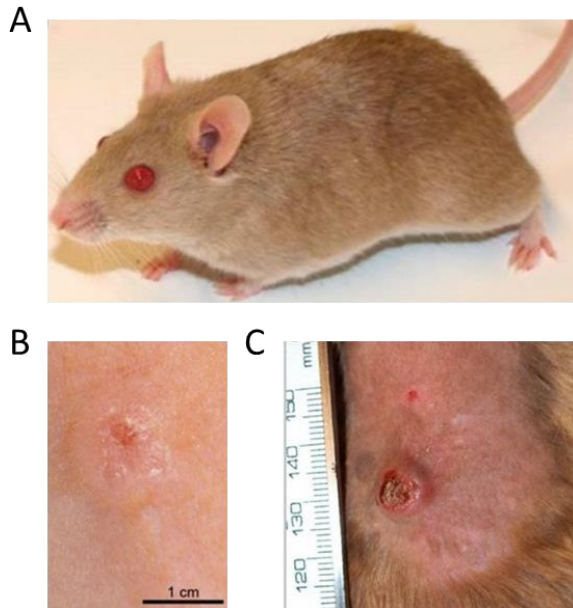


Figure 6: The preclinical animal model *Mastomys coucha*. **A)** Photo of an adult *Mastomys coucha* from our colony. **B)** and **C)** show UV-induced tumors of *Mastomys coucha*. The animals develop both dedifferentiated tumors (nKSCC) as shown in panel B and well-differentiated ones as shown in panel C (KSCC). Pictures modified from: [2]

were previously classified as "keratoacanthomas" or papillomas due to their similarity to human lesions [128-130]. Most of these keratoacanthomas occur on the trunk and head of *Mastomys*, especially around the ears and cheeks. In addition, the animals also develop lesions on the tongue and in the anogenital region, which correspond to human condylomas associated with the mucosal PV type McPV2 [131]. MnPV-infected *M. coucha* therefore show the same types of skin tumors found in patients. These are on the one hand the well-differentiated keratinized (KSCCs) and on the other the dedifferentiated non-keratinized SCCs (nKSCCs). The two tumor subtypes not only differ in their morphology but also in their overall MnPV load [44, 132]. The well-differentiated forms contain several thousand virus copies/cell, while dedifferentiated SCCs only contain an overall very low viral load with (< 1 copy/cell) Interestingly, a preceding MnPV-infection is serologically detectable [44] implicating, that MnPV acts under the control of a "hit-and run"-mechanism .

The genomes of both described *Mastomys* papillomaviruses, code for the late genes L1 and L2 as well as for the early genes E1, E2, E4, E6 and E7, but not for E5. This shows a further similarity to the cutaneous HPV types like HPV38 described above [84, 125, 133].

Introduction

Taken this together, *M. coucha* allow to follow the entire cycle of a PV infection (here MnPV) in its natural, immunocompetent host. This unique preclinical model is the only one available that is persistently infected with a genuine papillomavirus and mimics all aspects of human squamous cell carcinomas induced by UV light.

1.6 Aims of the study

The aim of this study was to describe the influence of MnPV on host cells. Anticipating a key role of PV oncogenes in cell transformation which can lead to the formation of premalignant skin lesions, the crosstalk between E6 and E7 with the host cell was investigated.

Therefore, the aims of the present study can be outlined as follows:

- To describe the spatial proteomes of NMSC subtypes from *Mastomys coucha*.
- The establishment of an appropriate cell system expressing MnPV and HPV38 E6 and E7 (as reference) to perform interactome and proteome studies to estimate global changes within the host cells caused by MnPV oncogenes.
- To identify potential targets deregulated by MnPV oncogene expression.
- To analyze individual deregulated candidates, to validate data and gain deeper knowledge of the underlying effect.
- To name host cellular pathways deregulated by MnPV infection and in particular oncoprotein expression which might serve as a complementing role to support MnPV-induced carcinogenesis.

2 Results

To better understand the role of MnPV in NMSC development, proteomic analyses and interactome studies were carried out. Through subsequent pathway analyses, new insights will be obtained, providing the basis for further investigations on this tumor entity.

For this purpose, the *in vivo* situation was examined by spatial proteome analysis of different SCC subtypes of *Mastomys coucha*. To enable a mechanistic analysis, additional *in vitro* studies investigated the influence of the expression of the entire MnPV genome as well as the expression of the two oncoproteins E6 and E7 in particular on the host cell proteome.

In addition, to obtain the overall network of molecular interactions of oncoproteins and host cell proteome, the interactomes of E6 and E7 of MnPV as well as HPV38 were constructed.

A schematic overview of the experiments and methods performed is shown in Figure 7.

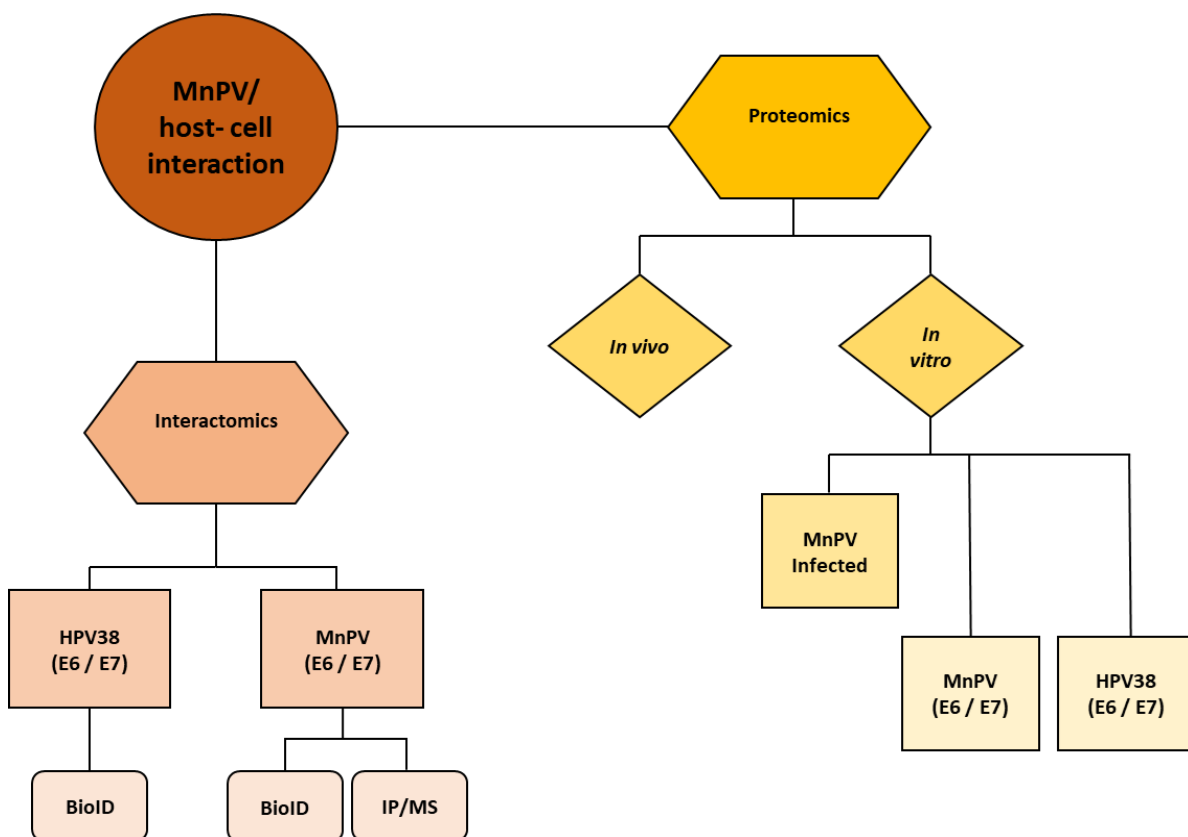


Figure 7: Schematic overview of experiments and methods performed within this thesis.

Please note that according to the commonly used gene/protein nomenclature for humans (see <https://www.genenames.org/>) and mouse (<https://rgd.mcw.edu/wg/species/mouse/>), in the following, the spelling of the protein/gene names differ according to the context, for instance *PTPN14* (human) or *PtpN14* (*Mastomys* or mouse).

2.1 Proteomic studies reveal insights into virus-host interactions

Proteomic studies used in this work are based on the powerful tool of mass spectrometry enabling insights into the virus-host interplay. Such analyses were never done so far and enabled to dissect protein networks and pathways affected by MnPV. To obtain information about the effects of MnPV infection *in vivo* analyses of different tissues were performed. The aim was to get global insight into pathways affected by MnPV, e.g., the disruption of differentiation processes of the host cells.

2.2 Semi-spatial proteomics of *Mastomys coucha* tumor tissue reveal strong differences on the entire proteome when compared to uninfected skin control

Semi-spatial proteomics of *Mastomys coucha* skin tumors were successfully established to distinguish between MnPV-infected and uninfected areas within one tumor. Immunofluorescence (IF) stainings against the viral E4 protein were performed *prior* to the dissection of the tumor tissue. The E4 protein is translated from the most abundant spliced transcript of MnPV, E1^ΔE4, and can be used as an infection marker, due to its high expression. A representative IF-staining of MnPV-infected tumor is shown in Figure 8.

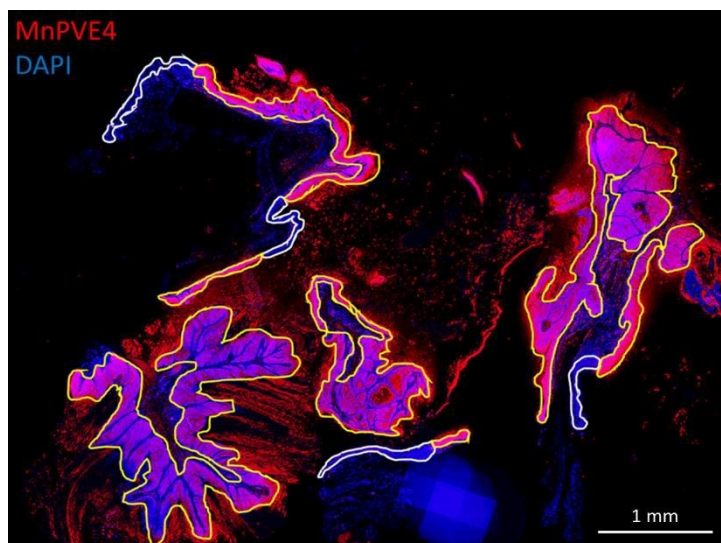


Figure 8: IF staining of a MnPV-positive *Mastomys* skin tumor. Areas outlined in yellow show MnPV-positive epidermal structures, while areas outlined in white are MnPV-negative. MnPVE4 serves as marker of infection (red). DAPI was used as nuclear marker (blue).

Results

In our model, spontaneously formed epithelial tumors but also different cSCCs subtypes under long-term UV irradiation and simultaneous MnPV-infection can be observed. These subtypes were either well-differentiated keratinized squamous cell carcinoma (KSCC) or dedifferentiated non-keratinized squamous cell carcinomas (nKSCC) [44]. The latter usually also harbor better differentiated areas in upper parts or the tumor, phenotypically similar to KSCCs, and transition zones to dedifferentiated lower areas. Figure 9 shows a HE staining of a representative tumor and its subsections of well-differentiated (red) and dedifferentiated (green) areas. MnPV-uninfected skin (blue) served as a control.

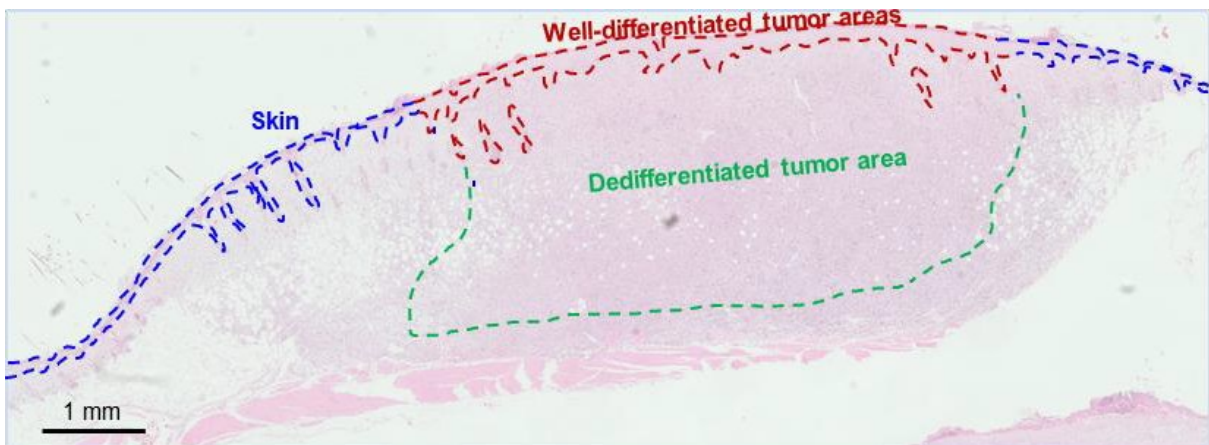


Figure 9: Exemplary HE stained nKSCC tumor to visualize the subdivision of micro-dissected areas.

The dissected FFPE tissue was analyzed to investigate differences in the proteomic profile of the abovementioned SCC subtypes of *Mastomys coucha* [44].

Care was taken to ensure that a minimum of 0.135 mm³ tissue was used as starting material, which was defined as the minimum tissue volume by dissecting tumor areas of different sizes, which were lysed and subsequently analyzed by western blotting. An illustration is shown in Supplemental Figure 1.

After the lysis of dissected tissue, SP3 purification [134], a bead-based, single-pot purification method for quality optimization of protein mixtures was performed. After SP3, samples have been handed over to the Genomics and Proteomics Core Facility of the DKFZ where they were trypsin digested and subsequently desalted. Resulting peptides were separated *via* analytical column and analyzed by a mass spectrometer.

Data analysis was carried out by MaxQuant (version 1.6.14.0). In total 13239 peptides and 2414 proteins could be identified by MS/MS based on an FDR cutoff of 0.01 on peptide level and 0.01 on protein level. Quantification was done using a label free quantification approach based on the MaxLFQ algorithm [135].

Principal component analysis (PCA) was performed to determine the frequency levels of the

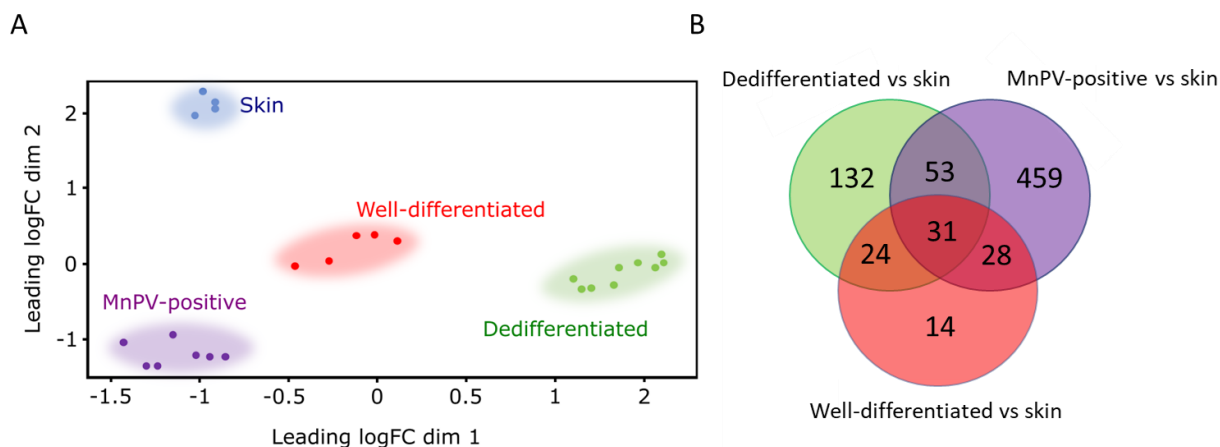


Figure 10: The analysis of the in vivo proteome results shows a successful application of the new method. A) PCA shows clear discrimination between the respective samples taken from both skin and tumor tissue. **B)** Venn diagram depicting a comparison of differentially expressed proteins found in tumor proteomes when compared to skin control.

characteristics in the different runs and to identify the main axes of frequency variation (Figure 10 A).

As can be seen from the PCA, the proteomes of well-differentiated tissues appear to have the highest similarity to the control skin as these clusters show great spatial proximity to each other. Dedifferentiated and MnPV-positive tissues, on the other hand, have large structural differences in the protein networks when compared to skin. Here, the spatial proximity appears larger in the PCA representation.

Comparing the measured signal intensities of all proteins quantified in the tumor sample with those from the skin control group reveals differences in the expression patterns. The amount of differentially expressed proteins in the tumor tissues in comparison to control skin can be illustrated in a Venn diagram (Figure 10 B).

The greatest similarity between the proteomes can be seen between skin and well-differentiated tissue. Here, only 97 proteins (shown in the Venn diagram as: $14 + 24 + 31 + 28$) with significantly

Results

different expression levels were found. Dedifferentiated tissues show greater differences in the proteomes compared to skin, a total of 240 proteins (shown in the Venn diagram as: 132 + 53 + 31 + 24) were found here. The common explanation for the development of dedifferentiated tumor tissue from well-differentiated precursors could be confirmed by these data. It is possible that in well-differentiated tissue additional driver mutations cause more aggressively proliferating and dedifferentiated tumor areas. MnPV infection also appeared to have a particularly substantial impact on the protein network, as a total of 571 proteins (shown in the Venn diagram as: 459 + 53 + 31 + 28) were differentially expressed when compared to control skin.

31 proteins could be found in all three tumor subtypes with significant different expression levels compared to skin. A list of proteins with strongest up- and downregulations for the different comparisons is shown in Supplemental Table 1.

Volcano plots were created to graphically illustrate the comparisons between the resulting data sets of the semi-spatial proteomics of *Mastomys* tissue (Figure 11). This type of representation allows a quick visual identification of the extent of the differences and their significance.

As depicted in the volcano plots, well-differentiated tissues and skin showed comparatively small differences in their proteomes. This is shown by only a few data points representing protein expression values that are far from the origin (0/0) (Figure 11 B). More pronounced differences could be seen when comparing the proteomes of dedifferentiated tissue and skin (Figure 11 C). However, the greatest difference is visualized by volcano blots between the skin and MnPV-infected tissues (Figure 11 A). This might be indicative for a hit-and-run mechanism, in which driver mutations are induced by the expression of MnPV, which finally lead to tumor development.

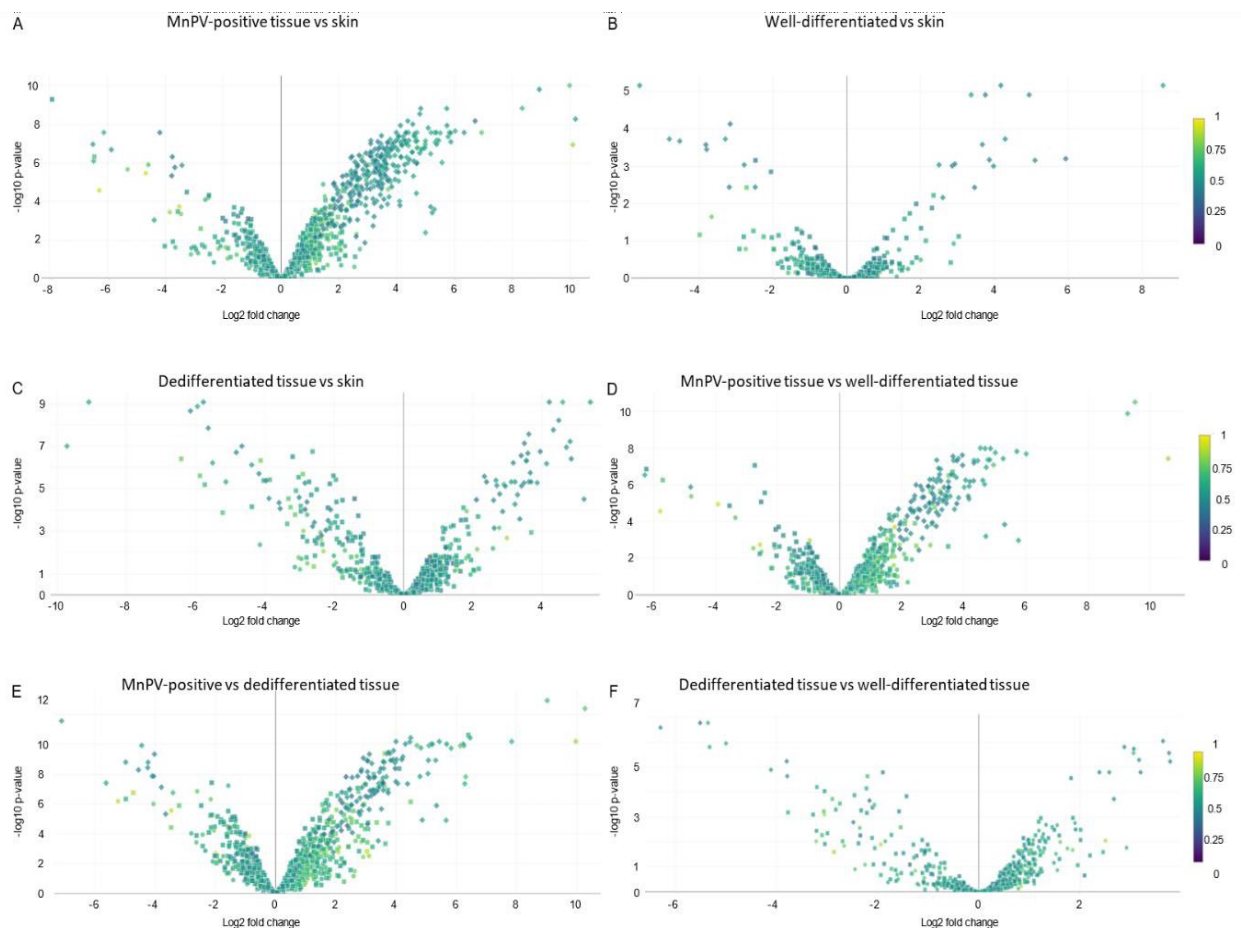


Figure 11: Volcano blots show overview of comparison between different in vivo proteomes. The negative logarithm of the p-value is plotted on the y-axis to base 10. Data points with low p-values (highly significant) appear at the top of the graph. The x-axis displays the logarithm of the fold change between two conditions. A) MnPV tumor vs skin B) Well-differentiated tissue vs skin C) Dedifferentiated tissue vs skin D) MnPV-positive tissue vs well-differentiated tissue E) MnPV-positive tissue vs dedifferentiated tissue F) Dedifferentiated tissue vs well-differentiated tissue.

Results

Thus, this study supports the already known heterogeneity of skin tumors [136-139]. To put the results into a biological context, further analyses of affected signaling networks were performed using the Ingenuity Pathway Analysis software (QIAGEN IPA). IPA compares a given data set with experimental results of over 100,000 publicly available data sets of previous experiments making it possible to identify causal relationships between own data sets, diseases, cellular networks and upstream regulators.

Based on the significantly differentially expressed proteins found in the label free quantification (LFQ)-values, a canonical IPA pathway analysis was performed to determine the most affected pathways in the tumor tissue compared to the skin control (Figure 12).

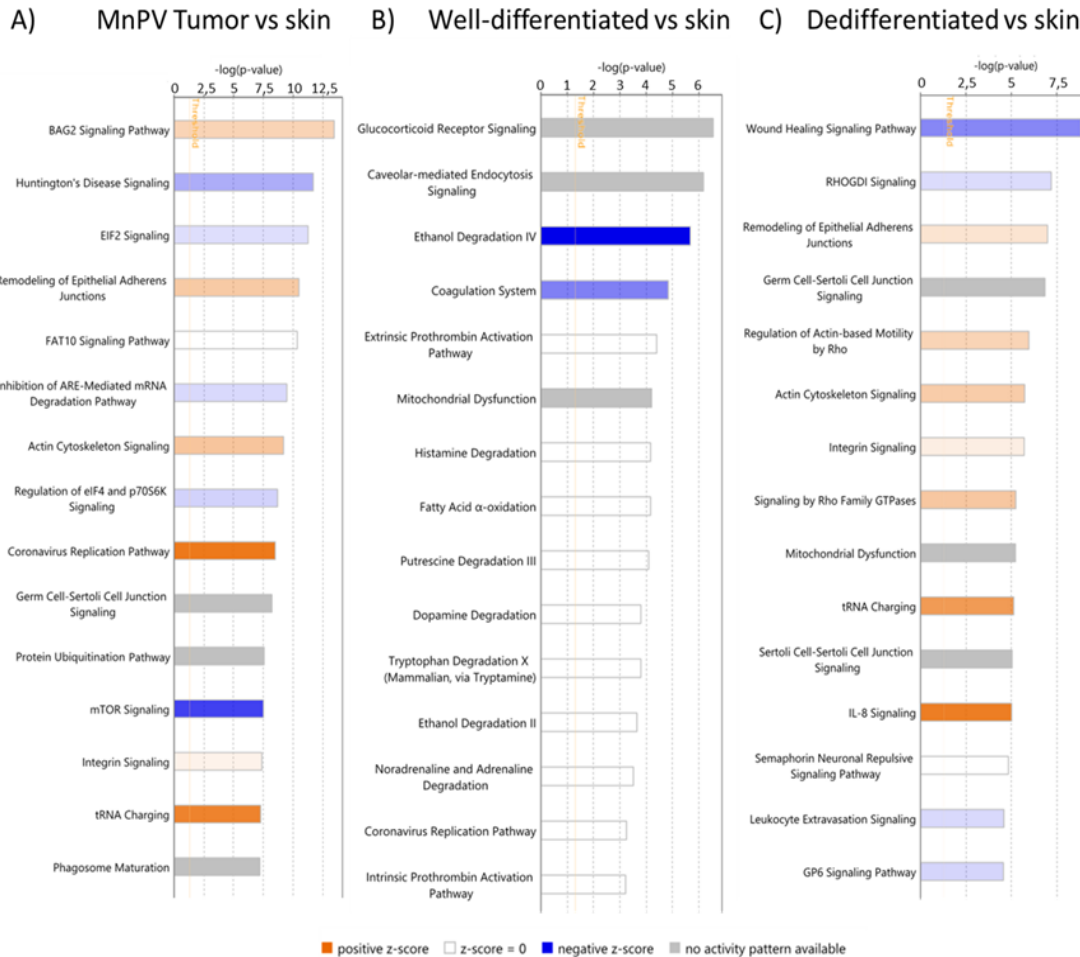


Figure 12: Top 15 altered canonical pathways identified by IPA in in vivo proteomic data sets. A) MnPV-positive tumor tissue vs skin B) Well-differentiated tissue vs skin C) Dedifferentiated tissue vs skin. IPA's z-score indicates a predicted activation or inhibition of a pathway. Negative z-score (blue): overall pathway inhibition, positive z-score (orange): overall pathway activation. IPA applies a $-\log(p\text{-value})$ cutoff of 1.3, meaning that pathways with a p-value equal to or greater than 0.05 are hidden.

Based on the data of the comparison to control skin, a significant downregulation of the mTOR signaling pathway in MnPV-positive tumor tissue was predicted (z-score = -1.89). mTOR signaling pathways regulate protein synthesis, cell division and cell proliferation [140].

Dysregulation of the protein synthesis machinery in cancer has significant implications for pathophysiology, including cancer development and progression [141]. Using canonical pathway analysis by IPA, tRNA-charging was found to be significantly upregulated (z-score = 2.33) when comparing dedifferentiated tissue with control skin. Since the loading of t-RNA is an elementary

Results

component of protein biosynthesis, it can be assumed that this central mechanism is disturbed in dedifferentiated tissue [142].

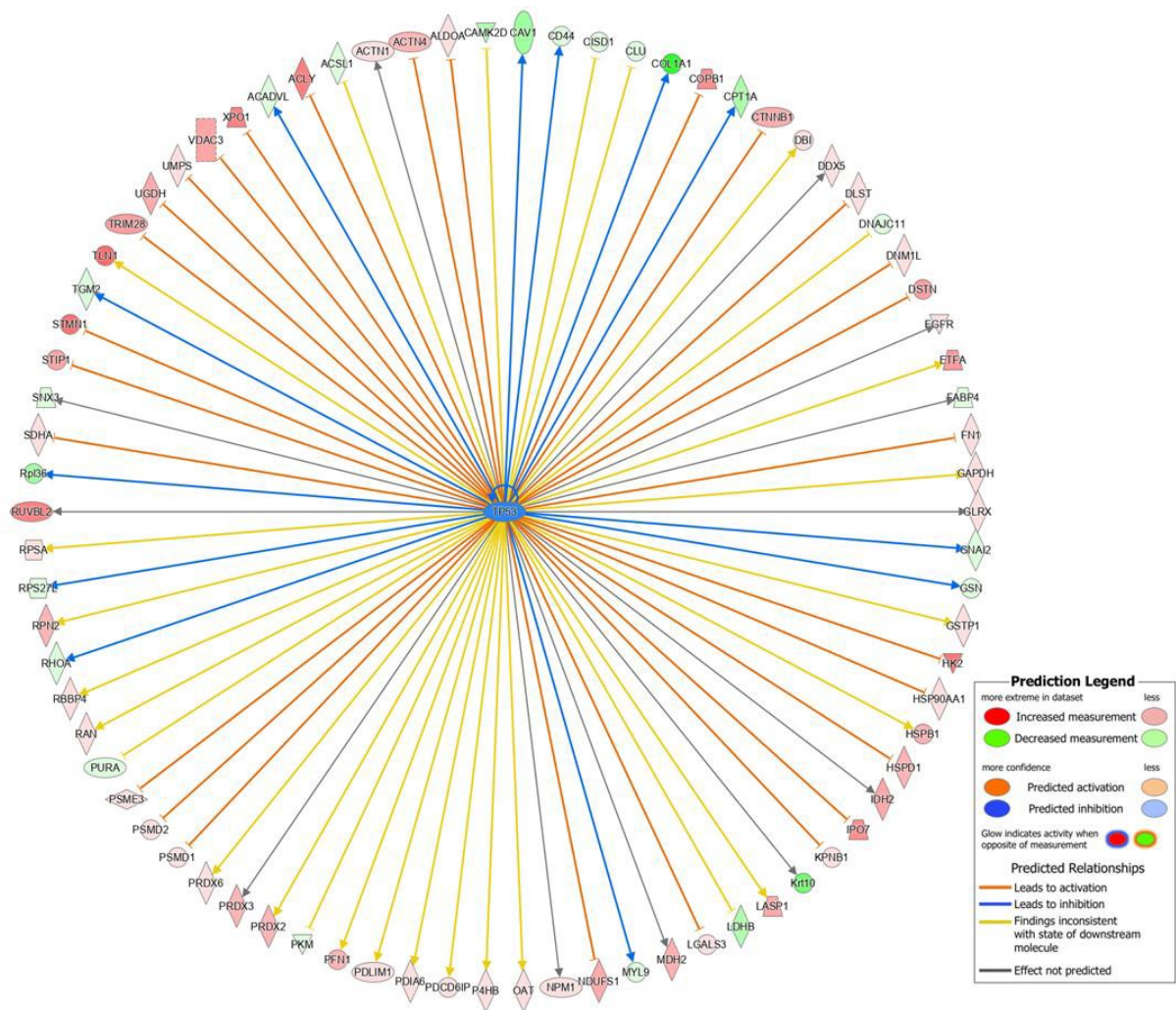


Figure 13: Upstream analysis generated with Ingenuity pathway analysis (IPA) revealed p53 as potentially inhibited in its activation in MnPV- positive tissue when compared to skin control.

Based on the dataset, IPA also allows identifying potential upstream regulators that show a different pattern of activity which could explain the observed changes in protein expression. For this, information about the expected effects between transcriptional regulators and their target genes, which are stored in the Ingenuity® Knowledge Base is used. Therefore, significantly (p -value < 0.05) altered proteins have been entered to the system which gave a statement about the activity of potential upstream regulators. Interestingly, based on the protein expression pattern of altered proteins, IPA names p53-activity as being significantly reduced. In total, the expression pattern of 88

proteins, which are shown in Figure 13, led to this statement. One of these proteins is caveolin (Cav1) which appears to be significantly downregulated ($\log_2FC = -1.32$).

2.2.1 MnPV-infected areas within a tumor display weaker expression of differentiation marker keratin 10 compared to uninfected areas

The global semi-spatial proteome study has revealed interesting candidates (Supplementary Table 1) that are altered in tumor tissue when compared to skin. One of these is the differentiation marker keratin 10 (K10). In IF MnPVE4 served as a marker of infection. In addition, MnPV copy number variations within a tumor could be discerned *via* ISH (Figure 14). Staining of *Mastomys coucha* tissue revealed that K10 is downregulated or lost in MnPV-positive areas when compared to MnPV-negative areas.

Differentiation markers of the skin such as K10 are widely described and considered as well accepted markers for determining the differentiation status of a cell [39-41]. However, it is known that HPVs are able to influence their expression levels [143].

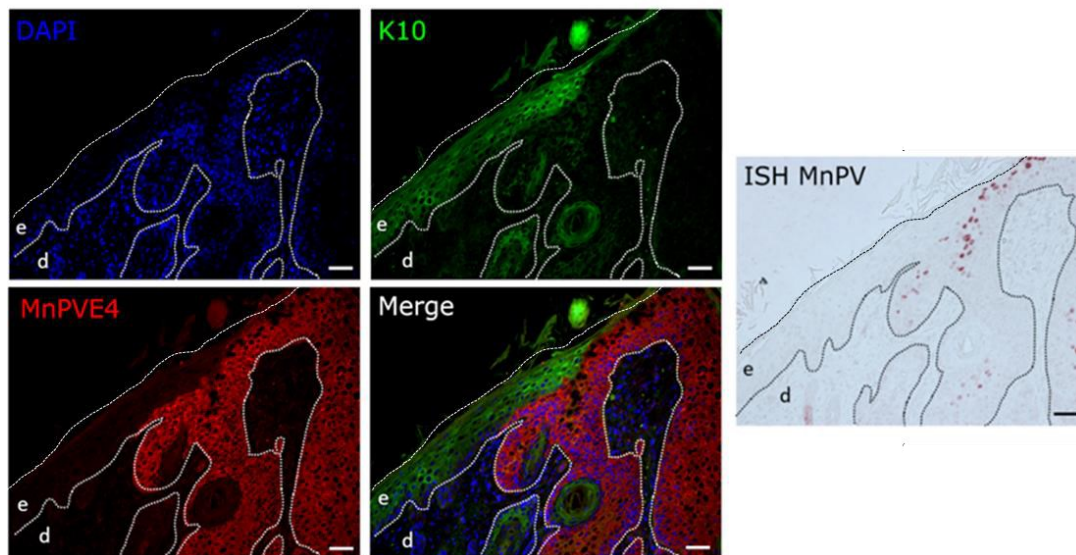


Figure 14: IF and ISH stainings confirm K10 reduction in MnPV-positive tissue when compared to negative tissue. K10 (green) is downregulated in MnPVE4 (red) positive areas. DAPI (blue) served as nuclear marker. In ISH purple stained areas are positive for MnPV- DNA. Scale bars: 50 μm

These results confirm the findings obtained in the proteomic study and highlight the similarities between MnPV infection in *Mastomys* and HPV infection in humans [128, 129].

Results

2.3 *In vitro* proteomics provides new insights into the interplay between MnPV and host cells

The results of the semi-spatial proteomic analysis of different skin tissue types from *Mastomys coucha* provide far-reaching new insights into the effects of a MnPV infection.

However, one must keep in mind that the use of an *in vivo* system entails a high degree of heterogeneity, which is due to the high complexity of an organism. Reducing this complexity by using a top-down approach enables a mechanistic analysis of the influence of MnPV on its host cell.

2.3.1 *In vitro* proteomics using infected murine keratinocytes

MnPV-infected murine 308 keratinocytes [144] are a valid system to investigate the influences of whole virus expression on the cell. In this system, established by Dr. Rui Cao in the laboratory of Prof. Frank Rösl, the entire virus genome is expressed in the target cell (Dissertation of Rui Cao, 2021). The generation as well as the quality control of the infected murine 308 keratinocytes was also done by Dr. Rui Cao (see chapter 5.1.8.), who was able to demonstrate successful infection of the keratinocytes using IF and western blot (WB) (Dissertation Rui Cao, 2021).

Proteome studies of these cells were included within this work. For this purpose, MnPV-infected cells and uninfected cells were lysed and total cell lysates were analyzed by mass spectrometry in triplicates by the Genomics and Proteomics Core Facility of the DKFZ. In total 83872 peptides and 5980 proteins could have been identified by MS/MS based on an FDR cutoff of 0.01 on peptide level and 0.01 on protein level. In all samples 24468 peptides and 4436 proteins had been identified. Match between runs option was enabled to transfer peptide identifications across aw files based on accurate retention time and m/z. Quantification was done using a label free quantification approach based on the MaxLFQ algorithm [135].

To illustrate the comparison of this data set, a volcano plot was created using the LFQ-values of the analysis (Figure 15) showing the extent of the differences and their significance. MnPV infection has an obvious effect on the host cellular proteome, which is reflected in the number of data points that are located far from the origin in the blot. A total of 80 proteins showed a significantly and biologically relevant altered expression level. A list of the top 10 altered proteins is given in Supplemental Table 2.

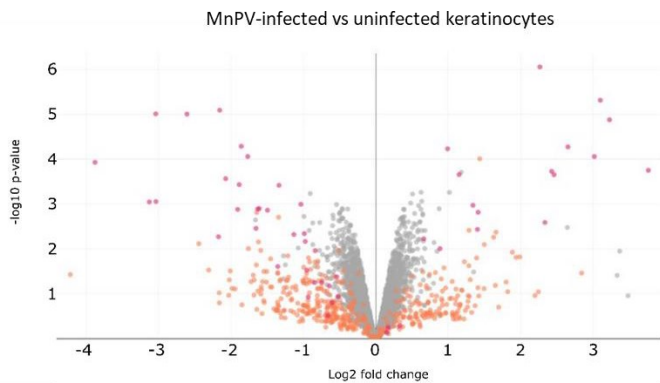


Figure 15: Volcano blot provides a general impression of the comparison of the proteomes between MnPV-infected keratinocytes vs control. For this blot LFQ-values had been used. Grey dots: all values available, orange dots: missing or imputed values, purple dots: missing or imputed data in one condition.

An IPA canonical pathway analysis was performed using the datasets from the proteomic analysis of the infected compared to uninfected control cells. With this, it was possible to put the results into a biological context. Therefore, all significantly altered proteins (LFQ-values) were entered into the software. The top 15 of these pathways are shown in Figure 16.

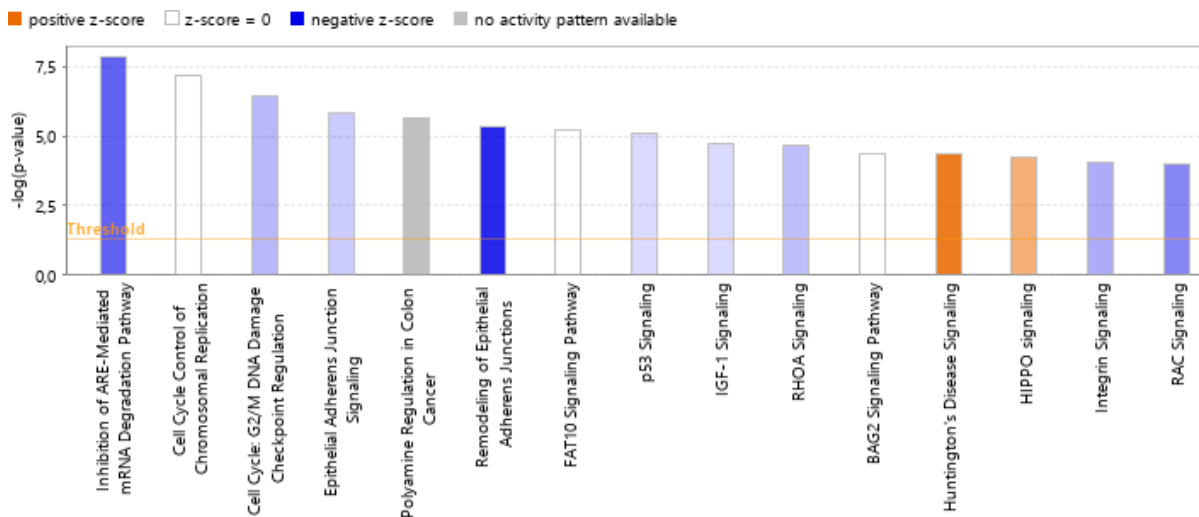


Figure 16: Altered canonical pathways (top 15) of infected murine keratinocytes when compared to control. A pathway analysis allows the visualisation of altered pathways in infected keratinocytes when compared to control cells. For simplicity, only the top 15 altered pathways are shown. Negative z-score: pathway inhibition, positive z-score: pathway activation. IPA applies a $-\log(p\text{-value})$ cutoff of 1.3; $p\text{-value}$ equal to or greater than 0.05 are hidden. LFQ-values had been used to perform this analysis.

Results

The analysis revealed, among others, a significant increase in the activity of the HIPPO pathway in MnPV-infected keratinocytes.

The HIPPO pathway is one of the central components of tissue homeostasis. Many studies have shown a crucial role of this pathway in the control of organ size, tissue regeneration and self-renewal [145-147]. The finding that this pathway is significantly activated in MnPV-infected keratinocytes is also of particular interest, as an effect on this pathway has already been described for HPV-expressing cells [148-150].

To further elucidate whether the two oncoproteins of MnPV are responsible for this effect of the HIPPO pathway, proteomic studies were performed with cells stably expressing MnPVE6, E7, and E6 together with E7. Figure 17 A shows a schematic overview of the cloned constructs which were

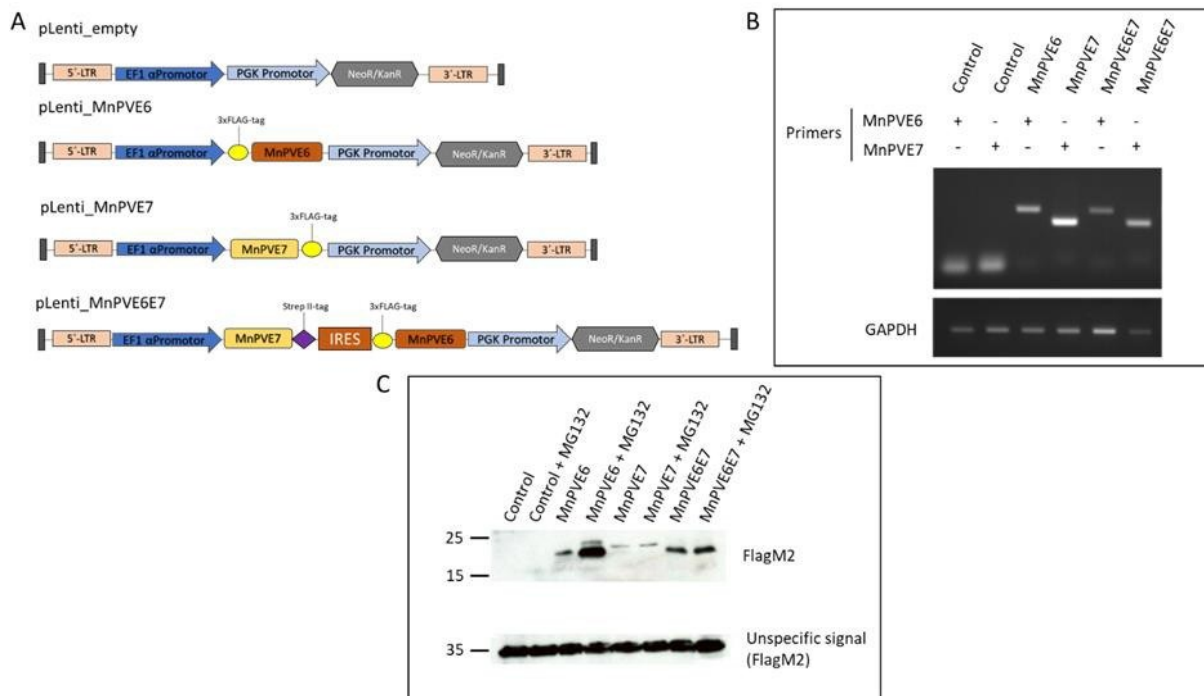
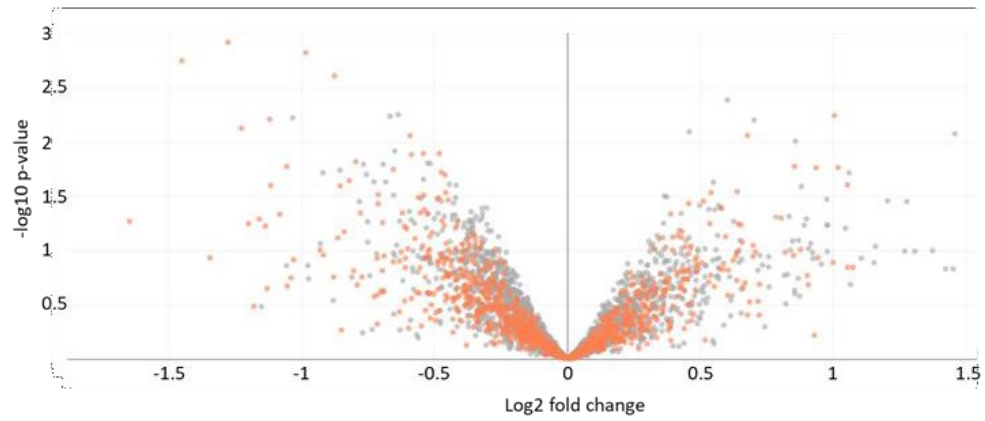


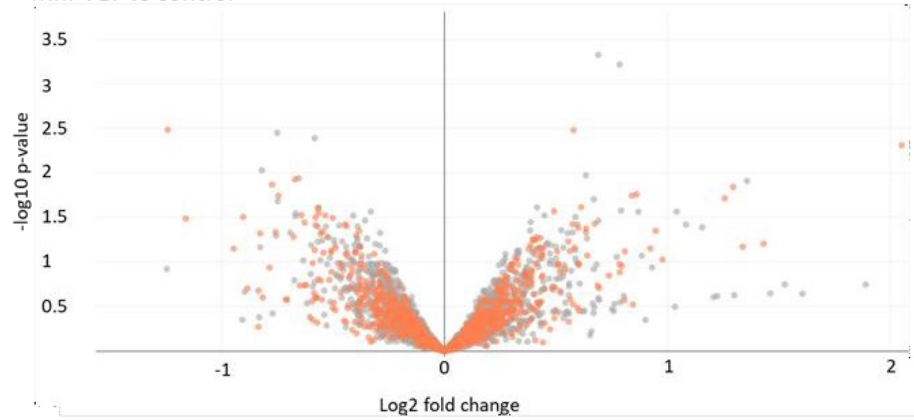
Figure 17: Establishment of 308 keratinocyte cell lines expressing MnPVE6, E7 or E6 and E7. A) Schematic overview of expression cassettes lentivirally transduced to the cells. **B)** Transcription control of transduced 308 keratinocytes using semi-quantitative RT-PCR. PCR was performed with primers against MnPVE6 or E7. cDNA from pLenti_empty transduced cells served as control. GAPDH served as loading control. **C)** WB revealed oncoprotein expression in transduced cells. Lysates from transduced cells were used to confirm oncoprotein expression using anti-Flag antibody. pLenti_empty transduced cells were used as control. Unspecific band of anti-Flag antibody served as a loading control.

transduced into 308 mouse keratinocytes. Successful transduction and subsequent selection of cells was confirmed by semiquantitative PCR (Figure 17 B) and WB (Figure 17 C). The obtained cells were

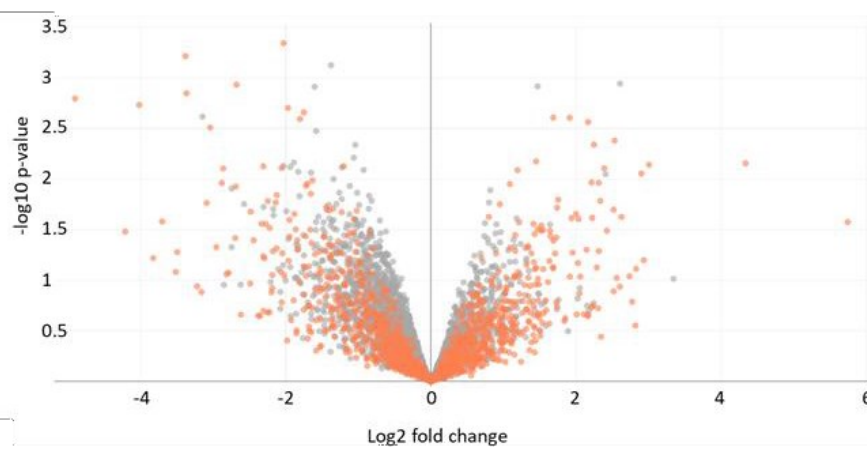
A MnPVE6 vs control



B MnPVE7 vs control



C MnPVE6E7 vs control



Results

Figure 18: Comparison of the proteome of cells expressing MnPV oncoproteins and control proteome of lentivirally transduced 308 keratinocytes. Volcano Blots show an overview of altered proteins in oncoprotein-expressing murine keratinocytes when compared to pLenti_empty. **A)** Comparison of MnPVE6-expressing cells compared to control. **B)** MnPVE7 influenced proteomes compared to empty control. **C)** Proteomes of cells expressing both oncoproteins at the same time compared to control. To create the volcano blots, LFQ-values had been used.

lysed and transferred to the Genomics and Proteomics Core Facility of the DKFZ for mass spectrometric analysis. All samples had been prepared in triplicates.

Peptides have been analyzed by a mass spectrometer. Data analysis was carried out by MaxQuant. In total 70625 peptides and 5153 proteins could have been identified by MS/MS based on an FDR cutoff of 0.01 on peptide level and 0.01 on protein level. Quantification was done using a label free quantification approach based on the MaxLFQ algorithm [135]. Volcano blots were created to illustrate the differences between the samples of oncoprotein-expressing cells and control cells (Figure 18).

A Venn diagram with the significant and biologically relevant changed proteins of the respective groups is shown in Figure 19. Intensity-based absolute quantification (iBAQ)-values [151] had been used for this blot. A total of 151 proteins were found for MnPVE6-expressing cells, showing a significant and biologically relevant change in the expression level when compared to control cells (Figure 19). The biological relevance of a change was defined by $\text{Log}_2\text{FC} > (1)$ or $\text{Log}_2\text{FC} < (-1)$. For

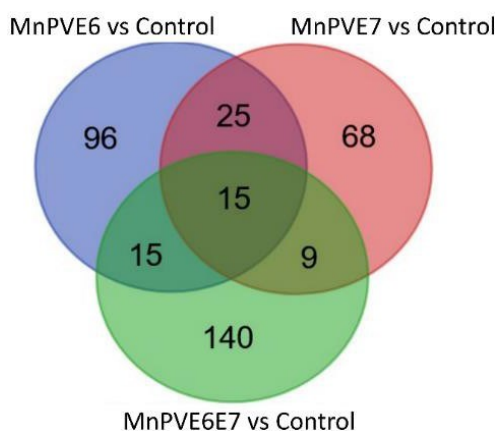


Figure 19: Venn diagram comparing the results from transduced 308 in vitro proteomics. Strongest differences could be examined in cells expressing MnPVE6E7 compared to control (179 proteins were altered). Comparison between MnPVE7-expressing cells and control revealed 117 altered proteins and MnPVE6-expressing cells show 151 altered proteins when compared to control. Diagram is based on iBAQ-values.

MnPVE7-expressing cells, 117 proteins with these specifications could be identified (Figure 19), for cells co-expressing both oncoproteins, 179 proteins with the above specifications (Figure 19) had been identified, representing the strongest differences to the control proteome. A representation of the

strongest differentially expressed proteins in the abovementioned comparisons is shown in Supplemental Table 3.

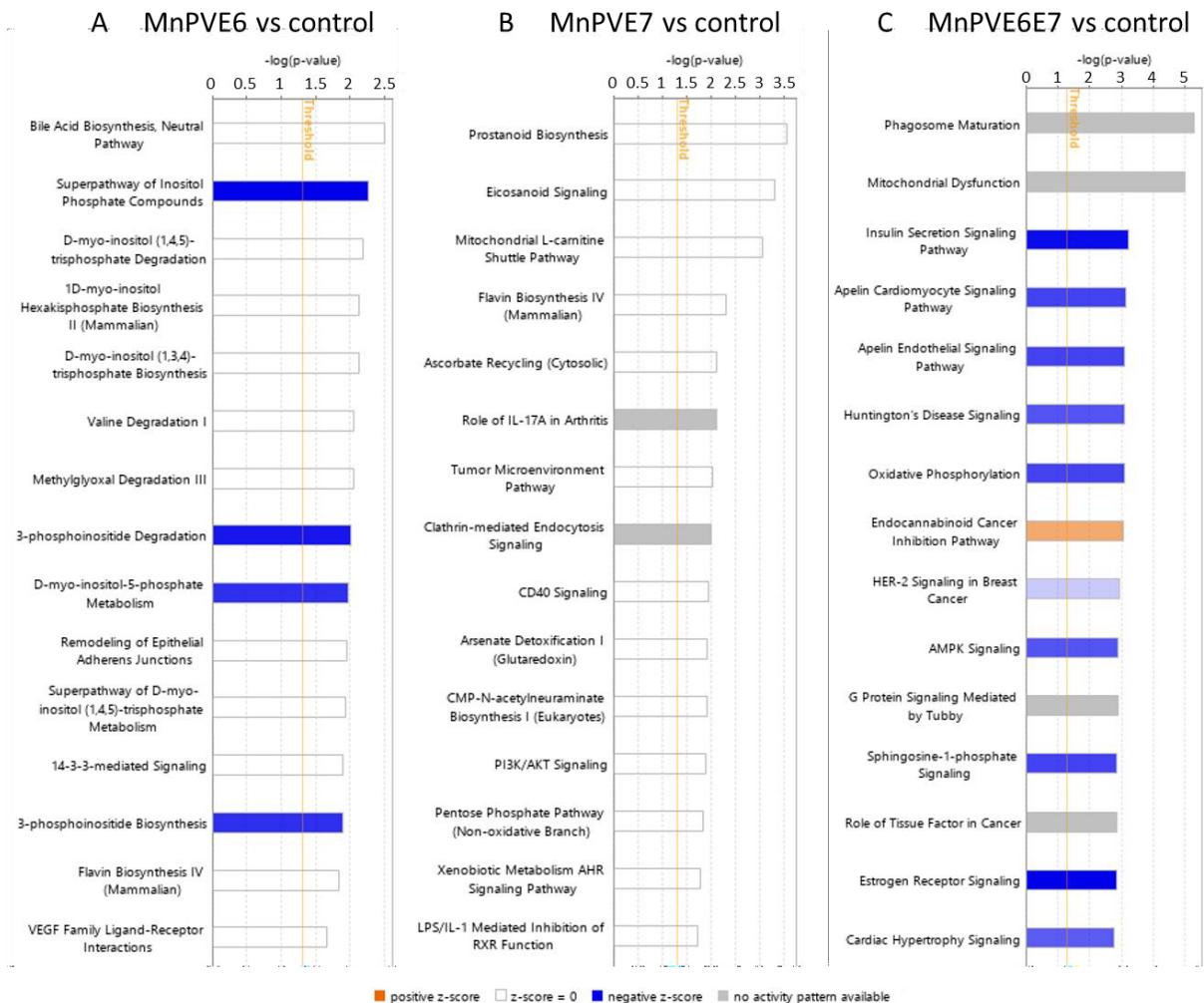


Figure 20: Altered top 15 canonical pathways in in vitro proteomic data sets of transduced 308 cells. A) MnPVE6-expressing cells compared to control cells. B) MnPVE7-expressing cells vs control cells. C) MnPVE6E7-expressing cells compared to control cells. IPA's z-score indicates a predicted activation or inhibition of a pathway. Negative z-score (blue): pathway inhibition, positive z-score (orange): pathway activation. Pathways with a p-value of 0.05 or more are not shown.

For the comparison of MnPV oncoprotein-expressing and control datasets, a canonical pathway analysis was performed using IPA to put the results in a biological context. For this analysis, all significantly altered proteins (LFQ-values) of MnPVE6, E7 or E6E7-expressing cells compared to control cells were entered into the software. The top 15 potentially altered canonical pathways are shown in Figure 20.

Results

The analysis of the canonical signaling pathways showed, among others, a significant upregulation of the endocannabinoid cancer inhibition pathway in MnPVE6E7-expressing cells compared to the control (z-score: 1.13). Endocannabinoids are endogenous lipid signaling molecules [152], which have a wide variety of effects on cells. For example, they inhibit the proliferation of cancer cells, stop the cell cycle and are able to induce cell death [153, 154], which had been demonstrated in both *in vitro* and *in vivo* in various malignant tumors [155, 156].

2.3.2 Wwp2 and Cullin7 are downregulated in the presence of MnPVE7

The results generated in the proteome studies of the transduced 308 keratinocytes provided interesting new insights to the effect of MnPV oncoprotein expression in the cell. Representative altered proteins from this study were additionally examined using WB and IF analyses to confirm the proteome data.

One of these candidates is the NEDD4-like E3 ubiquitin-protein ligase Wwp2. Wwp2 ubiquitinylates E3 SUMO-protein ligase EGR2 and thereby promotes its proteasomal degradation [157]. In T cells, this

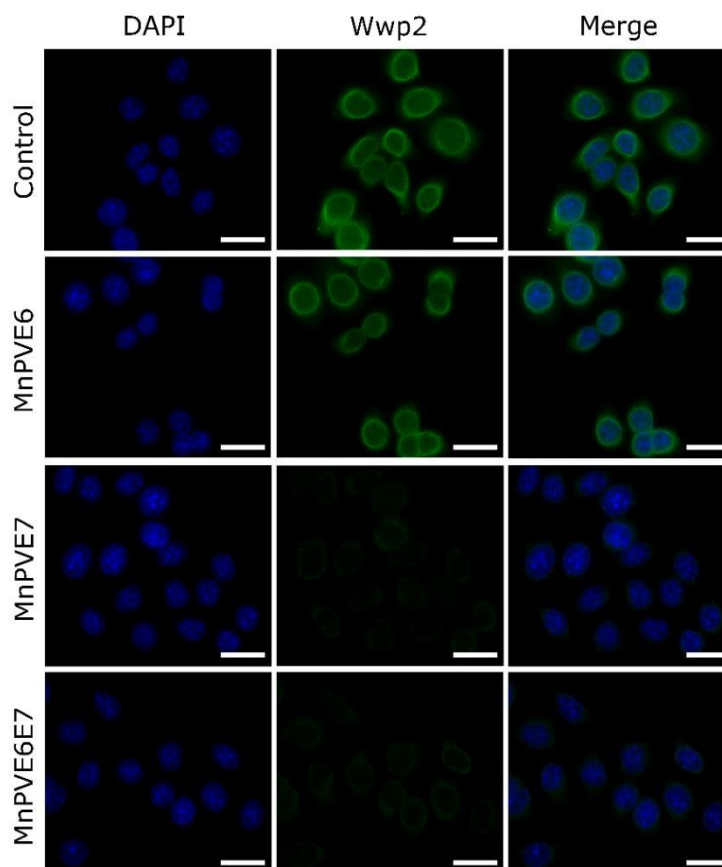


Figure 21: Wwp2 is reduced in MnPVE7- and MnPVE6E7-expressing cells when compared to control. Reduction of Wwp2 can be visualized in MnPVE7- and MnPVE6E7-expressing cells by IF. Wwp2 is stained in green. DAPI was used as nuclear marker (blue). Scale bars: 20 μ m

ubiquitylation inhibits induced cell death [158]. In addition, Wwp2 ubiquitylates DNA-directed RNA polymerase II subunit RPB1, which leads to its degradation [159]. In the proteomic analysis of MnPVE6E7-expressing cells compared to control, Wwp2 was significantly downregulated ($\log_2FC = -1.8$, $p\text{-value} = 0.002$). By IF, this downregulation was confirmed in MnPVE6E7-expressing cells. Interestingly, downregulation of Wwp2 was also observed in MnPVE7-expressing cells (Figure 21).

In addition to Wwp2, another candidate was investigated in detail. Cullin7 (Cul7) is the core component of the 3M and Cul7-RING(FBXW8) complexes, which mediates the ubiquitination of target

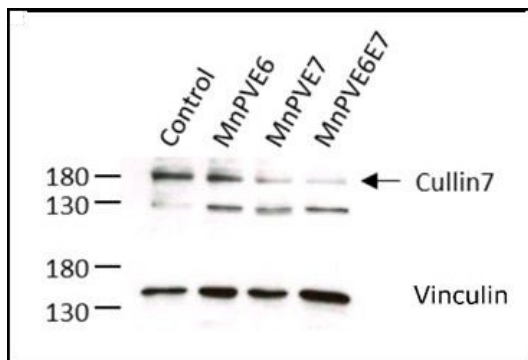


Figure 22: Downregulation of Cul7 in MnPVE7- and MnPVE6E7-expressing cells shown by WB. MnPV oncoprotein-expressing keratinocytes and empty-plasmid transduced control cells were lysed, and lysates were used in WB revealing downregulation of Cul7 in MnPVE7- and MnPVE6E7-expressing cells. Vinculin served as loading control.

proteins [160]. Target proteins are, among others, MAP4K1/HPK1. Cullin7 recognizes and binds auto-phosphorylated MAP4K1/HPK1, leading to its degradation and thereby affecting cell proliferation and differentiation [161]. In the proteomic study a significant reduction ($\log_2FC = -1.95$, $p\text{-value} = 0.025$) of Cullin7 in MnPVE6E7-expressing cells was observed when compared to control. In fact, its reduction in MnPVE7- as well as MnPVE6E7-expressing cells could be observed by WB (Figure 22).

2.3.3 HPV38 oncoprotein-expressing keratinocytes

Cutaneous HPV type 38 was included in this study as it can contribute, like MnPV in *Mastomys*, to the development of NMSC in humans *via* a hit-and-run mechanism in combination with UV light [84] and is therefore a particularly interesting candidate for placing the results from the *Mastomys* model to a human context. Therefore, the effect of the oncoprotein expression of the cutaneous HPV38 on the host cell proteome was examined.

For this purpose, normal oral keratinocytes (NOK) cells were lentivirally transduced with the constructs shown in Figure 23 A. After selection with puromycin, successful transduction was verified by semi-quantitative RT-PCR (Figure 23 B). Morphologically, no differences between the generated

Results

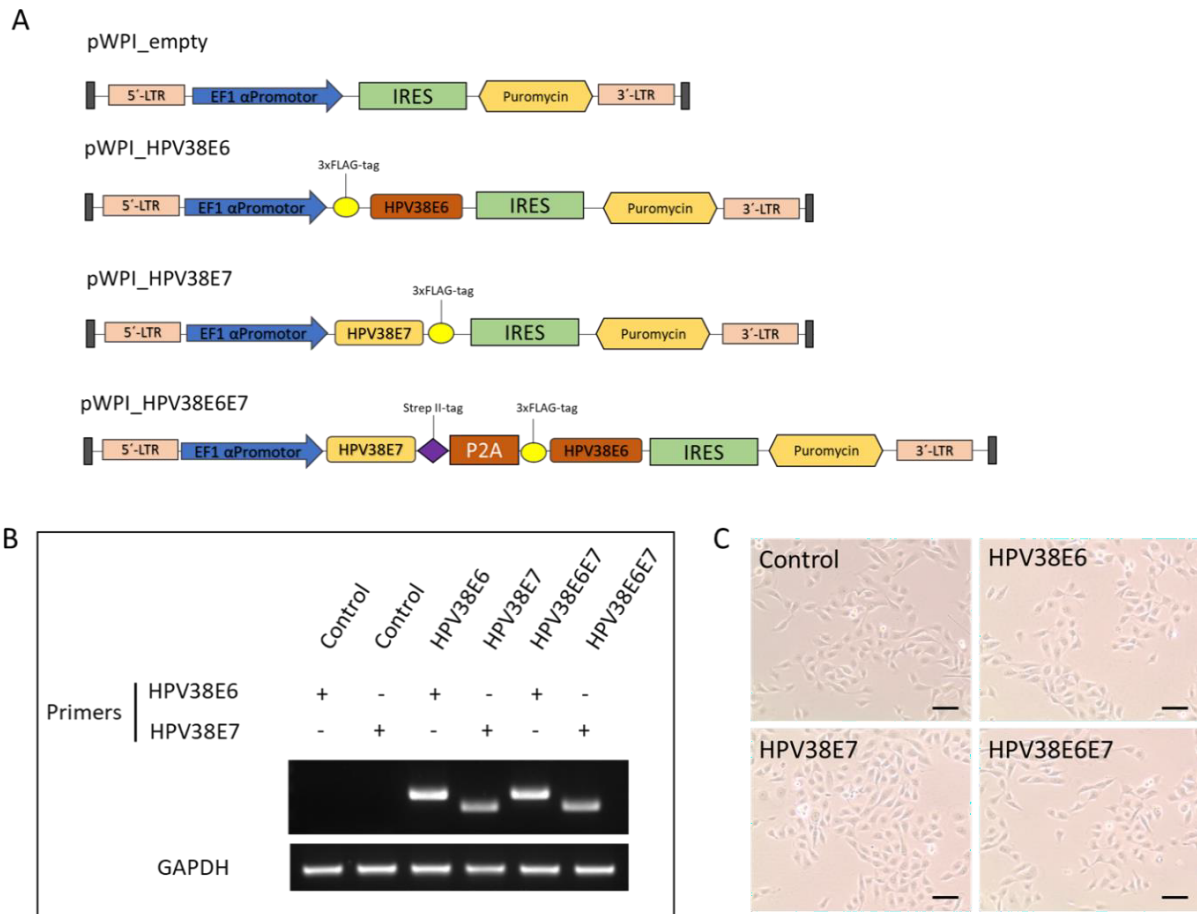
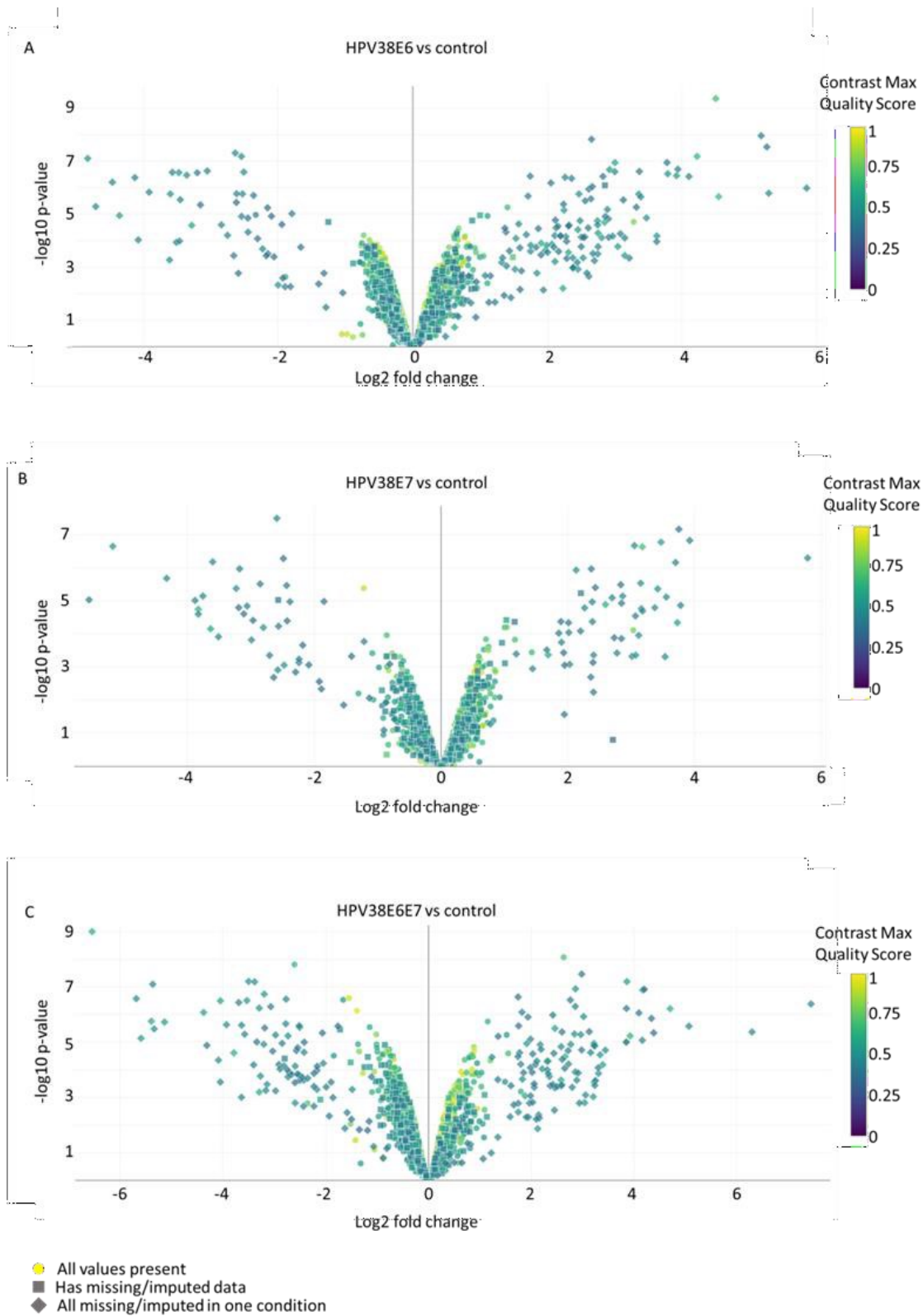


Figure 23: Establishment of NOK cell lines expressing HPV38 oncoproteins. A) Schematic overview of expression cassettes which allow expression of Flag-tagged HPV38E6 or E7 or both oncoproteins together. Constructs were lentivirally transduced to NOK cells. pWPI_empty serves as control construct. **B)** Transcription control of transduced NOK using semi-quantitative RT-PCR. Primers against HPV38E6 and E7 was performed with cDNA from empty vector control (pWPI_empty) or oncogene-transduced cells. GAPDH served as loading control. **C)** Light microscopic images of oncoprotein-expressing cells show no morphological differences when compared to pWPI_empty control. Scale bars: 50 μ m.

cell lines could be detected, as shown by light microscopy (Figure 23 C). The lysates of these cell lines were forwarded to the Genomics and Proteomics Core Facility of the DKFZ for further proteomic analyses performed in triplicates to identify their proteomes in comparison to empty plasmid transduced control cells. For data analysis, MaxQuant software was used. In total 70360 peptides and 5246 proteins could have been identified by MS/MS based on an FDR cutoff of 0.01 on peptide level

and 0.01 on protein level. Quantification was done using a label free quantification approach based on the MaxLFQ algorithm [135].



Results

Figure 24: Comparison of the proteomes of HPV38 oncoprotein-expressing and control transduced NOK cells.

Volcano Blots give an overview of altered proteins in oncoprotein-expressing cells when compared to pWPI_empty control. A) Comparison of proteome datasets from HPV38E6-expressing cells with those from control cells B) Proteomes of cells influenced by the expression of HPV38E7 compared to control. C) Strongest differences can be described in proteomes from HPV38E6E7-expressing cells when compared to control. The negative logarithm of the p-value is plotted on the y-axis to base 10. The x-axis shows the logarithm of the fold change between the two conditions. For the generation of the volcano blots, LFQ-values were used.

To graphically illustrate the comparisons between the resulting data sets volcano blots were created (Figure 24).

Comparing the proteomes of the HPV38E6-expressing NOK cells with those of the control cells transduced with pWPI_empty, 176 proteins are significantly and biologically relevantly altered. Biologically relevance is classified by $\log_2FC < (-1)$ or $\log_2FC > (1)$. For HPV38E7, compared to the control, 97 proteins fulfill these specifications, for cells expressing both oncoproteins at the same time 224 proteins were altered. A compilation of the most affected proteins is shown in Supplemental Table 4.

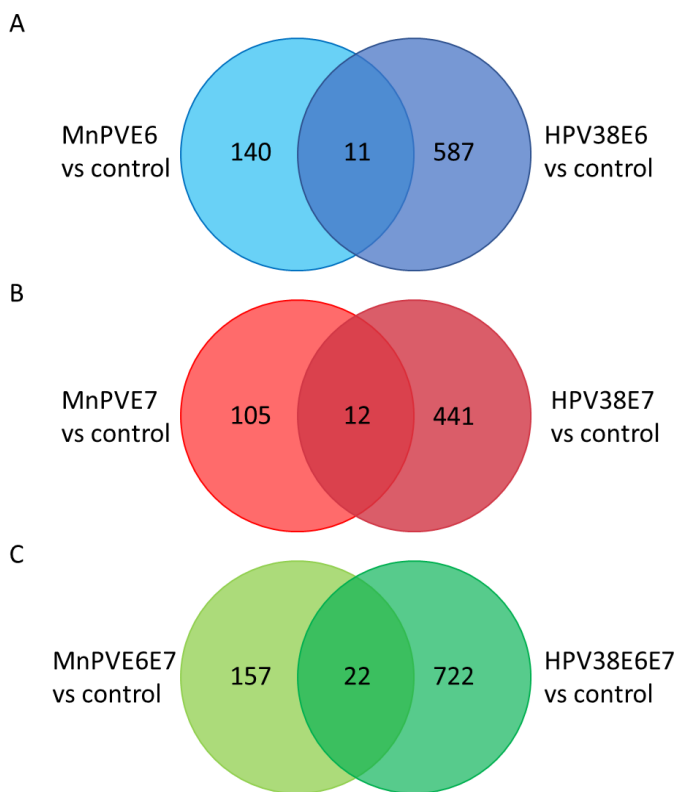


Figure 25: Venn diagrams show comparison of altered proteins of in vitro proteomic studies of MnPV and HPV38 oncoprotein-expressing cells compared to the respective controls. A) Comparison between protein data sets of altered proteins characterized in MnPVE6- and HPV38E6-expressing cells compared to the respective control. B) Comparison between MnPVE7 and HPV38E7 datasets. C) Comparison between data sets resulting from cells expressing both oncoproteins. For the generation of these diagrams the LFQ-values of significantly ($p < 0.05$) and biologically relevant [$\log_2FC < (-1)$; $\log_2FC > (1)$] altered proteins had been used.

A Venn diagram shows the comparison between altered proteins from the MnPV and HPV38 proteome analyses (Figure 25). For the MnPVE6-expressing cells, 11 proteins were found that were also altered in HPV38E6-expressing cells. For the E7-expressing cells, 12 proteins were found, and for cells expressing both oncoproteins simultaneously, 22 proteins were found altered in both cell lines compared to the respective control.

2.4 Interactome studies uncover host cellular interaction partners of cutaneous PVs oncoproteins

Interactome studies were performed for the E6 and E7 oncoproteins of MnPV and HPV38 to obtain information on the interaction between the virus and the host cell. HPV38 was used as a reference in this context since much information is already available for this HPV type [84, 162-164].

To generate the interactome for the oncoproteins, two methods were used: Firstly, the BioID method [165], which allows labeling and subsequent characterization of a host cell protein surrounding a target protein by biotinylation within a living cell, and secondly, an immunoprecipitation (IP) to detect binding partners [166]. For both methods, a mass spectrometric evaluation was used.

2.4.1 BioID for MnPV and cutaneous HPV38 oncoproteins

To detect potential interaction partners of MnPV and HPV38 oncoproteins, BioID was performed [165]. First, a construct was cloned to generate a fusion protein consisting of a promiscuous biotin ligase (BirA*) [167] linked to protein of interest (MnPVE6 or MnPVE7) (Figure 26 A). Target cell line was chosen according to previous biotinylation tests (Supplemental Figure 2). To guarantee a sufficiently strong biotinylation for the subsequent BioID, MaFi132 cells were first transiently transfected with plenti_GFP-BirA* control, treated with 50 μ M of biotin overnight and lysed the next day. The lysates were tested for successful biotinylation of the host cell proteins in a WB with antibodies against biotin. An illustration of an exemplary blot is provided in Supplemental Figure 3.

Results

After successful lentiviral transduction of the target cells (*Mastomys* fibroblasts 132; MaFi132 [168]), verified by semi-quantitative PCR (Figure 26 B) and WB (Figure 26 C), the fusion proteins enabled the labeling of surrounding proteins through biotinylation within the living cell. Subsequent streptavidin pulldown allowed the purification of the labeled proteins, which were subsequently characterized by mass spectrometry.

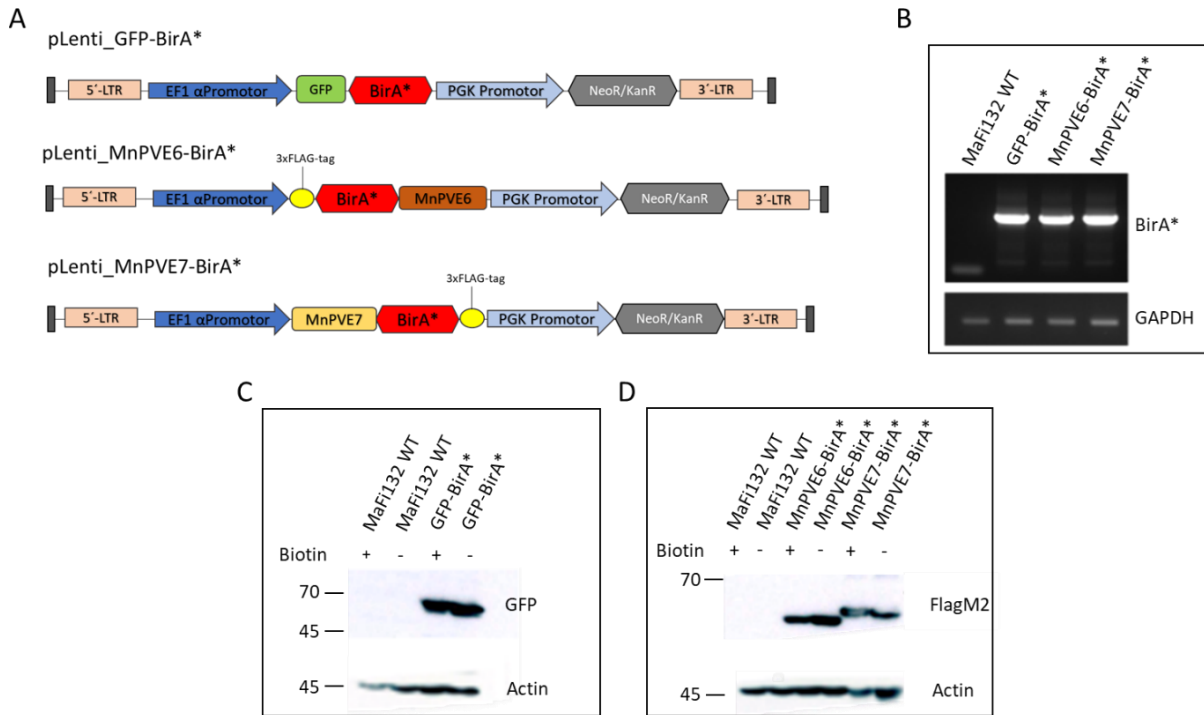
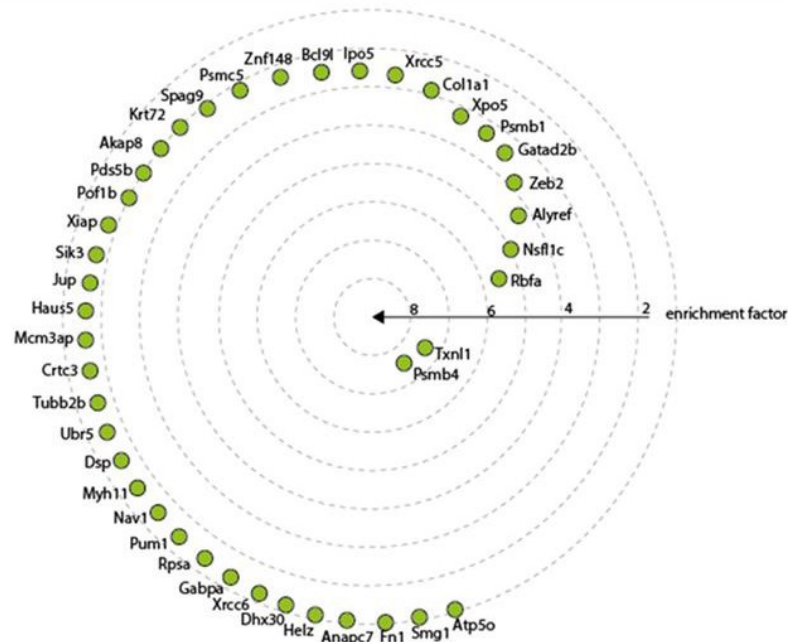


Figure 26: Establishment of MaFi132 cell lines to describe the interactome of MnPV E6 and E7 by BioID. A) Schematic overview of constructs used to transduce MaFi132. pLenti_GFP-BirA* served as control. pLenti_MnPVE6-BirA* and pLenti_MnPVE7-BirA* code for E6 or E7 fused to BirA*. The fusion proteins were Flag-tagged to enable the detection in WB. The fusion site of BirA* (at N/C-terminal of the oncoprotein) is based on functionality tests using the same principle on HPV16 in our group (unpublished, manuscript in preparation). **B)** Transcription control of transduced MaFi132 using semi-quantitative PCR with primers against BirA* verifies successful transduction. GAPDH served as loading control. **C)** WB confirmed biotin ligase fusion protein expression in transduced cells using anti-Flag or anti-GFP antibodies. Actin served as a loading control.

Within the interactome study using the BioID method, 41 host cell proteins could be identified as putative interactors of MnPVE6 and 157 of MnPVE7. These proteins are listed in Figure 27. The enrichment factor given in

this Figure shows how often a particular protein appeared in the triplicated samples when compared to control. In addition to the interactome study for E6 and E7 of MnPV, a BioID was also performed for the two oncoproteins of the cutaneous HPV38. For this purpose, NOK cells were transduced with

A MnPVE6



B MnPVE7

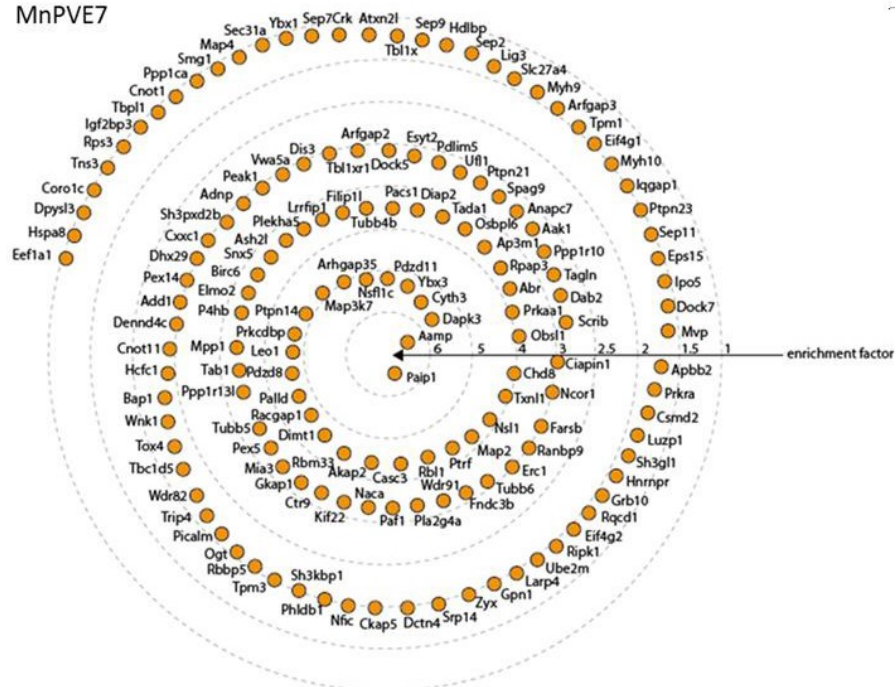


Figure 27: Illustration of MnPVE6 and E7 interaction partners identified by BioID. Enrichment factors show the frequency that the named protein appeared in the samples when compared to control. **A)** Putative interactors of MnPVE6. **B)** Putative interactors of MnPVE7.

Results

a construct consisting of a fusion protein of the respective oncoprotein and the biotin ligase BirA*. An illustration of these constructs is shown in Figure 28 A. Successful transduction was verified by semi-quantitative PCR using primers against BirA* (Figure 28 B). WB (Figure 28 C) was performed to verify the expression of the genes and the translation to fusion proteins.

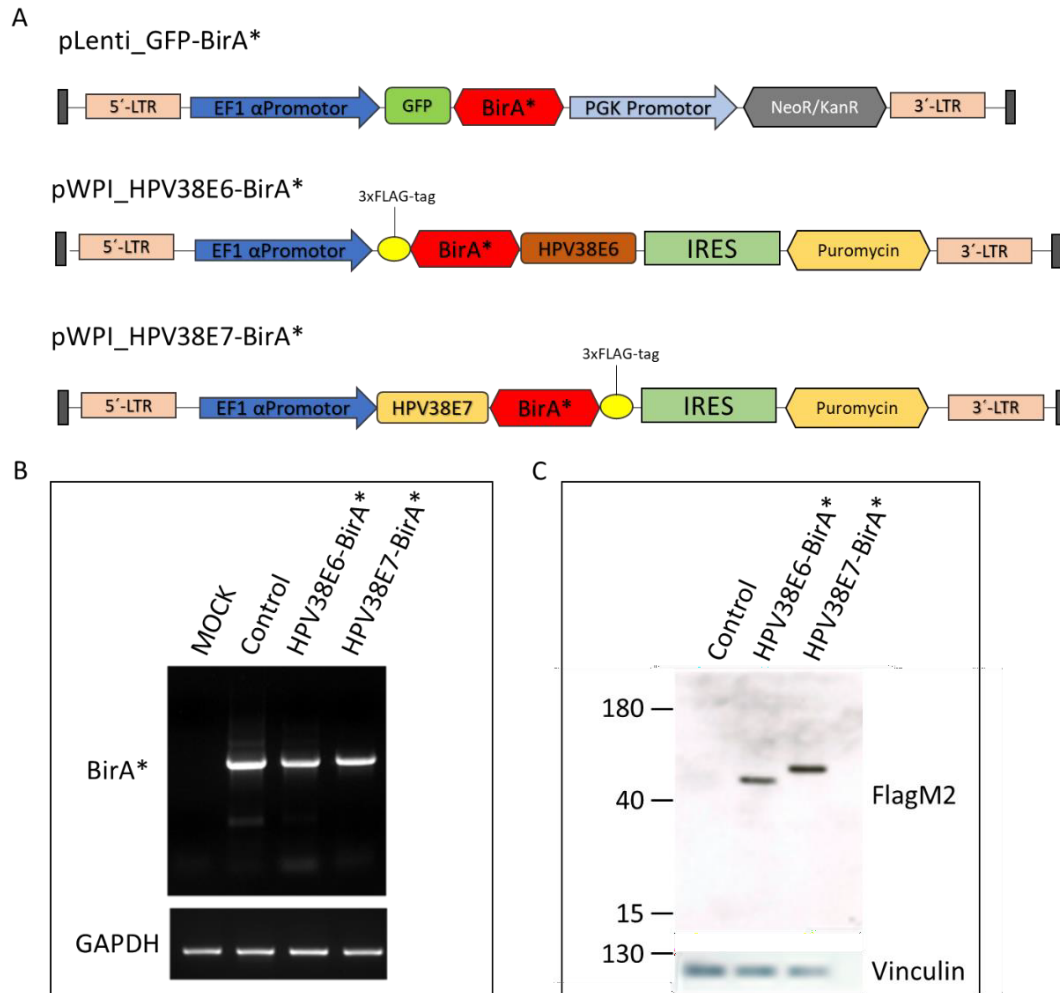


Figure 28: Establishment of stable NOK cell lines to describe the interactome of E6 and E7 of HPV38 via BioID.

A) Schematic overview of cloned and transduced constructs. Construct pLenti_GFP-BirA* served as control. Constructs pWPI_HPV38E6-BirA* and pWPI_HPV38E7-BirA* code for E6 or E7 fused to BirA*. The fusion site of BirA* is based on the same functional tests that already served for the construction of MnPV-BirA* constructs (unpublished, manuscript in preparation). **B)** Transcription control of transduced NOK cells using semi-quantitative PCR proved transcription of BirA* in transduced cells. pLenti_GFP-BirA* serves as control. GAPDH served as loading control. **C)** WB revealed correct biotin ligase fusion protein expression in transduced NOK cells using anti-Flag antibody. pLenti_GFP-BirA* cell lysates were used as control. Vinculin served as loading control.

After streptavidin purification, the biotinylated protein mixtures were handed over to the Genomics and Proteomics Core Facility of the DKFZ. Here, the mixtures were analyzed mass-spectrometrically in triplicates. Data analysis was carried out by MaxQuant. In total 25669 peptides and 2747 proteins could have been identified by MS/MS based on an FDR cutoff of 0.01 on peptide level and 0.01 on protein level. Quantification was done using a label free quantification approach based on the MaxLFQ algorithm [135].

Using the above- mentioned BioID, in total 304 interacting proteins could be found for HPV38E6 and 300 for HPV38E7.

S100A9, which plays a key role in cell cycle regulation and inflammation [169-171], was described here by BioID as an interaction partner of HPV38E7. Interestingly, this protein shows altered expression patterns in many types of cancer (reviewed in: [172]), including in cells of head and neck squamous cell carcinoma (HNSCC), in which it is downregulated [173].

A comparison of interactors of MnPV and HPV38 oncoproteins is shown in chapter 2.3.2. Figure 31.

2.4.2 Analysis of the interactome of the two oncoproteins MnPV E6 and E7 using IP

In addition to the BioID performed, IP followed by mass spectrometric analysis (IP/MS) was done to further characterize the interactome of MnPVE6 and MnPVE7 in more detail. To determine cellular interaction partners of MnPV oncoproteins using IP, transiently transfected *Mastomys* Fibroblasts (MaFi132) expressing either MnPVE6-Flag or MnPVE7-Flag were lysed. Whole cell lysates were subjected to a Flag-IP followed by MS (IP/MS).

With this method a total of 125 host cellular proteins were identified as interactors for MnPVE6 and 386 for MnPVE7. 74 proteins could be described as interactors for both oncoproteins, resulting in 41 proteins that bind exclusively to MnPVE6 and 302 that bind only to MnPVE7 (Figure 29). To illustrate interactors found in BioID as well as in IP, a Venn diagram was created. For this diagram iBAQ values had been used.

Results

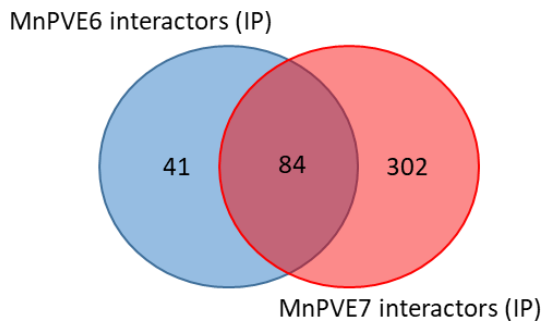


Figure 29: Comparison between interactors revealed for MnPVE6 and E7 in IP. For MnPVE6 125 host cell proteins could be characterized as interaction partner using IP. For MnPVE7 386 interactors had been identified. 84 proteins are interactors of both oncoproteins. iBAQ-values had been used to generate this diagram.

In order to validate the results obtained from the interactome studies, single candidates were examined in detail. For this purpose, an IP using lysates of transiently transfected *Mastomys* fibroblasts (MaFi132) expressing either MnPVE6-Flag or MnPVE7-Flag was performed. This IP was followed by WB. The results of this analysis are shown in Figure 29.

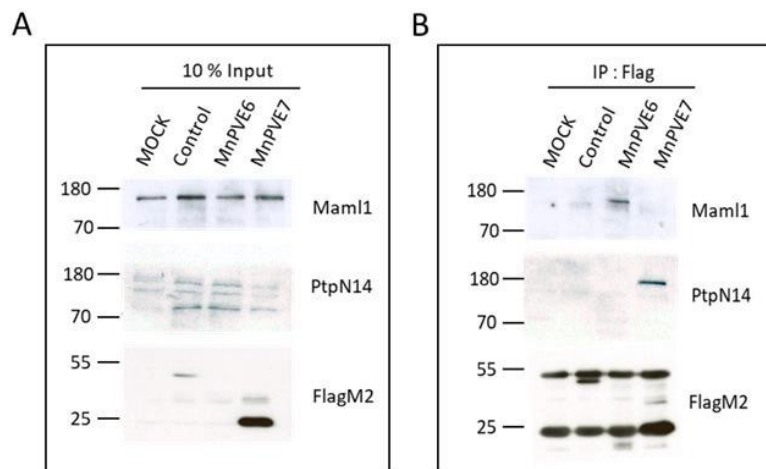


Figure 30: Immunoblotted IPs verifies PtpN14 as interaction partner of MnPVE7 and Maml1 binding to MnPVE6. Lysates from MnPV oncoprotein transfected MaFi132 cells were used in IPs against Flag-tag. Precipitates were analyzed in WB using Flag, Maml1 and PtpN14 antibodies. pCMV_empty transfected MaFi132 served as control. A) 10% input samples. B) IP:Flag samples.

Among the interaction partners of E6 found by IP, Smad2/3 could be characterized, for which the context to HPV E6 proteins had already been shown [174].

The results of the WB analyses confirmed the IP/MS results. Thus, Mastermind-like protein 1 (Mam1) can be verified as an already described interaction partner of MnPVE6 [175]. In addition, Tyrosine-protein phosphatase non-receptor type 14 (PtpN14) can be characterized as an interaction partner of MnPVE7 for the first time (Figure 30 B).

Comparisons of the interacting proteins characterized by the different experiments were made and presented as Venn diagrams (Figure 31).

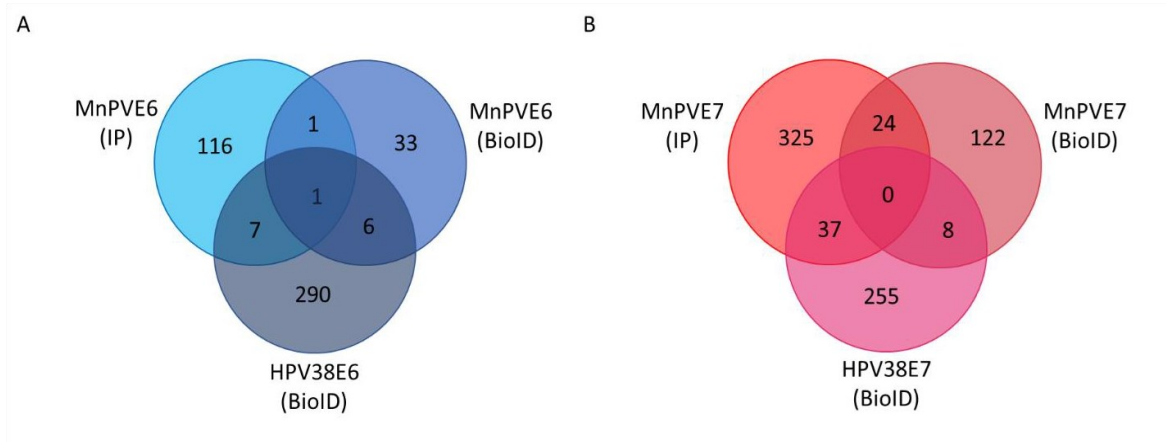


Figure 31: Comparison of interactomes for E6 and E7 of MnPV and HPV38 analyzed by BioID and IP. A) The competitive interaction analyses for E6 show that there is only one common interactor for MnPV (BioID and IP) and HPV38, which is Ipo5. **B)** For E7 no interactor could be described for MnPV E7 that appears in in IP and BioID as well as for HPV38E7 (BioID). iBAQ values had been used to generate these diagrams.

A direct comparison of the interactomes data obtained by different methods revealed only one common interaction partner for MnPVE6 and HPV38E6, which is Ipo5. However, if the BioID results are compared with each other, 6 common interactors of the oncoproteins could be characterized. For the comparison between the IP performed for MnPVE6 and the HPV38E6 BioID, 7 common interactors can be found. Among them is Mam1, which has already been shown in other studies to be an interactor of MnPVE6 and HPV38E6 [175, 176]. In the comparisons of MnPVE7 and HPV38E7 interactors, common binding partners are only found when the results obtained in BioID are compared (8 in common) or when the BioID for HPV38E7 and the IP results for MnPVE7 are compared (37 in common).

Results

2.5 Deeper understanding of the influence of MnPV oncoproteins on the host cell - Investigation of the influence of MnPV on the HIPPO signaling pathway.

The proteome and interactome studies conducted in this work have already provided new insights into how MnPV affects the host cell. One of the effects observed is the downregulation of PtpN14 in MnPV oncoprotein-expressing cells. To gain a deeper understanding of the processes involved, which may be interrupted by MnPV, the effect of PtpN14 downregulation on the host cell was investigated. To this end, the reduction of PtpN14 in MnPVE6E7-expressing cells described in the proteomic analysis was first verified in WB and IF. To analyze the downstream effects of this protein, the localization of Yap/Taz was investigated since their intracellular compartmentation is controlled by PtpN14.

2.5.1 PtpN14 reduction under the influence of PVE7

PTPN14 is a member of the PTP protein family which are signaling molecules known to regulate a variety of different cellular processes.

Apart from the binding of PtpN14 to MnPVE7 as revealed in the interactome study by BioID and IP/MS, PtpN14 was characterized as an altered protein in the *in vitro* proteome studies of MnPVE6E7-transduced keratinocytes showing a significant reduction of this phosphatase compared to control (log₂FC of -2.02 at p-value < 0.05).

To validate this observation, MnPV oncoprotein-expressing 308 cells were lysed and PtpN14 levels were determined using WB, which confirmed its reduction in MnPVE6E7-expressing cells (Figure 32 A). Apart from this, a reduction of PtpN14 could also be seen in MnPVE7-expressing cells. In addition, an IF was performed showing a reduced expression of this phosphatase in MnPVE7- and MnPVE6E7-expressing cells (Figure 32 B). These differences in the PtpN14 signal intensity in IF had also been quantified using the software ImageJ (Figure 32 C). Here, measurements of the signal intensity of PtpN14 showed a significant down-regulation (p-value = 0.028) of PtpN14 in 308 keratinocytes expressing MnPVE7. This trend is also observed in MnPVE6E7 cells (p-value = 0.059) when compared to control. For this measurement, three pictures of three independent experiments had been used.

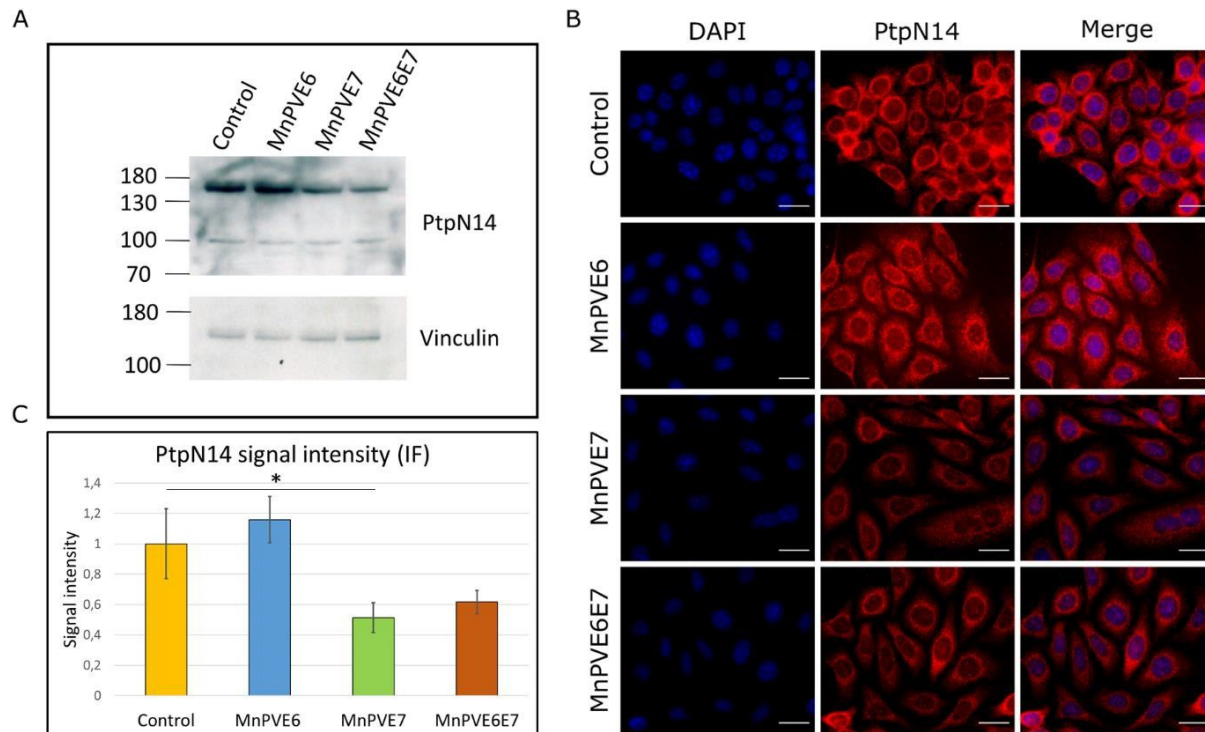


Figure 32: PtpN14 reduction in MnPVE7-expressing murine keratinocytes. **A)** WB of transduced 308 keratinocytes reveals PtpN14 reduction in MnPVE7- and MnPVE6E7-expressing cells. Vinculin served as loading control. **B)** IF of transduced 308 cells show PtpN14 reduction in MnPVE7- and MnPVE6E7-expressing cells. **C)** Signal quantification of PtpN14 IF stainings reveal significant reduction of this phosphatase in MnPVE7-expressing cells ($p = 0.028$). In addition, the tendency of a reduction can also be shown in MnPVE6E7-expressing cells ($p = 0.059$).

Since the reduction of PtpN14 could be demonstrated, the question arises as to what effect this reduction has. To answer this question, special attention was paid to the role of PtpN14 in the HIPPO pathway.

2.5.2 Downstream effects of PtpN14 downregulation- Investigating the localization of Yap/Taz

PTPN14 is shown to be a negative regulator of the oncogenic potential of YAP through a direct interaction of PTPN14 PPxY motifs and YAP/TAZ WW domains [177].

In the past, various methods have been used to determine the activity of these two co-transcription factors. One of them is the visualization of the nucleocytoplasmic shuttling of YAP/TAZ. This method represents a quantitative and automatable analytical procedure to get information about the activity

Results

of these proteins [178, 179]. In this work, IF was applied using 308 keratinocytes expressing MnPV oncoproteins to determine the localization of endogenous YAP/TAZ (Figure 33 A). The IF showed an altered localization in MnPVE7- and MnPVE6E7- expressing cells. Here, the localization of Yap/Taz seemed to be more towards the nucleus compared to cells expressing MnPVE6 or the empty control plasmid.

To quantify the signals in the corresponding cell compartment, intensities of Yap/Taz and DAPI staining from 3 independent experiments (3 images of each experiment) were measured using ImageJ software. To calculate the ratio between nuclear and cytosolic signal intensity, the total signal intensity was calculated first, which served as the 100% signal intensity. Then, the cytosolic and

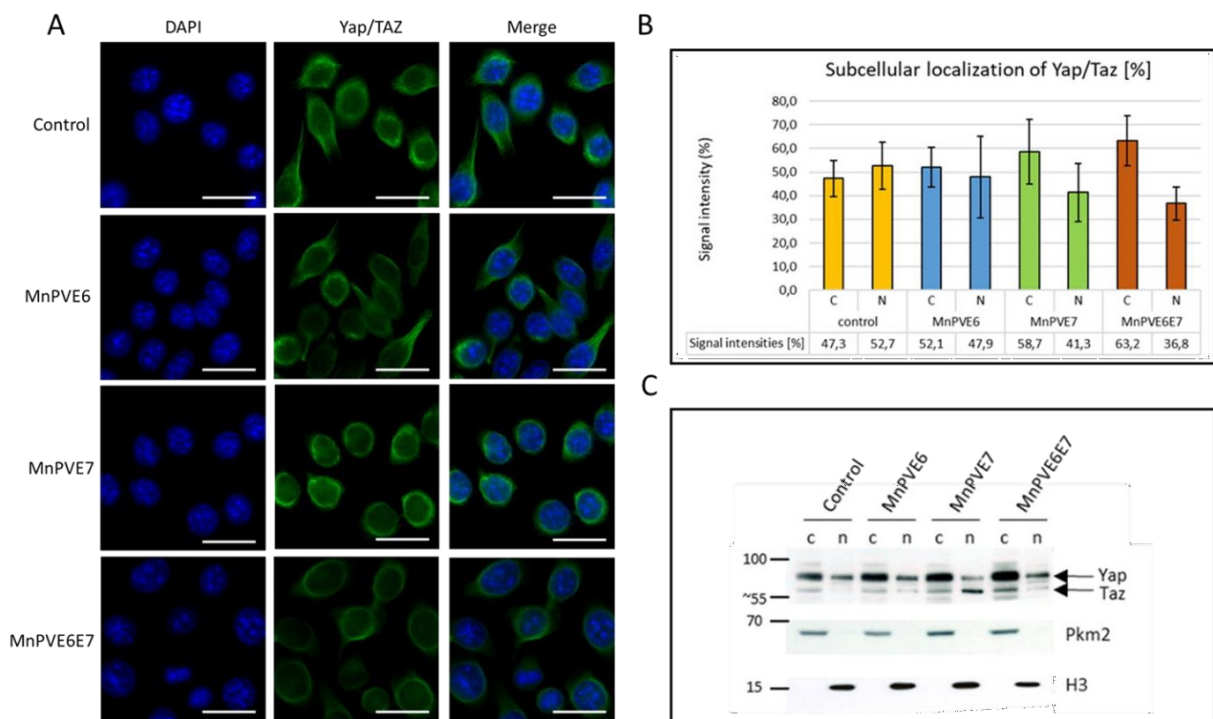


Figure 33: Translocation of Yap/Taz towards the nucleus. A) IF shows an altered localization of Yap/Taz in MnPVE7- and MnPVE6E7-expressing cells. The approach of Yap/Taz to the nucleus compared to the localization in control cells and MnPVE6-expressing cells is unambiguous. DAPI served as nuclear marker. Scale bars: 20 μ m **B)** Quantification of Yap/Taz signal intensity from IF using ImageJ illustrates the tendency of these proteins towards the nucleus in MnPVE7- and MnPVE6E7-expressing cells. DAPI signal was used as a nuclear marker. **C)** Cell fractionation was done to elucidate the localization of Yap/Taz in MnPV oncoprotein-expressing 308 keratinocytes. Here, an increased presence of Taz in nuclear fractions of MnPVE7-expressing cells compared to other cell lines can be observed. Histone H3 served as marker for nuclear fraction, Pyruvate kinase isozymes M1/M2 (Pkm2) was used as marker for cytosolic fraction. c = cytosol, n = nucleus.

nuclear signals were determined as percentage values. Using this quantification method, a clear tendency of the Yap/Taz localization towards the nucleus in MnPVE7- and MnPVE6E7-expressing cells was found (Figure 33 B).

To test whether a translocation of Yap or its homologue Taz happens, a nucleus/ cytoplasm separation of MnPV oncoprotein-expressing cell lines was performed and analyzed by WB (Figure 33 C). Here, Taz was found to be enriched in the nucleus in cells expressing MnPVE7. However, this effect could not be shown in cells expressing MnPVE6 or MnPVE6E7. But in general, an overall stronger signal intensity of Yap/Taz was shown compared to control, MnPVE6- or MnPVE7-expressing cells.

Thus, for the first time, an effect directly mediated by MnPVE7 on the cell could be described.

3 Summary of results

In the present thesis, the influence of MnPV on the host cell was investigated using, among others, the mass spectrometry-based interactomics and proteomics.

By semi-spatial proteomics, great differences between the different SCC subtypes of *Mastomys coucha* was shown in the proteome composition, depending on their level of differentiation. Especially naturally MnPV-induced benign tumors strongly differed from dedifferentiated nKSCCs developing after UV-irradiation. Furthermore, it is of particular interest that MnPV-infected tissue shows extremely large differences in the proteome composition compared to uninfected tissue or skin control. The influences on differentiation processes in infected cells could also be verified by IF staining against the differentiation marker K10.

In the following, the effect of MnPV-infection on keratinocytes was further characterized in detail by using *in vitro* proteomics. These studies identified a plethora of proteins influenced by the presence of oncoproteins from MnPV and HPV38. A significant effect on the important HIPPO signaling pathway found was used to verify these data.

By focusing on effects mediated by MnPV E6 and E7, proteomic analyses, WB and IF were performed. Here, a significant reduction of Wwp2, Cul7 and PtpN14 was observed in MnPVE7- and MnPVE6E7-expressing cells.

Interactome studies performed for MnPV- and HPV38- oncoproteins revealed the complex sites of action of these PV proteins within a cell. My analyses have shown that the PV proteins studied bind to cellular proteins involved in a variety of cellular pathways. Thus, they most likely influence a variety

Discussion

of biological processes, such as apoptosis, proliferation, and cell cycle control. By demonstrating for the first time the interaction of MnPVE7 with cellular PtpN14, a direct link between MnPV-infection to the HIPPO pathway was uncovered, in which this phosphatase plays a regulatory role.

Subsequent experiments showed that the MnPVE7-mediated influence on the HIPPO pathway impairs the localization of its main effectors Yap and Taz towards the nucleus. Further IF and nuclear/cytosol fractionation followed by WB uncovered that Taz is more abundant in the nucleus of MnPVE7-expressing cells while in MnPVE6E7 a general higher expression level of Yap/Taz was observed when compared to control.

In summary, the study provides new insights into SCC development *in vivo* (first time done for SCCs) and *in vitro*. In addition, a proteomic analysis was done for the first time to investigate the effect of HPV38 E6 and E7 on the host cell. In the interactome analysis, new and known interactors were found that explain how cutaneous PVs can facilitate SCCs.

4 Discussion

In recent years, the role of beta types in the development of skin cancer has been increasingly considered concluding, that cutaneous beta HPVs promote the development of SCCs *via* a hit-and-run mechanism in which PVs act together with the accumulation of UV-induced DNA mutations [44, 84]. Confirmation of this postulated system was achieved using the African mammalian rodent *Mastomys coucha*, which has proven to be a suitable animal model for the study of papillomavirus-associated skin carcinogenesis [2, 44].

Until now, however, it remained unclear which processes take place in an infected cell that ultimately lead to uncontrolled cell division. This led to the question which cellular proteins are affected in presence of viral proteins and what effects this interference has on cell homeostasis and on elementary signaling pathways.

This work provides first steps to answer these fundamental questions by using proteomics and interactomics, paving the way for more in-depth research on cutaneous PVs using *Mastomys coucha* as a preclinical animal model.

4.1 Proteomic analyses provide new in-depth insights into the virus-host cell interplay of MnPV

Proteins fulfill a wide range of tasks within a cell. Cellular properties essentially depend on the composition and structure of the totality of all proteins produced. Therefore, the analysis of the so-called proteome can provide information about various cellular processes [180].

Nowadays, proteomics are used in various fields of research [181]. The analysis of proteins as effectors of biological functions thus represents one of the most important pillars of modern biology for characterizing biological systems and describing relevant global changes [182].

During the last few years, using a variety of methods (reviewed in: [183]) including proteomic analyses [184-188] extensive new insights have been gained into how HPV interacts with its host cell. So far, however, limited is known about how cutaneous HPV types contribute to the development of skin cancer by interfering with cell homeostasis. In this work, proteomic studies were carried out to describe the processes involved in the development of NMSC in *Mastomys coucha* and to further elucidate the role of MnPV in this process.

The inter-/ and intra-tumoral heterogeneity in NMSCs was illustrated for the first time to investigate the hit-and-run mechanism. Therefore, proteome analyses revealed differences between the various tumor subtypes on a spatial and molecular level in correlation with the MnPV infection status and their morphology.

The tumor heterogeneity was already shown in a PCA analysis (Figure 10 A), displaying a comparison of the different proteome comparisons in dependency of the tissue origin. Here, a comparable large similarity of the overall proteome composition of well-differentiated tissue and control skin represented was described. Dedifferentiated tissues, on the other hand, appeared to have greater differences from the control skin, which was to be expected since the morphology of the two tissues already exhibits strong differences (Figure 9). This observation is supported by the known processes of dedifferentiation, in which progressive changes in cells leads to even greater differences compared to normal tissue, potentially resulting in aggressively growing tumor tissue (reviewed in: [189]). The differences found between well-differentiated and poorly differentiated tissues compared to normal skin (Figure 11 B and C) suggest the hypothesis that changes in proteome composition have a sustained and widespread effect on cell homeostasis leading to the multistep process of dedifferentiation, which ultimately causes tissue to degeneration.

Discussion

The effects of dedifferentiation and MnPV infection on the host cell were further elucidated by an IPA canonical pathway analysis (Figure 12). In general, only few reliable statements could be made about altered cellular pathways in the comparison between well-differentiated tissue and skin with less than 100 proteins significantly and biologically relevant altered (Figure 10 B). Since these proteins form the basis of the following pathway analysis, the initial data set was too small for IPA to carry out reliable and meaningful analyses. Assuming the morphological similarity of the two tissue types, it is obvious that minor differences were found between the proteome networks of these two tissue types.

The situation was different when comparing proteomes from the dedifferentiated tissues with those of control skin. Here, more than 240 proteins were found to be altered (Figure 10 B). The protein networks of these two tissue types show differences, which were displayed in a canonical pathway analysis (Figure 12 C). One of the altered pathways found was the tRNA charging, as a central mechanism of protein biosynthesis. This pathway was found to be significantly upregulated (z-score = 2.33) in dedifferentiated tissue, since among others, aspartyl-tRNA synthetase 1 (Dars1), glycyl-tRNA synthetase 1 (Gars1), lysyl-tRNA synthetase 1 (Kars1) and tryptophanyl-tRNA synthetase 1 (Wars1) were significantly upregulated in dedifferentiated tissue. Dysregulation of the protein synthesis machinery in cancer has significant implications for pathophysiology, including cancer development and progression [190]. Since t-RNA loading is a fundamental component of protein biosynthesis, it can be assumed that this central mechanism is disturbed in dedifferentiated tissue compared to control skin, supporting the hypermetabolic nature of these cancer cells (reviewed in: [191]).

Spatial proteomics also showed that MnPV infection has a deep impact on the host cell proteome, since a total of 571 proteins were found to be significantly altered in MnPV-positive tissue compared to control skin (Figure 10 B). The canonical pathway analysis (Figure 12 A) showed among others a significant downregulation of the mTOR signaling pathway in MnPV-expressing tissue (z-score = -1.89). The mTOR signaling pathway has multiple roles in the cell and controls elementary functions such as protein synthesis, cell division and cell proliferation [192] for instance. The signaling pathway, based on mTOR complex 1 (mTORC1) and mTOR complex 2 (mTORC2), induce a transition from the G1 to the S phase of the cell cycle and thus cell division [193]. mTOR inhibitors suppressing these signaling cascades [194], lead to G1 arrest and stop cell growth. Thus, these inhibitors are frequently used in tumor therapy (reviewed in: [192]) making it even more interesting that in MnPV-positive tumor tissue this signaling pathway is significantly downregulated when compared to skin control.

Interestingly, activation of the mTOR signaling pathway is a frequently described feature of HPV16-positive head and neck squamous cell carcinoma (HNSCC) (reviewed in: [195]). The fact that under the influence of cutaneous MnPV infection the opposite effect takes place, namely a downregulation of this pathway, may represent a kind of protective mechanism of the cell against the virus. By downregulating the activity of this pathway, the cell possibly represses the progression of the cell cycle and the associated virus protein synthesis and replication.

In contrast, the xenobiotic metabolism PXR signaling pathway was significantly upregulated (z-score 1.508) in MnPV-expressing tissue when compared to control skin (Figure 12 A). This is particularly interesting as this pathway appears to be downregulated in UV-induced well- (z-score = -2.00) and dedifferentiated tumor areas (z-score = -1.63). Therefore, upregulation of the xenobiotic metabolism PXR signaling pathway can be attributed to MnPV- infection, which is a particularly interesting observation with respect to inter-tumoral heterogeneity. Since the xenobiotic metabolism PXR signaling pathway has multiple influences on various cellular functions through its effector pregnane X receptor (PXR or NR1I2) [196-200] its dysregulation of this pathway can lead cancer development (reviewed in [201]). Until now, no relationship between PV infections and the xenobiotic metabolism PXR signaling pathway has been described. The extent to which this pathway is also affected in tumors with an HPV context has to be investigated in further studies. In any case, however, the work presented here represents a new approach to study inter-/ and intra- tumoral heterogeneity.

In addition to canonical pathway analyses, underlying upstream regulators were also determined by using IPA (Figure 13). These analyses are based on prior knowledge about the expected effects between transcriptional regulators and their target genes, which are stored in the Ingenuity® Knowledge Base, making it possible to predict transcription factors which is potentially altered in their activity. The upstream regulator analysis performed here revealed a potentially reduced activity of the tumor suppressor p53 in MnPV-expressing tissue when compared to control skin. This statement is based on the up- and downregulation profile of 88 proteins found in the named comparison. One of these is Cav1 which was found to be significantly downregulated ($\log_2FC = -1.32$) in MnPV-positive tissue when compared to skin control. Since reduced expression of mouse Cav1 has been described in dermal fibroblasts of embryonic homozygous mice with mutated p53 gene (knockout) [202], it can be assumed that the lower expression in MnPV-positive tissue is due to lower activity of p53.

P53 is a known degradation target of E6 of diverse HPV types [203]. Various studies have shown that the expression of E6 leads to the degradation of cellular p53 and that this contributes to the

Discussion

transformation properties of HPV (reviewed in: [204]). This activity is not the case for MnPVE6 as shown in previous studies [44]. The decreased activity of p53 might also be caused in by mutations in the *Trp53* gene. However, it is important to remember that no decreased levels of p53 were detected in MnPVE6- expressing cells. Therefore, potential mutations in *Trp53* may only affect the activity, but not the expression level of p53.

The demonstration of reduced p53 activity in MnPV-expressing tissues represents a new insight into the intracellular activity of this PV. Although the expression level of p53 is not directly affected by expression of MnPVE6, the virus appears to suppress the activity of p53 *via* a yet unknown process during natural infection. Interestingly, this effect was not found in the *in vitro* proteomic studies performed in this work using cells expressing E6 or E7. Thus, it can already be shown that the downregulated p53 activity is not due to the two oncoproteins. Further studies must be carried out to clarify how the suppression is induced by MnPV and which viral proteins are responsible for this.

The data from the spatial proteomics uncovered interesting cellular candidates altered in MnPV infected tissue. One of these is the differentiation marker K10. In the skin, differentiation markers are well described and mark a certain degree of cellular differentiation. Specific keratins, e.g. K10 [39] and keratin 14 (K14) [40], are expressed only in early steps of differentiating cells of epidermal layers while involucrin [41], for instance, is exclusively expressed in the uppermost layer of the epidermis, which allows the identification of terminally differentiated areas [42]. In proteomic analysis, K10 was found to be 4-fold reduced in MnPV-expressing tissue compared to control skin. IF stainings of *Mastomys* tissue confirmed the reduction in MnPV-expressing tissue, suggesting that MnPV has an impact on cell differentiation (Figure 14). This finding is in accordance with previous studies on HPV16 and HPV18, where a reduced expression of K10 could be observed *in vitro* in E7-expressing cells [205]. This effect on K10 could now be shown for the first time *in vivo* in MnPV-induced *Mastomys coucha* tissue, representing another example for intra-tumoral heterogeneity.

4.1.1 Proteomic analyses of MnPV-infected cells provide insights into canonical pathways which are altered by infection

Within the framework of the top-down approach carried out, the influences of a MnPV infection on the intracellular system were examined. Here, the lower complexity an *in vitro* system was utilized to precisely investigate the influences of MnPV on the host cell. For this purpose, MnPV-infected murine 308 keratinocytes [144] were proteometrically analyzed and IPA canonical pathway analyses were

carried out (Figure 16). A particularly noteworthy result of this pathway analysis was the predicted activation of the HIPPO pathway in MnPV-infected cells. The HIPPO pathway is a highly conserved pathway from *Drosophila* to Mammalia playing a central role in the regulation of organ size [145, 206, 207]. The main effectors of this pathway are the two transcriptional coactivators YAP and TAZ, which together with TEA domain family members (TEAD) transcription factors control the expression of various genes involved in cell proliferation, apoptosis and cell fate [208].

It is already known that different HPV types have a direct influence on the HIPPO pathway [150, 209] and thus support the transforming properties of some HPV types [150]. An influence of MnPV on this pathway has not yet been described and so represents a new central starting point for further analyses. Interestingly, a link between MnPV infection and the activity on the HIPPO pathway was also found in the MnPV oncoprotein-expressing system studied in this work. Here, a reduced expression of non-receptor tyrosine phosphatase 14 (PtpN14) was found in MnPVE7-expressing cells which is discussed in more detail in chapter 3.3.

4.1.2 The expression of MnPV and HPV38 oncoproteins affects the entire host cell proteome

The influence of MnPV, E6 and E7 oncoproteins on cell homeostasis was described in the context of this work by proteomic investigations.

For this purpose, *in vitro* proteomic analyses of MnPV and HPV38 E6, E7 and E6E7-expressing cells were performed (Figure 18). Cutaneous HPV type 38 was included in this study (Figure 24) as it can contribute, like MnPV in *Mastomys*, to the development of NMSC in humans *via* a hit-and-run mechanism in combination with UV light [84] and is therefore a particularly interesting candidate for placing the results from the *Mastomys* model to a human context. The investigation of the target cell proteome is one way to describe the influences of the abovementioned oncoproteins on the host cell.

Interestingly, comparing the effects at the proteome level, some similarities between MnPV and HPV38 could be identified (Figure 25). For example, Cullin7 (Cul7) was shown to be significantly downregulated in MnPVE6E7-expressing cells (Figure 22) as well as in HPV38E6E7-expressing cells.

These similarities are particularly noteworthy because the used experimental systems have significant differences. The most obvious one is the use of different cell lines. While for MnPV proteome studies murine 308 keratinocytes [144] were examined, normal oral keratinocytes [210] (NOKs) were used to

Discussion

investigate the influence of HPV38. In addition, cells were transduced using different lentiviral vectors, which may also have an influence on the protein expression profile of the cells. These differences probably led to a generally low level of global agreement in the IPA analyses carried out for the two sets of experiments, in which no cellular pathway was found to be affected by both HPV38 and MnPV. Nevertheless, the *in vitro*-based proteomic studies conducted here provide new insights into the influence of MnPV and HPV38 oncoproteins on the cell and revealed exciting new starting points for further studies, especially in single-candidate analyses like for Cul7.

Among other candidates, a significant downregulation of Cul7 in MnPVE6E7-expressing as well as in HPV38E6E7-expressing cells was detected in the *in vitro* proteome analysis (Figure 22 and Supplemental Table 4). For MnPV, this downregulation could be attributed to MnPVE7, but not to MnPVE6 (Figure 22). In addition, a CUL7 downregulation was observed in HPV38E6E7-expressing cells in the proteome analyses. However, no significant different expression levels of Cul7 could be shown

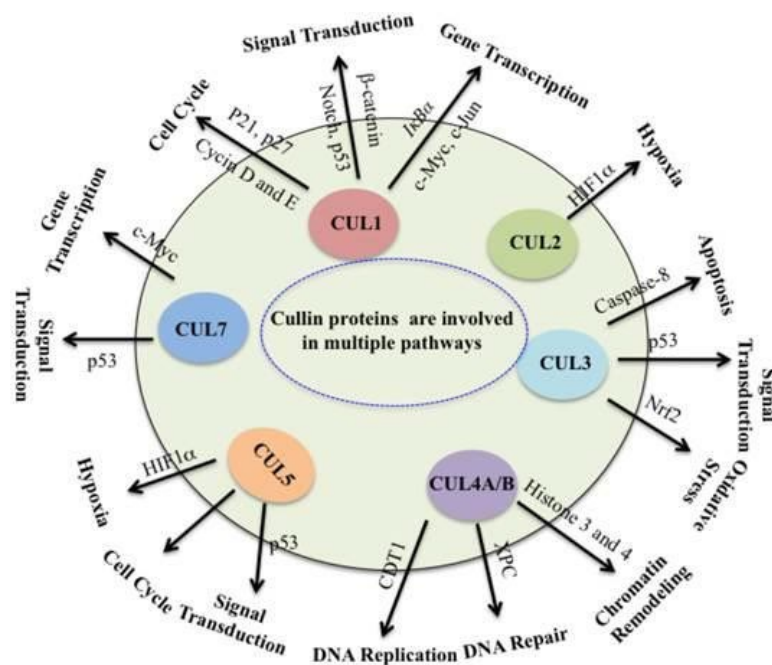


Figure 34: Members of the CUL-protein family influence various signaling pathways in the cell which are associated with the development of cancer. Figure adapted from: [5]

for HPV38E7, which is why further experiments are needed here to be able to attribute the observed effect to an oncoprotein of HPV38 (Supplemental Table 5).

CUL7 also known as p185 was discovered in 1994 [211]. Together with 5 others, it forms the family of CUL proteins. Unlike all other CUL proteins, CUL7 does not have a CUL repeat sequence [212]. Cullins are involved in various signaling pathways and influence a wide variety of biological functions like apoptosis, cell cycle control, gene transcription and signal transduction (reviewed in: [5]) (Figure 34). CUL7 is the core component of the 3M and Cul7-RING(FBXW8) complexes [160, 213] which mediate the ubiquitination of various target proteins [161, 214-216]. By influencing substrate stability, CUL7 can thus affect multiple signaling pathways, including processes controlling cell proliferation and cell cycle progression [217, 218]. Cullins in general represent crucial regulators of cell homeostasis [219]. Several studies have also shown a link between CUL7 and the development of tumors such as breast cancer [220], lymph node metastases [221] or colon cancer [222]. Here, CUL7 promotes cell growth and migration. Therefore, CUL7 is also referred to as a putative tumor-promoting protein. Additionally, CUL7 is known to bind directly to the p53 tetramerisation domain [223]. Functional analysis of this binding showed that p53 function was attenuated after DNA damage by CUL7 binding [224].

Interestingly, however, CUL7 appears to have a dual role. DeCaprio et al. were able to show a tumor-suppressing function of CUL7 using an SV40 antigen model system [225]. Nevertheless, further studies are needed to assess the postulated context-dependent dual role of CUL7 in different systems. In particular, the expression level of CUL7 in NMSC is not yet described. A connection between CUL7 and HPV infection has also not been shown so far making this protein a new, interesting target for further studies in the field of PV research. Especially, further research of the downstream effects of CUL7/Cul7 downregulation in HPV38E6E7- and MnPVE7-expressing cells will show how this affects cell homeostasis and might contribute to the formation of skin cancer.

In addition to Cul7, the WW domain containing E3 Ub-protein ligase 2 (WWP2) was also characterized in the proteomic analyses as significantly downregulated ($\log_2FC = -1.8$) in MnPVE6E7-expressing cells compared to control cells. This result was verified in IF analyses which showed that a downregulation of Wwp2 is not only observed in cells expressing MnPVE6E7, but also in cells expressing E7 only (Figure 21). Thus, the downregulation of Wwp2 seems to be an effect triggered by the oncoprotein E7 and that E6 is not significantly involved in this so far not described process.

WWP2 is an E3 ubiquitin protein ligase which influences various cell functions such as the translation in stem cells or the regulation of inflammatory processes by acting on the immune system.

Discussion

In addition to these properties, WWP2 has also been described as a novel oncogene as it appears to be associated with the formation of various forms of cancers [226-232] but so far, no studies have investigated the expression levels of WWP2 in NMSC. *In vitro* studies performed with different cell lines [231-233] revealed an accumulation of cells in the G1 phase when WWP2 was knocked down [228, 231]. Furthermore, a decreased expression of cell cycle dependent genes such as cyclin D1 and cyclin E was observed when WWP2 is decreased [228]. To date, there is no evidence on how inhibition of WWP2 function/expression affects proliferation, differentiation, or apoptosis functions in keratinocytes *in vitro*.

Thus, the results presented here are an interesting new starting point for further analyses that will elucidate the effect of downregulation of WWP2 in the PV-promoted NMSC context.

Interestingly, the described effects on Cul7 and Wwp2 could not be shown in MnPV-infected cells, which could have several reasons, e.g., the expression level of the oncoproteins, which is likely higher when controlled by a constitutive promoter than controlled by viral URR but has not been proven in detail may influence the effects on the cell. In a previous study (Dissertation of Rui Cao, 2021), the number of infected cells was estimated to be about 40% of the total cell population based on E4 stainings. This makes a direct comparison of effects between both experimental systems even more difficult.

The results of the proteome study of MnPV oncoprotein-expressing cells were placed in the biological context by an IPA pathway analysis (Figure 20). This showed that various cellular functions are impaired by the presence of the oncoproteins. Among others, a significant upregulation of the endocannabinoid cancer inhibition pathway in MnPVE6E7-expressing cells (z-score: 1.134) was found. Based on a decreased expression of G protein subunit alpha 13 (Gna13), which is a mechanistic target of rapamycin kinase (Mtor) and the regulatory associated protein of MTOR complex 1 (Rptor), IPA identifies the endocannabinoid cancer inhibition pathway to be upregulated in MnPVE6E7-expressing cells. Endocannabinoids are endogenous lipid signaling molecules of which the two best characterized are anandamide (AEA) and 2-arachidonoylglycerol (2-AG) [152]. These signaling molecules are natural or synthetic cannabinoids which inhibit the proliferation of cancer, stop the cell cycle and are able to induce cell death [153, 154]. These effects of endocannabinoids have been demonstrated both *in vitro* and *in vivo* in various malignant tumors [155, 156] but have not yet been described in the context of PVs. Endocannabinoids induce *de novo* synthesis of ceramides leading to activation of the ERK signaling cascade [234]. This promotes apoptosis and inhibits cell proliferation in various cancers

[235]. However, cannabinoids have a dual role. It has been shown that they are able to suppress the functions of the immune system [236]. Their otherwise cancer-fighting effects can be greatly impaired by this side effect. However, the extent to which the expression of MnPVE6 and E7 and the resulting increased activity of the endocannabinoid cancer inhibition pathway affect cell homeostasis remains to be clarified by further studies.

The proteomic data presented here showed great differences (Supplemental Figure 4). This could be due to various experimental aspects. First, the transfer of results from *in vitro* experiments to the *in vivo* situation is always a great challenge due to the great differences in the complexity [237]. Secondly, the use of mouse cells (308 keratinocytes) made a direct comparison with the data from the *Mastomys in vivo* study difficult since two different species were used. For the abovementioned reasons, it is easy to understand that the proteomic investigations made using *in vivo* and *in vitro* starting material are not directly comparable with each other. Nevertheless, these proteomic studies display interesting starting points for further studies that will address the question of what influence cutaneous papillomaviruses have on the cell and how this, together with UV light, can promote NMSC formation.

4.2 Interactome analyses of MnPV and HPV38 oncoproteins reveal interaction sites of oncoproteins with cellular proteins

Various approaches exist for the investigation of PV oncoprotein bound host cell proteins [238, 239]. Current studies use methods such as the Y2H system or affinity purification mass spectrometry to identify interaction partners of PV proteins (reviewed in: [80]).

To identify host cellular proteins interacting with MnPVE6 or E7, BioID and IP/MS were performed. An overlap of 24 proteins between the two data sets from BioID and IP was found for MnPVE7 interactors. For E6, only one protein (Ipo5) was characterized as an interactor in both methods which might be due to the overall small dataset revealed by BioID (41 interactors in total, Figure 27)). The fact that a comparatively small data set of potential interactors for MnPVE6 was found using BioID may be due to the fact that the MnPVE6-BirA* showed a generally low biotinylation rate (Supplemental Figure 2) compared to MnPVE7-BirA* and the control GFP-BirA*. It is also possible that MnPVE6-BirA* is less expressed or that biotinylation is affected by proteins bound to the fusion protein. Also, the

Discussion

localization of the construct within the cell may play a role in the effectiveness of the reaction (number of available proteins).

Comparing the interactomes of MnPV and HPV38 oncoproteins, it is noticeable that generally only a few proteins can be described as common interaction partners of the respective PV oncoproteins (Figure 31). The highest commonality is given comparing the results of the IP study of the MnPV oncoproteins with the BioID results of the HPV38 oncoproteins. This is probably due to the generally larger interactome data set described in the IP studies.

One of the candidates found in the IP for HPV38E6 and MnPVE6 is Maml1, which was additionally verified for MnPVE6 in an IP followed by WB (Figure 30). Maml1 has already been described as a binding partner of both MnPVE6 [175] and HPV38E6 [176], further confirming the correctness of the data shown here. Therefore, the presented study provides far-reaching insights into the binding partners of MnPVE6 and E7 for the first time and can be considered as a milestone for the detailed description of MnPV host cell interaction. In addition, there is further evidence for the comparability of the interaction points of MnPV and cutaneous HPVs with their respective host cells.

4.2.1 Confirmation of MnPVE6 interaction with Maml1 and newly discovered interaction with Smad2/3

In addition to many other interactors, Maml1 was verified as a cellular interaction partner of MnPVE6 in IP/MS. This result is in line with a large-scale interaction study from 2017, in which 45 different E6 proteins from various PVs were investigated for their binding properties to MAML1 and E6AP [175]. Here, it was shown that the vast majority of E6 proteins bind either to MAML1 or to E6AP. An oncoprotein that had both cellular proteins as binding partners could not be found in the performed IP with subsequent WB [175]. This is consistent with the results from the interactome study conducted here. Neither the BioID nor the IP with subsequent MS analysis identified E6AP as interaction partner of MnPVE6.

MAML1 is a transcriptional coactivator of NOTCH signaling pathway, which plays a crucial role in epithelial differentiation processes [240] and therefore is a necessary factor in maintaining the natural barrier function of the skin [241].

In PV-uninfected skin, NOTCH signaling is regulated by cell-cell contact [242]. Extracellular proteins bind to NOTCH receptor proteins which induce a conformational change of NOTCH, releasing the

fragment Intracellular NOTCH (ICN) to the intracellular space. ICN can then form a complex together with RBPJ and the co-activator MAML1 to specifically repress genes. Target genes of the NOTCH signaling pathway include Hairy and Enhancer of Split (HES) genes, MYC (coding for c-myc) and CCND1 (coding for cyclin D1) (reviewed in: [243]). However, it is important to notice that NOTCH target genes are lineage specific, and NOTCH target genes of differentiating keratinocytes have not been well characterized so far.

In 2012 it was described that MAML1 is a cellular interaction partner of many beta HPV types as well as *Mus musculus* papillomavirus 1 (MmuPV1) [244, 245] and that this binding is associated with inhibition of NOTCH signaling in various *in vitro* and *in vivo* contexts. HPV8E6 binds to MAML1 *via* the LXXLL motif [176, 245]. The exact function of this domain is unknown, but the TAD1 domain of MAML1 is able to bind to p300 [246]. It is currently assumed that binding of E6 to TAD2 of MAML1 can effectively inhibit the expression of NOTCH target genes on the one hand [176] and on the other hand impede the association of p300 with TAD1 of MAML1. Binding of MnPVE6 to p300, which has already been described for many HPV types as well [82, 90, 247], would then not be necessary to inhibit NOTCH signaling effectively. However, this hypothesis needs to be verified by further experiments.

In immunodeficient nude mice [248], an intact binding site of E6 to MAML1 was necessary for the outgrowth of papillomas and carcinomas in experimentally MmuPV1- infected animals [249]. As a result of this disruption of the NOTCH signaling pathway, keratinocyte differentiation was found to be reduced and cell cycle arrest was found to be inhibited, which is considered to be an important point in the differentiation process of cells [240].

To determine which effect, the interaction between MnPVE6 and MAML1 on the NOTCH signaling pathway and the differentiation processes has needs to be carried out in further experiments. However, it is obvious that there is a connection between the expression of MnPV proteins and the expression of intracellular differentiation markers such as K10 which could be shown in IF stainings and spatial proteomics (Figure 14).

In addition to Maml1, Smad2 and Smad3 were also identified as interaction partners of MnPVE6. These proteins are the main components of the TGF-beta transduction pathway which has been shown to induce epithelial stemness and to control proliferation in differentiating keratinocytes [250-252]. TGF-beta has a tumor suppressor activity in epithelial cells and mutations in this pathway are common in epithelial tumors [253-255]. In addition, TGF-beta is a factor in epithelial to mesenchymal

Discussion

transmission (EMT) and causes increased expression of metalloproteases and is associated with increased migration and invasion of human keratinocytes [256].

The interaction of E6 proteins with SMAD2/3 has previously been described for various HPV types as well as MmuPV1E6 [244, 257]. An illustration of the effect of E6 binding to SMAD2/3 is shown in the

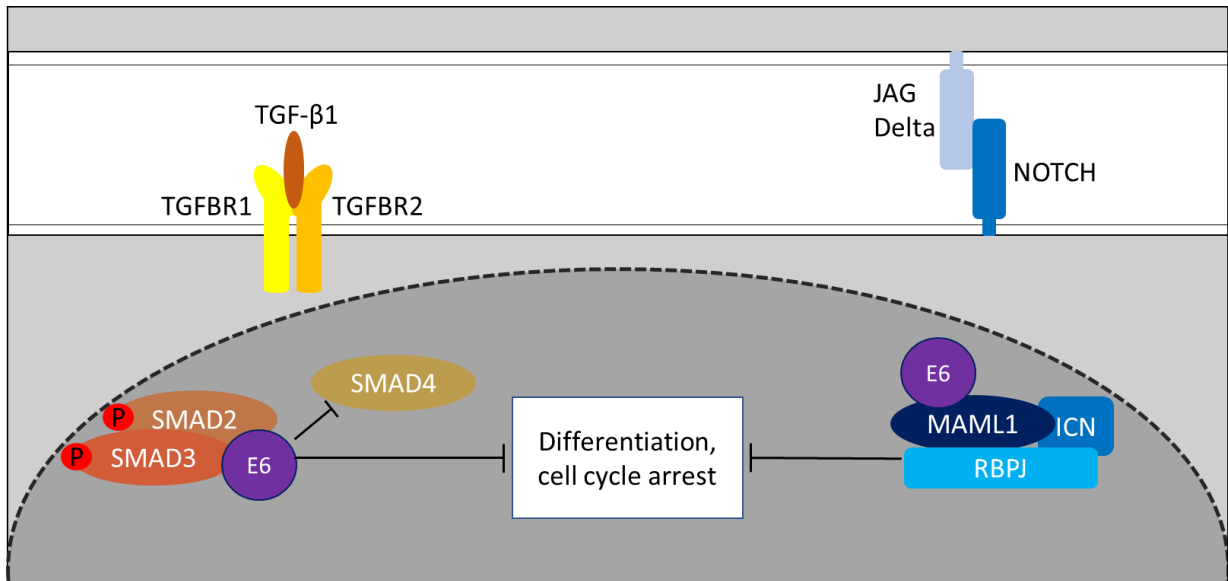


Figure 35: Hypothetical consequence of MnpVE6 binding to MAML1 and SMAD2/3 on NOTCH and TGF- β signaling pathway. The proven binding of MnpVE6 to SMAD2/3 could prevent binding to co-SMAD4, which could subsequently lead to a blockade of differentiation processes (left part). In addition, it is possible that this effect is achieved by MnpVE6 binding to Maml1 (right part).

left part of Figure 35. In order to clarify whether the newly discovered interaction of MnpVE6 and SMAD proteins leads to a dysregulation of the TGF-beta signaling pathway, further experiments are needed.

Taken together, the results from the interactome study for MnpVE6 demonstrate for the first time the binding of MnpVE6 to Smad2/3 and Maml1 in *Mastomys* cells. The identification of Maml1 and Smad2/3 as interaction partners of MnpVE6 lead to potential mechanisms which may be involved in MnpV contribution to skin cancer formation in *Mastomys coucha*.

4.2.2 PtpN14 is a novel discovered interaction partner of MnpVE7

PTPN14 is a non-receptor tyrosine phosphatase with a mass of approximately 135 kDa. It is characterized by an N-terminal FERM domain and a C-terminal catalytic domain. In the middle part of

the protein are two proline-rich motifs (PPXY) [258, 259] which allow binding of PtpN14 to WW domain-containing proteins. Such proteins include YAP and Kibra [177, 260]. In addition, this phosphatase is able to bind to cytoskeletal and plasma membrane proteins *via* the FERM domain [261].

PtpN14 was described as an interaction partner of HPV16 and HPV18 E7 in 2016, which could be additionally demonstrated in the following studies on various E7 proteins of different PVs [79]. Also, the binding site of HPV18E7 to PTPN14 catalytic domain could be shown by structural analysis [262].

Within interactome study carried out here, the binding of MnPVE7 and PtpN14 was demonstrated for the first time. This interaction could be shown in both BioID and IP/MS. In addition, the binding could be verified by IP with subsequent WB. Binding of HPV38E7 to PTPN14 could not be shown in this work using BioID, which is in line with already known results from previous studies on interactome of various HPV types, in which PTPN14 could also not be shown as an interaction partner of HPV38E7 [79]. The resulting effects of MnPVE7 binding to PtpN14 are further described in more detail in chapter 3.3.

4.3 Influence of MnPVE7 on the HIPPO pathway through the binding to PtpN14

In this work, a reduction in the expression of PtpN14 under the influence of MnPVE7-expression was demonstrated. This was shown in the proteome analyses by a significant, 4-fold reduction ($\log_2FC = -2.03$) of the PtpN14 expression level MnPVE6E7-expressing cells as well as in WB and IF (Figure 32). Here, it turned out that in MnPVE6E7- as well as in MnPVE7-expressing cells, a reduction of this phosphatase can be observed, which allows the conclusion that this effect is maintained by MnPVE7. Furthermore, the question arose what effect the downregulation of PtpN14 by the oncoprotein has on the host cell homeostasis. Therefore, the regulatory role of PtpN14 in the HIPPO pathway was examined in more detail.

The HIPPO signalling pathway plays a crucial role in various cellular processes such as cell proliferation, survival, mobility, stemness and cellular differentiation (reviewed in: [206]). This pathway is considered as highly conserved from *Drosophila melanogaster*, where it was described first, to Mammalia. The main components of the HIPPO pathway are kinases, which control the activity of the pathway and its effects within the cell through a phosphorylation cascade. The serine/threonine kinases MST1/2 first form heterodimers with Salvador Family WW Domain Containing Protein 1

Discussion

(SAV1) [263, 264] *via* their SARAH domains. This interaction is necessary to enable phosphorylation of MOB kinase activator 1A (MOB1A) and the Serine/threonine-protein kinases LATS1/2 [265]. LATS1/2 directly phosphorylates the main effectors of the HIPPO pathway Yes-associated protein (YAP) and Transcriptional co-activator with PDZ-binding motif (TAZ) at multiple sites and can thus control the localization of these transcriptional coregulators [266]. A simplified representation of the signaling cascade of this pathway is shown in Figure 36. It is important to consider, that the activity of this pathway is a dynamic process, which is why the representation in Figure 36 is intended to be a simplified illustration of the cascade but is not the underlying real situation in the cell.

When the HIPPO pathway is activated, it inhibits tissue growth and cell proliferation by phosphorylating the effectors YAP/TAZ which remain in the cytosol where they bind to cytosolic

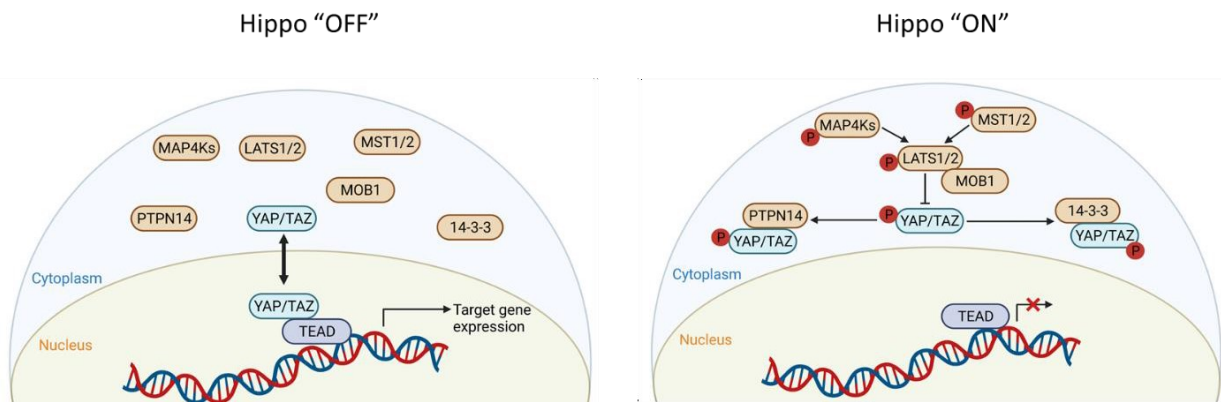


Figure 36: Core components of the HIPPO signaling pathway in mammals base on the dynamic change in localization of the two main effectors YAP and TAZ between nucleus and cytoplasm. When the pathway is "OFF", YAP and TAZ are present in a dephosphorylated state and accumulate in the nucleus, where, together with TEADs, they control the gene transcription of target genes. When the pathway is active ("ON"), YAP and TAZ are present in a phosphorylated state. Thus, they can bind to cytoplasmic proteins such as 14-3-3 and PTPN14, which leads to their cytoplasmic retention and degradation. This signaling pathway is always dynamically regulated. An exclusive "ON" or "OFF" state is rarely achieved, which is why the representation shown here should be seen as a simplification of the real situation within a cell. Figure modified from: [9]

proteins such as 14-3-3 [267] and PTPN14 [259]. If the HIPPO pathway is turned off, YAP/TAZ are dephosphorylated. At this stage, they translocate into the nucleus where they bind to TEAD transcription factors. This induces transcriptional programs that are important for cell proliferation, survival, and migration. In the absence of YAP/TAZ, TEAD acts as a standard repressor and represses the expression of the corresponding target genes [268-270].

In this work, an altered localization of Yap/Taz in MnPVE7- and MnPVE6E7-expressing keratinocytes was observed in IF (Figure 33). Quantitative measurements revealed a tendency of Yap/Taz localization towards the nucleus in MnPVE7- and MnPVE6E7-expressing cells (Figure 33). Interestingly, these cell lines also showed decreased expression of PtpN14, suggesting that the lower expression of PtpN14 advocates localization of these HIPPO effectors towards the nucleus. This effect has already been shown in HPV16 and HPV18 E7-expressing keratinocytes [271]. It was found that binding of E7 to PTPN14 induced proteasomal degradation of this protein, making binding to the HIPPO effector YAP no longer possible [205]. Thus, activated YAP/TAZ translocate towards the nucleus in E7-expressing cells where it extended the lifespan of primary keratinocytes [205]. In addition, genomic data from human cancer genome analyses revealed a more frequent mutation rate of HIPPO pathway components in HPV-negative tumors than in HPV-positive HNSCC [272].

Differences in binding affinity between high-risk and low-risk HPVs and the resulting effect on the cell have already been described. While in high-risk types the binding of E7 to PTPN14 lead to proteasomal degradation and therefore lower expression level of PTPN14, a change in expression level was not observed in cells expressing low-risk HPV types [271, 273].

A recently published study showed that YAP/TAZ is activated under the influence of HPV16 and 18 and, together with TEAD, is required for the carcinogenic activity of HPV E7. In addition, it was shown that basal epithelial cells remain in a proliferative stage due to the expression of E7 [205].

The two paralogues YAP and TAZ are transcriptional coactivators with 46% amino acid identity [274]. Thereby, great similarities between the available binding sites of these proteins and the resulting binding possibilities arise (Figure 37). Both proteins control cell proliferation and regulate organ size [9, 275]. They also play an important role in cellular stress, where they control cell survival. YAP/TAZ are required for embryonic tissue growth, wound healing, and organ regeneration [275-277]. *In vivo*, loss-of-function experiments have shown that YAP/TAZ activity in adult tissues such as skin is not essential for the maintenance of cell homeostasis [278-281]. In addition to that, YAP/TAZ also have important functions in the induction of epithelial-to-mesenchymal transition (EMT) [282-284], regulation of heart development and many more [285-290].

Discussion

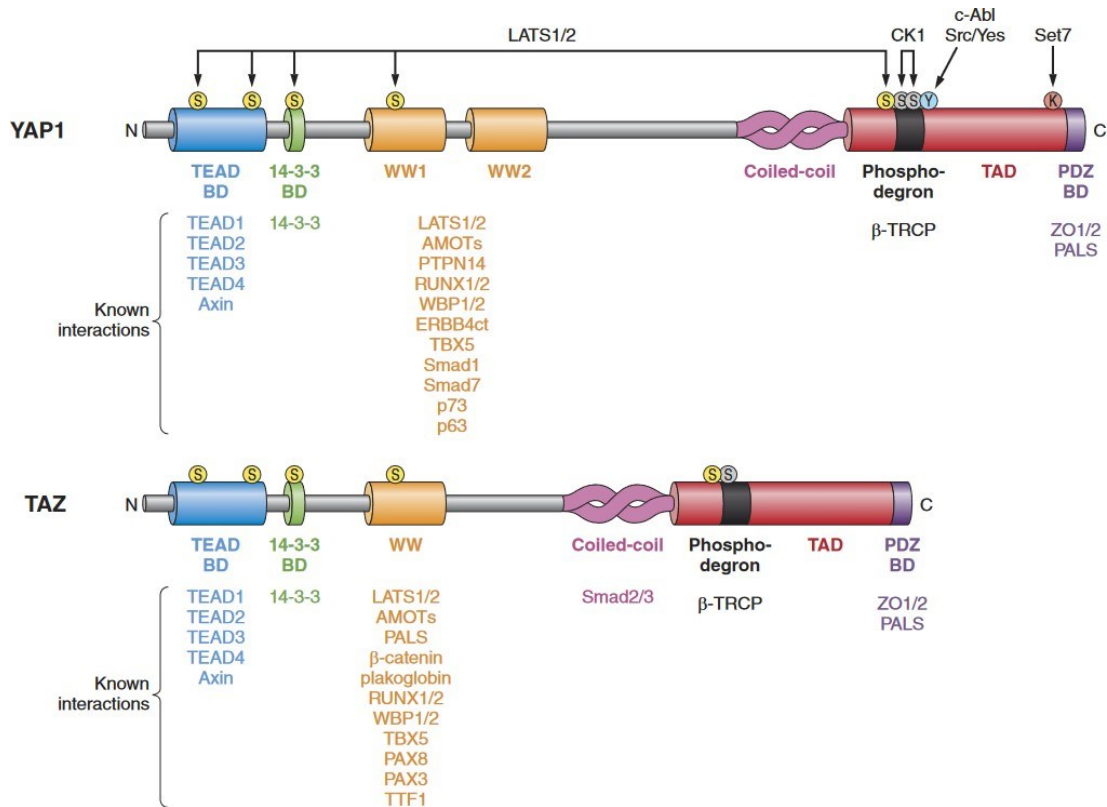


Figure 37: Schematic representation of the domains of YAP and TAZ as well as their interactors and interaction binding sites. A total of five serines (S) of YAP correspond to four S of TAZ. Serines activated by LATS1/2 phosphorylation are colored in yellow. BD: binding domain. TAD: transcription activation domain. Figure adapted from: [4]

Within this thesis, nuclear/cytoplasmic separation was performed showing that Taz is more abundant in the nucleus than in the cytoplasm in MnPVE7-expressing cells. Most of the available literature attributes functional redundancy to YAP and TAZ [291, 292]. However, there is also evidence that the two co-transcription factors show a context dependency, which can even lead to opposing roles of YAP and TAZ (reviewed in: [293]). In squamous epithelial cells, activation of YAP and TAZ can equally promote basal cell proliferation, while inhibition of the activity of these proteins induces keratinocyte differentiation [294-299]. A different role of the two proteins within adult skin has not yet been described. Therefore, YAP and TAZ can be considered as equivalent regulators of epithelial differentiation processes.

Interestingly, the effect of increased nuclear presence of Yap or Taz could not be detected in MnPVE6E7-expressing cells. This unexpected observation allows various hypotheses of the possible underlying effects. It might be the case that MnPVE6 enhances the binding of Yap/Taz to cytoplasmic

proteins such as PtpN14 [300]. However, an indirect influence of MnPVE6 on the translocation of Yap/Taz is more likely, as in the interactome studies performed here PtpN14 had not been found to bind to MnPVE6. A particularly noteworthy fact is the predicted activation of the HIPPO pathway in MnPV-infected cells (Figure 16). Thus, an effect on this pathway could be demonstrated in two different systems within this work.

It is already known that some HPV types have a direct influence on this pathway [150, 209] and thus support the transforming properties of some HPV types [150]. An influence of MnPV on this pathway has not yet been described and thus represents a new central starting point for further analyses which are needed to elucidate the context-dependent role of Yap/Taz in MnPV infected *Mastomys coucha* tissue. However, the description of important basic implications on mechanistic effects of MnPV infection represents an elementary contribution to a deeper understanding of the development of skin tumors under the influence of cutaneous PVs. Thus, the HIPPO signaling pathway with its effectors YAP and TAZ could be assigned a central role in the development of NMSC for the first time.

5 Summary of the Discussion

In the context of the work presented here, new insights into the interplay between MnPV and the target cell were uncovered using multiple different techniques.

For the first time, spatial proteomes from different NMSC tumor subtypes were described within this thesis uncovering huge differences in the protein expression patterns of the individual tumor subtypes. This brought new profound insights into the inter-/ and intra- tumoral heterogeneity of NMSCs.

Additional interactome studies using BioID and IP/MS revealed multiple host cellular interactors of the MnPV oncogenes. Here, Maml1 was confirmed as a binding partner of MnPVE6, and new interaction partners such as SMAD2/3 were described for the first time. In addition, PtpN14 was identified as a binding partner of the second oncoprotein MnPVE7, again demonstrating the similarity of the cutaneous PV type studied here with extensively described HPV types. This fact further supports the use of *Mastomys coucha* as a preclinical model system for the investigation of skin tumor development.

Using a top-down approach, an effect of MnPV on the HIPPO signaling pathway was observed in MnPV-infected cell systems. Alterations in Hippo signaling elements have already been identified in HPV-related cancers [205, 301]. In transduced murine keratinocytes, the effect on the HIPPO pathway could be attributed to the oncoprotein E7 which reduces the expression level of PtpN14, a phosphatase which belongs to the HIPPO pathway. Due to its reduced expression level, the main effector of the HIPPO pathway, Yap/Taz was increasingly translocated towards the nucleus in MnPVE7- and MnPVE6E7-expressing cells. This effect could be shown here for the first time for a cutaneous PV type. On closer examination of the abovementioned effect, translocation in MnPVE7-expressing cells could be restricted to Taz.

The analysis of candidates influenced by MnPVE6 and/or E7, partly by interaction, as well as their influence on intracellular signaling pathways showed that these oncoproteins can profoundly disrupt the cellular homeostasis. Thus, MnPV can force the development of NMSC, which together with UV can lead to malignancy and dedifferentiation of tissue. This eliminates the need for the continued presence of the virus for the progressive process of tumor development, referred as hit-and-run mechanism. Thus, my study represents a starting point for further exciting investigations using the preclinical *Mastomys* model system on PV related NMSC development research.

6 Material

6.1 Chemicals and reagents

2-Propanol Merck	Calbiochem, Darmstadt
6 × DNA Loading Dye	Fermentas, St. Leon-Rot
Acetic acid	Merck Calbiochem, Darmstadt
Acrylamide-Bis (29:1), 30% solution	Serva Feinbiochemica, Heidelberg
Agarose	Sigma-Aldrich, Steinheim
Ammonium acetate	Merck Calbiochem, Darmstadt
Ammonium bicarbonate	Sigma-Aldrich, Steinheim
Ammonium persulfate	Sigma-Aldrich, Steinheim
Aqua ad iniectabilia	Braun, Melsungen
Bradford Reagent	Bio-Rad Laboratories, München
Bromophenol blue	Serva Feinbiochemica, Heidelberg
BSA	New England BioLabs, Frankfurt
Complete Protease Inhibitor Cocktail	Roche, Mannheim
DMSO	Carl Roth GmbH, Karlsruhe
dNTPs Set PCR Grade	Invitrogen, Karlsruhe
ECL Super Signal West Femto	Thermo Fisher Scientific, USA
Enhanced Chemiluminescence Substrate (ECL)	PerkinElmer, USA
Ethanol, absolute	Merck Calbiochem, Darmstadt
Ethidium bromide, 1% solution	Fluka, Steinheim
Glucose	Carl Roth GmbH, Karlsruhe
Glycerol	AppliChem, Darmstadt
Glycine	Gerbu, Gaibach
Hydrochloric acid	Carl Roth GmbH, Karlsruhe
KCl	Merck Calbiochem, Darmstadt
KH ₂ PO ₄	Carl Roth GmbH, Karlsruhe
Methanol	Sigma-Aldrich, Steinheim

Material

MgCl ₂	Merck Calbiochem, Darmstadt
MgSO ₄	Serva Feinbiochemica, Heidelberg
Milk powder	Carl Roth GmbH, Karlsruhe
Na ₂ HPO ₄	Carl Roth GmbH, Karlsruhe
Na ₃ VO ₄	Sigma-Aldrich, Steinheim
NaCl	Sigma-Aldrich, Steinheim
NaF	Sigma-Aldrich, Steinheim
NaOH	Carl Roth GmbH, Karlsruhe
Nonidet® P-40	Sigma-Aldrich, Steinheim
Protease Inhibitor Cocktail Complete, EDTA-free	Roche, Mannheim
Protein A/G PLUS-Agarose beads	Santa Cruz, Heidelberg
RiboLock RNase inhibitor	Thermo Scientific, St. Leon-Rot
SDS, Ultra-pure	Carl Roth GmbH, Karlsruhe
Sodium deoxycholate	Merck Calbiochem, Darmstadt
Sucrose	Carl Roth GmbH, Karlsruhe
TEMED	Sigma-Aldrich, Steinheim
Triton® X-100	Serva Feinbiochemica, Heidelberg
Trizma base (Tris)	AppliChem, Darmstadt
Tween® 20	Gerbu, Gaibach
Urea	Carl Roth GmbH, Karlsruhe
β-Mercaptoethanol	Carl Roth GmbH, Karlsruhe

6.2 Reagents for Bacteria Cultivation

Ampicillin	Sigma-Aldrich, Steinheim
Bacto™ Agar	Becton Dickinson, Heidelberg
Bacto™ Trypton	Carl Roth GmbH, Karlsruhe
Kanamycin	BIOTREND Chemikalien, Cologne
LB Medium	Carl Roth GmbH, Karlsruhe
Doxycycline	Sigma-Aldrich, Steinheim

6.3 Reagents for cell culture

0.25% Trypsin/EDTA	Invitrogen, Karlsruhe
Biotin	Thermo Fisher Scientific, Darmstadt
Dulbecco's Modified Eagle's Medium (DMEM)	Sigma-Aldrich, Steinheim
Dulbecco's Phosphate Buffered Saline (PBS)	Invitrogen, Karlsruhe
Fetal Bovine Serum (FBS)	Linaris GmbH, Wertheim
Keratinocyte SFM Medium	Invitrogen, Karlsruhe
MG132 Merck	Calbiochem, Darmstadt
Opti-MEM serum-free medium	Invitrogen, Karlsruhe
polybrene	Santa Cruz Biotechnology
Polyethylenimine 25 kDa linear (PEI)	Polysciences Europe GmbH, Hirschberg an der Bergstrasse
Puromycin	Sigma-Aldrich, Steinheim
Penicillin/Streptomycin (100 x)	Thermo Fisher Scientific, Darmstadt
Supplements for Keratinocyte SFM Medium	Invitrogen, Karlsruhe
Trypan blue	Biochrom, Berlin
Turbofect <i>in vitro</i> Transfection Reagent	Thermo Fisher Scientific, Darmstadt
Hank's Balanced Salt Solution (HBSS) 10 x	Thermo Fisher Scientific, Darmstadt
Incubator-Clean	VWR International, Darmstadt
MEM amino acids (50x)	Biochrom, Berlin
MEM vitamins (100x)	Thermo Fisher Scientific, Darmstadt

Material

Table 1: Composition of the 308 keratinocyte medium. Mixture of Hanks 10 x and H₂O is prepared and autoclaved previously to the addition of the other components. Final volume of the prepared medium is 528 ml with a pH ~ 7.3

Additive	Volume [ml]	Concentration [%]
Hanks 10 x	40	7.575
H ₂ O	345	64.341
MEM vitamins 100 x	16	3.03
MEM amino acids 50 x	32	6.061
NEAA 100 x	16	3.03
L-Glutamine 200 mM	4	0.758
NaHCO ₃	16	3.03
Pen/Strep	5	0.947
HCl 4 M	1.7	0.34
FCS 10 %	50	9.47

6.4 Kits

CloneJET PCR Cloning Kit	Thermo Fisher Scientific, Darmstadt
GeneJET Plasmid Miniprep Kit	Thermo Fisher Scientific, Darmstadt
QIAGEN® Plasmid Midi Kit	Qiagen, Hilden
QIAquick® Gel Extraction Kit	Qiagen, Hilden
RNeasy® Mini Kit	Qiagen, Hilden
TURBO DNA-free™ Kit	Thermo Fisher Scientific, Darmstadt

6.5 DNA and protein size markers

GeneRuler™ 1 kb DNA Ladder	Thermo Fisher Scientific, Darmstadt
PageRuler™ Plus Prestained Protein Ladder	Thermo Fisher Scientific, Darmstadt

6.6 Universal enzymes

DreamTaq™ Green DNA Polymerase	Thermo Fisher Scientific, Darmstadt
FastAP Thermosensitive Alkaline Phosphatase	Thermo Scientific, St. Leon-Rot
iTaq™ Universal SYBR® Green Supermix (2 ×)	Bio-Rad, München
Phusion® High-Fidelity PCR Master Mix (2 ×)	New England Biolabs, Frankfurt
RevertAid Reverse Transcriptase	Thermo Fisher Scientific, Darmstadt
T4 DNA Ligase	New England BioLabs, Frankfurt
NEBuilder® HiFi DNA Assembly Cloning Kit	New England BioLabs, Frankfurt

6.7 Restriction enzymes

FastDigest SbfI	Thermo Fisher Scientific, Darmstadt
FastDigest MluI	Thermo Fisher Scientific, Darmstadt
FastDigest BamHI	Thermo Fisher Scientific, Darmstadt
FastDigest Sall	Thermo Fisher Scientific, Darmstadt
FastDigest EcoRI	Thermo Fisher Scientific, Darmstadt
FastDigest SpeI	Thermo Fisher Scientific, Darmstadt
FastDigest XhoI	Thermo Fisher Scientific, Darmstadt

6.8 Consumables

Amersham™ Hybond™ P 0.45 PVDF	Th. Geyer, Renningen
Capillary tips (200 µl)	Biozym, Hessisch Oldendorf
Cell culture dishes (6, 10, 14 cm)	Greiner, Frickenhausen
Cell culture flasks (25, 75, 175 cm ²)	Greiner, Frickenhausen
Cell culture plates (6, 12, 24, 96 well)	Greiner, Frickenhausen
Cell scraper Corning	Sigma, München
Cryo Tubes	Thermo Fisher Scientific, Darmstadt
Gloves (Microflex® XCEED)	MICRFLEX, USA
Incidin® Foam	Ecolab Deutschland, Monheim am Rhein

Material

Luer-Lock Syringe (50 ml)	Terumo Detuschland, Eschborn
Minisart Syringe Filter	Sartorius, Göttingen
Multiplate™ PCR Plates 96-well, clear	Bio-Rad, München
Needles, sterile (18G, 20G, 25G, 27G)	Braun, Melsungen
Optical Adhesive Covers MicroAmp	ABiosystems, Foster City, USA
PCR SingleCap 8er Soft Strips	Biozym, Hessisch Oldendorf
Pipette Tips (10, 200, 1,000 µl)	Steinbrenner, Gießen
Pipette Tips RAININ LTS (20, 200, 1,000 µl)	Mettler-Toledo GmbH, Gießen
Pipette Tips RAININ LTS sterile with filter (20, 200, 1,000 µl)	Mettler-Toledo GmbH, Gießen
Reaction Tubes (0.5, 1.5 and 2.0 ml)	Eppendorf, Hamurg
Reaction Tubes (15 and 50 ml)	Greiner, Frickenhausen
Special autoclavable bags	Nerbe plus GmbH, Winsen/Luhe
TipOne sterile pipette filter tips	Starlab, Ahrensburg
Whatman 3 mm filter paper	GE Healthcare, Munich
X-ray films Super RX	Fuji, Japan
Fixogum Rubber Cement	Marabuwerke GmbH & Co KG, Tamm
Objektträger Superfrost® Plus	Carl Roth GmbH, Karlsruhe
Low Bind Proteins tubes (0.5, 1.5 ml)	Thermo Fisher Scientific, Darmstadt

6.9 Laboratory equipment

Analytical scale ABJ-120-4NM	Kern & Sohn GmbH, Balingen
Autoradiography Cassettes	Kodak, Stuttgart
Bacterial shaker G25 Infors	Bottmingen, CH
Centrifuge Heraeus Fresco 17	Thermo Fisher Scientific, Darmstadt
Centrifuge Heraeus Pico 17	Thermo Fisher Scientific, Darmstadt
Centrifuge Megafuge 1.0R	Heraeus, Hanau
Centrifuge Rotina 380R	M&S Laborgeräte, Wiesloch
Centrifuge Sprout	Biozym, Hessisch Oldendorf
CFX96 Touch Real-Time PCR detection system	Bio-Rad, München

Confocal Olympus FluoView FV1000	Olympus, Hamburg
Developing machine CURIX 60	AGFA, Cologne
Easy-Cast™ Electrophoresis System	Thermo Fisher Scientific, Darmstadt
EVOS® XL Core Imaging System	Thermo Fisher Scientific, Darmstadt
Freezer profi line	Liebherr, Ludwigshafen
Freezer VIPTM Series -86°C	Sanyo, USA
Fridge Premium	Liebherr, Ludwigshafen
Incubator C200	LaBoTect, Göttingen
Kern EMB 1200-1 Tischwaage 1200 g	KERN & SOHN GmbH, Balingen
Magnetic stirrer MR3000	Heidolph Instruments, Schwabach
Microscope Olympus CK2	Olympus, Hamburg
Microwave	DéLonghi GmbH, Seligenstadt
Mini Trans-Blot® Cell	Bio-Rad, München
Mini-PROTEAN® 3 Cell	Bio-Rad, München
Multichannel Pipette RAININ (50-200 µl)	Eppendorf, Hamburg
MyCycler thermal cycler	Bio-Rad, München
Overhead shaker REAX2	Heidolph Instruments, Schwabach
pH-meter 761 Calimatic	Knick, Berlin
Pipette Boy Integra	Biosciences GmbH, Fernwald
Pipettes Research (2, 10, 20, 100, 200, 1000 µl)	Eppendorf, Hamburg
Plate Reader SPECTROstar Nano	BMG LABTECH Ortenberg
Power supply PowerPac™ HC/basic	Bio-Rad, München
Spectrophotometer NanoDrop® ND-1000	NanoDrop, USA
Thermal Cycler C1000™	Bio-Rad, München

Material

6.10 Cell lines

Table 2: Cell lines used in this study. All the received and generated cell lines used in this study are summarized below.

NOK	Normal oral keratinocytes immortalized by ectopic expression of TERT.	Gift from Dr. K. Münger
NOKs HPV38E6	Established from NOK parental cells. Expressing 3 × Flag-tagged HPV38E6	Established in this study.
NOKs HPV38E6-BirA*	Established from NOK parental cells. Expressing 3 × Flag-tagged HPV38E7 linked to BirA*	Established in this study.
NOKs HPV38E7	Established from NOK parental cells. Expressing 3 × Flag-tagged HPV38 E7	Established in this study.
NOKs HPV38E7-BirA*	Established from NOK parental cells. Expressing 3 × Flag-tagged HPV38E7 linked to BirA*	Established in this study.
NOKs HPV38E6E7	Established from NOK parental cells. Expressing 3 × Flag-tagged HPV38 E6 and StrepII-tagged HPV38E7	Established in this study.
HEK293T	Human embryonic kidney cells transformed with E1A/B of adenovirus 5, contains the SV40 T-antigen.	ATCC® CRL-3216™
MaFi132	Spontaneously immortalized <i>Mastomys</i> -derived fibroblasts	Established in this lab
MaFi132 MnPVE6-BirA*	Established from MaFi132 parental cells. Expressing 3 × Flag-tagged MnPVE6 linked to BirA*	Established in this study
MaFi132 MnPVE7-BirA*	Established from MaFi132 parental cells. Expressing 3 × Flag-tagged MnPVE7 linked to BirA*	Established in this study
MaFi132 GFP-BirA*	Established from MaFi132 parental cells. Expressing GFP linked to BirA*	Established in this study

MaFi191	Spontaneously immortalized <i>Mastomys</i> -derived fibroblasts	Established in this lab
308 Keratinocytes	Murine immortalized keratinocytes	[302]
308 MnPVE6	Established from 308 parental cells. Expressing 3 × Flag-tagged MnPVE6.	Established in this study
308 MnPVE7	Established from 308 parental cells. Expressing 3 × Flag-tagged MnPVE7.	Established in this study
308 MnPVE6E7	Established from 308 parental cells. Expressing 3 × Flag-tagged MnPVE6 and StrepII-tagged MnPVE7.	Established in this study

6.11 Bakteria

One Shot™ Stbl3™ Chemically Competent *E. coli*

Thermo Fisher Scientific, Darmstadt

One Shot™ TOP10 Chemically Competent *E. coli*

Invitrogen, Karlsruhe

Material

6.12 Oligonucleotides

All oligonucleotides (primers) were synthesized by Sigma-Aldrich, Germany.

Table 3: Primers used in this study. The sequences of all the primers used for PCR experiments in this study are listed below. Size: Sizes of the amplicons.

Primer name	Sequence	Used for	Annealing temperature and cycles
GAPDH-F	CTTCATTGACCTCAACTACATGGTC	PCR	58°C, 35x
GAPDH-R	GCAGTGATGGCATGGACTGTG	PCR	58°C, 35x
PtpN14(<i>Mastomys</i>)-F	gggatccccgggctgcaggaaATGCCTTTC GGCCTGAAGCT	Cloning pCMV_PtpN14 (Antibody-test)	62°C, 35x
PtpN14(<i>Mastomys</i>)-R	ttaaggtaccgggccccccTCAAATGAGCC TGGAGTTCTGCAG	Cloning pCMV_PtpN14 (Antibody-test)	62°C, 35x
Wwp2(<i>Mastomys</i>)-F	CGATAAAGCCCGGGCGGGATCAATGG CAGCTGCCAACTCCAGC	Cloning pCMV_Wwp2(A ntibody-test)	62°C, 35x
Wwp2(<i>Mastomys</i>)-R	CGATAAGCTTGATATCGAATTCTACTC CTGTCCGAACCCCTCAGTCTC	Cloning pCMV_Wwp2(A ntibody-test)	62°C, 35x
Cullin7(<i>Mastomys</i>)-F	CGATAAAGCCCGGGCGGGATCAATGG TGGGGGAGCTCCGCTACA	Cloning pCMV_ Cullin7(Antibod y-test)	62°C, 35x
Cullin7(<i>Mastomys</i>)-R	CGATAAGCTTGATATCGAATTCTACCG GAAAGTGGAGAAGGTCTGGG	Cloning pCMV_ Cullin7(Antibod y-test)	62°C, 35x
MnPVE6-F	GCCCCGGCGGATCCGCCgataggaccgt gcactccttgt	PCR	57°C, 35x
MnPVE6-R	atcagcgagctctaggaattACTAGTttacacg ggtttgcaaattctgcac	PCR	57°C, 35x
MnPVE7-F	CTGCAGGgccaccatggatgataggacctgac accacg	PCR	57°C, 35x
MnPVE7-R	CGCCGGCGacGCGGCCGagatcttcatt cttctggttacaccg	PCR	57°C, 35x
HPV38E6-F	cgataaaGCCCCGGCGGGATCaatggaac taccaaaacctcaaactgtg	PCR	57°C, 35x
HPV38E6-R	CTGCAGCCCGTAGTTTACTAGtcattctat tgcttgcaatgcctgc	PCR	57°C, 35x
HPV38E7-F	ttcaggtgtcgtgaCCTGCAGctagcggccacca tggatgattgggaaacaagctactcttc	PCR	57°C, 35x
HPV38E7-R	GGATCCGCCCGGGCGCCGGCGagatctt cgtccgccattg	PCR	57°C, 35x

BirA*-F	GCCCGGGCGGATCCGCCCATGAAGGA CAACACCGTGCC	PCR	57°C, 35x
BirA*-R	tctaggaattGCTAGCCTGCAGGttaCTTC TCGGCGCTCCGC	PCR	57°C, 35x
BirA*CloningMnE6-F	ACTGGCGGCCGCATGAAGGACAACAC CGTGCCCTGA	Cloning BirA*- MnE6 (BioID)	60°C, 35x
BirA* CloningMnE6-R	ATCGcgccggcgACTTCTCGGCGCTCCGC AGG	Cloning BirA*- MnE6 (BioID)	60°C, 35x
BirA*CloningMnE7-F	ATCGgcccgggcAATGAAGGACAACACC GTGCCCTGA	Cloning BirA*- MnE7 (BioID)	60°C, 35x
BirA* CloningMnE7-R	atcgGGATCCaCCTTCTCGGCGCTCCGC AGG	Cloning BirA*- MnE7 (BioID)	60°C, 35x
BirA*Cloning 38E6-F	CGCCGGCGCCCGGGCGGATCCATGAA GGACAACACCGTGC	Cloning BirA*- HPV38E6 (BioID)	60°C, 35x
BirA*Cloning 38E6-R	CATCCTTGTAATCTGCggccaaTGTACA CTTCTCGGCGCTCCG	Cloning BirA*- HPV38E6 (BioID)	60°C, 35x
BirA*Cloning 38E7-F	ATCGcgccggcgACTTCTCGGCGCTCCGC AGG	Cloning BirA*- HPV38E7 (BioID)	60°C, 35x
BirA*Cloning 38E7-R	ACTGGCGGCCGCaATGAAGGACAACA CCGTGCCCTGA	Cloning BirA*- HPV38E7 (BioID)	60°C, 35x

6.13 Plasmids

Table 4: Plasmids used in this study. All the received and generated plasmids used in this study are summarized below with their features and references indicated.

Plasmid name	Reference	Features
pCMV_VSV-G	Addgene #8454 [283]	Envelope protein for producing lentiviral particles.
pLenti_Neo/Kan	Gift from Dr. M. Niebler	
pLenti_MnPVE6	Constructed in this study.	MnPVE6 N-terminally fused to 3X-Flag-tag
pLenti_MnPVE7	Constructed in this study.	MnPVE6 C-terminally fused to 3X-Flag-tag
pLenti_MnPVE6E7	Constructed in this study.	MnPVE6 N-terminally fused to 3X-Flag-tag and C-terminally StreptII-tagged MnPVE7.
pLenti_MnPVE6-BirA*	Constructed in this study.	MnPVE6 N-terminally fused to Flag-tagged <i>BirA</i> *
pLenti_MnPVE7-BirA*	Constructed in this study.	MnPVE7 C-terminally fused to Flag-tagged <i>BirA</i> *
pCMV_3Tag-1A	Agilent Tech.	Cloning vector with CMV promoter

Material

		and enhancer, N-terminal 3 × Flag-tag
pPK_CMV-E3	PromoKine, Heidelberg	Empty cloning vector CMV promoter and enhancer C-terminal HA-tag
pCMV_PtpN14	Constructed in this study	<i>Mastomys</i> PtpN14 expression under CMV promoter, 3 × Flag-tag at N-terminus
pCMV_WWP2	Constructed in this study.	<i>Mastomys</i> Wwp2 expression under CMV promoter, 3 × Flag-tag at N-terminus
pCMV_Cullin7	Constructed in this study.	<i>Mastomys</i> Cullin7 expression under CMV promoter, 3 × Flag-tag at N-terminus
pWPI_Puro	Gift from Dr. M. Niebler	Lentiviral expression plasmid, confers puromycin resistance, puro gene located after an IRES
pWPI_38E6-BirA*	Established in this study.	HPV38E6 N-terminally fused to Flag-tagged BirA*
pWPI_38E7-BirA*	Established in this study.	HPV38E7 C-terminally fused to Flag-tagged BirA*
pLenti_GFP-BirA*	Established in this study.	GFP N-terminally fused to Flag-tagged BirA*
psPAX2	Gift from Dr. M. Niebler Addgene#12260	Second generation lentiviral packaging plasmid.

6.14 Antibodies

Table 5: Primary antibodies used in this study. All the antibodies used in this study are summarized below. Application information are provided as well.

Antibody	Distributor and catalogue number	Methods used in, working concentration
Anti-FLAG® M2, Mouse monoclonal	Sigma-Aldrich, Cat. # F3165, Lot: SLBT6752	Western Blot 1:1000 in 5% milk/TBST (w/v)
Anti-Biotin, HRP-linked	Cell Signaling Technology, Cat. #7075S Lot: 33	Western Blot 1:2000 in 5% BSA/TBST (w/v)
Anti-HA (3F10), Rat monoclonal	Roche, Cat. #11867423001	Western Blot 1:1000 in 5% milk/TBST (w/v)
Anti-GFP, rabbit polyclonal	Santa Cruz Cat.# sc-8334	Western Blot 1:1000 in 5% milk/TBST (w/v)
Anti-PtpN14	Cell Signaling Cat. # 13808	Western Blot 1:1000 in 5% milk/TBST (w/v)
Anti-Keratin 10	Covance PRB-159P	IHC: 1:1,000 (Citrate, 1h room temp.)
Anti-MnPVE4	Produced in this lab	IHC: 1:50 (Citrate, 1h room temp.)
Anti-Cullin7	ThermoFisher Scientific Cat. # PA5-22313	Western Blot 1:1000 in 5% milk/TBST (w/v)
Anti-WWP2	OriGene Cat. #TA329807	IF 1:200 in 1% goat serum/DPBS
Anti-YAP/TAZ	Cell Signaling Cat. # 14074	Western Blot 1:1000 in 5% milk/TBST (w/v) IF 1:200 in 1% goat serum/DPBS

Material

Table 6: Secondary antibodies used in this study. All the antibodies used in this study are summarized below.

Antibody	Distributor and catalogue number	Methods used in, working concentration
Goat-anti mouse IgG HRP Conjugate	Promega Cat. #: W402B	Western Blot 1:10000 in 5% milk/TBST (w/v)
Goat-anti rabbit IgG HRP Conjugate	Invitrogen Cat. #: W401B	Western Blot 1:10000 in 5% milk/TBST (w/v)
Goat-anti rat IgG (H+L) HRP Conjugate	Jackson Immuno Research Cat. #:112-035-143	Western Blot 1:5000 in 5% milk/TBST (w/v)
AlexaFluor594 Goat-anti rabbit IgG (H+L)	Invitrogen Cat. #: A11072	IF: 1:1000; 1h room temp. IHC: 1:1000, 1h room temp.
AlexaFluor488 Goat-anti rabbit IgG (H+L)	Invitrogen Cat. #: A11008	IF: 1:1000; 1h room temp. IHC: 1:1000, 1h room temp.
AlexaFluor488 Goat-anti mouse IgG (H+L)	Invitrogen Cat. #: A32723	IF: 1:1000, 1h room temp. IHC: 1:1000, 1h room temp.
AlexaFluor594 Goat-anti mouse IgG (H+L)	Invitrogen Cat. #: A11032	IF: 1:1000; 1h room temp. IHC: 1:1000, 1h room temp.
AlexaFluor594 Goat-anti mouse (IgG2b)	Invitrogen Cat. #: A21145	IF: 1:1000; 1h room temp. IHC: 1:1000, 1h room temp.
AlexaFluor594 Goat-anti mouse (IgG1)	Invitrogen Cat. #: A21125	IF: 1:1000; 1h room temp. IHC: 1:1000, 1h room temp.
AlexaFluor488 Goat-anti mouse (IgG1)	Invitrogen Cat. #: A21121	IF: 1:1000; 1h room temp. IHC: 1:1000, 1h room temp.

6.15 Software, programs and bioinformatic tools

Table 7: Software and programs used in this study.

Tool	Version	Source	Application
ImageJ	5.30.17 release	https://imagej.net/Fiji/Downloads	Image quantification
MaxQuant	v1.6.0.16	[303]	BioID data processing and protein identification
IPA	01-12	https://www.qiagenbioinformatics.com/products/ingenuity-pathway-analysis	Network analysis
SnapGene Viewer	5.2.4	https://www.snapgene.com/snapgene-viewer/	Cloning
Clustal Omega		https://www.ebi.ac.uk/Tools/msa/clustalo/	Cloning, Alignments
Serial Cloner	2.6.1	http://serialbasics.free.fr/Serial_Cloner.html	Cloning, Alignments
GIMP	2.10.22	https://www.gimp.org/	Image processing and quantification

7 Methods

7.1 Cultivation and treatment of cells

7.1.1 Cultivation of cell lines

NOK cells were cultured in Keratinocyte-SFM medium containing supplements provided by the manufacturer. HEK293T cells were grown in high-glucose (4.5 g/l) DMEM supplemented with 10% FBS, Penicillin-Streptomycin and L-Glutamine. MaFi132 and MaFi191 were cultured in low-Glucose DMEM supplemented with 10% FBS, Penicillin-Streptomycin and L-Glutamine. For 308 murine keratinocytes, a medium specifically for these cells was mixed in our laboratory (composition is listed in Table 1). All cells in culture were tested for *Mycoplasma spp.* contamination by PCR on a regular basis according to the protocol shown below. For this reaction, the Dream Taq polymerase was used. The products were visualized using agarose gel electrophoresis.

The sequence of interests was amplified in a thermo cycler using the following program:

Initial Denaturation	98°C	2 min	
Denaturation	98°C	30 sec	30 cycles
Annealing	X°C	20 sec	
Elongation	72°C	y sec	
Final Elongation	72°C	5 min	

All cell lines were maintained in an incubator set at 37°C with 5% CO₂ and 95% humidity.

7.1.2 Passaging and seeding of cells

For passaging cell lines, the medium was removed, and cell monolayer was washed with 1 x PBS once before treated with 1 ml 0.25% trypsin-EDTA. After incubating at 37°C for 5 minutes, 9 ml DMEM containing 10% FBS was added to neutralize the trypsin. Cell suspension was collected in a 15 ml tube and centrifuged at 1,400 rpm (revolutions per minute) for 2 minutes. The cell pellet was subsequently resuspended in 10 ml 1 x PBS, centrifuged at 1,400 rpm for 4 minutes again and resuspended in 5 ml fresh culture medium. This procedure was performed for all cell lines used within this thesis.

7.1.3 Counting of cells

For cell counting, 20 μ l cell suspension was mixed with 20 μ l of 0.25% trypan blue in 1 x PBS and the cell number was determined using a Neubauer counting chamber.

7.1.4 Cryopreservation and thawing of cells

For long-term storage of cell lines, cell pellets collected as previously described were directly resuspended in 1 ml cryo-medium and transferred into cryo-tubes. Tubes were stored directly in a Corning™ CoolCell™ cell freezing container at -80°C. For reactivation, cryo-tubes were placed in 37°C water bath until cells were thawed. Cells were then immediately resuspended in 9 ml of culture medium and seeded on dishes (MaFi132, MaFi192, 308 keratinocytes) or washed with 1 x PBS before resuspension in culture medium. 24 h after seeding the culture medium was refreshed.

7.1.5 Transient transfection

For transfecting cells with DNA plasmids, cells were seeded in either 6 cm/ 10 cm dishes in 4 ml/ 8 ml culture medium and incubated for 24 h. Before adding the transfection reagents, medium was changed to no FCS containing medium. PEI (polyethylenimine) solution (1 μ g/ μ l) was pre-warmed to room temperature for several minutes before adding it to DNA plasmids which were diluted in 400 μ l/ 800 μ l Opti-MEM. After PEI solution was added the tube was vortexed immediately for at least 30 sec. The DNA/PEI mixture was incubated at room temperature for 15 - 20 minutes and was then applied to the cells dropwise. The cell dish was gently shaken before placing it in the incubator. The cells were harvested 24 hours after transfection.

7.1.6 Lentivirus production and transduction of NOK cells, MaFi132 and 308 keratinocytes

For lentivirus production, 1×10^6 HEK293T cells were seeded in a 6 well plate. After 24 hours DMEM medium was removed and replaced by 1.5 ml Opti-MEM. 10 μ g of lentiviral expression plasmids, 5 μ g of packaging plasmid psPAX2, and 5 μ g of enveloping plasmid pMD2.G were mixed in Opti-MEM by mixing. 9 μ l clear PEI solution was added to the DNA/Opti-MEM mixture which was immediately vortexed. The transfection reagent was incubated at room temperature for 30 minutes and was applied to the cells dropwise. Cells were then cultured for 24 hours. Subsequently, the supernatant was removed and high-Glucose DMEM was applied to the cells. After 24 h the supernatant was collected using a 20 ml lock syringe and filtered through a Minisart-plus 0.45 μ m filter. The lentivirus-

Methods

containing supernatant was either used directly for transduction or stored in the -80°C freezer. For lentiviral transduction of NOK cells, MaFi132 or 308 keratinocytes, 750 μl of the abovementioned

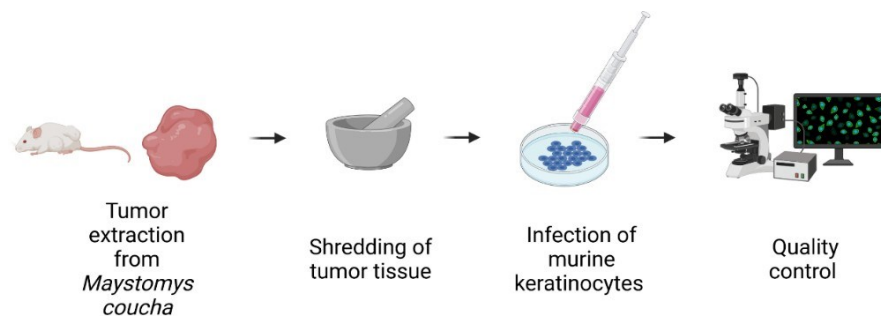


Figure 38: Schematic illustration of the infection process of 308 murine keratinocytes using MnPV-infected tumor tissue. Figure created with BioRender.com

supernatant was mixed with 750 μl of the cell corresponding medium and polybrene (10 $\mu\text{g}/\text{ml}$). The mixture was applied to 1×10^5 cells seeded in 6 well plate 24 hours prior to transduction. Cells were incubated for 24 hours before the virus-containing medium was removed from the cells and fresh medium was applied. After 3 days, medium containing the corresponding antibiotic (either G418 or Puromycin) was given onto the cells to start the selection. Untransduced cells were cultured in selection medium in parallel serving as a control. Antibiotic selection was considered as completed when all untransduced control cells were dead. Only cells within three passages after selection were used for experiments.

7.1.7 Verification of transduction

To check the presence of the transgene within the cellular genome and its transcriptional activity, RNA was extracted from the transduced cells and subsequently used in a PCR reaction to generate cDNA. Afterwards, 100 ng of the obtained cDNA was applied in a semi-quantitative PCR, using primers binding within the transgene sequences.

7.1.8 Generation of MnPV infected 308 keratinocytes

Infected murine 308 keratinocytes were generated by Dr. Rui Cao according to the following protocol.

MnPV particles were extracted from MnPV-induced skin lesions of *Mastomys coucha*. For this, frozen tumors were minced with a scalpel and placed in a 2 ml Precellys tubes containing 6 glass beads. 400 μl of pre-cooled 1 x DPBS containing 136.9 mM NaCl was added to the tubes. The mixture was then

homogenized twice using a Precellys 24 tissue homogenizer. If tumor tissue remained this step was repeated again. The tubes were centrifuged at 5,000 g for 10 min and the supernatant was collected. The homogenized mixture was transferred to a 50 ml Falcon tube filled with 5 ml 1 x DPBS. The mixture was then sonicated at an output of 3.0 (20-25%) for 50 sec, followed by centrifugation at 5,000 g for 10 min at 4°C. The supernatant was aliquoted into 1.5 ml Eppendorf tubes and stored at -20°C for further experiments. For the infection step, 1×10^5 308 cells were seeded into a 6-well plate 12 h before infection. Then, 100-150 μ l of the tumor extract was added to the culture medium followed by swirling the plate gently. After 24 h of incubation, the cells were washed 1 x DPBS twice and fresh culture medium was added for additional 24 h. Afterwards, the infected cells were cultured as described in 5.1.1. An overview of this entire procedure is shown in Figure 38.

To determine successful infection of the cells, they were checked for MnPVE4 expression using Western blot analysis (see point 5.2.2.) and IF (see point 5.2.3.) by Dr. Rui Cao.

7.2 Cloning and Analysis of Oligonucleotides

7.2.1 RNA Extraction from cells

For RNA extraction, the RNeasy Mini Kit (Qiagen) was used according to the manufacturer's protocol. As starting material, $3-5 \times 10^5$ cells were harvested using a cell scraper, washed once with 1 x DPBS and collected in 5 ml reaction tubes. RLT lysis buffer was supplemented with 40 μ l 1 M DTT per ml buffer and 600 μ l was added to the cells. Cells were lysed and homogenized by passing them through QIAshredder columns. 600 μ l of 70% ethanol (prepared with RNase-free water) was added to the mixture before proceeding according to the manufacturer's instructions. RNA was ultimately eluted in 35 μ l of RNase-free water. The concentration was determined photometrically. Subsequently, the co-extracted DNA was removed. To remove DNA traces, RNA was treated with Turbo-free DNase free kit. Briefly, 10 x RNase buffer and 0.6 μ l RNase were added to RNA (max 20 μ g) in 20 to 30 μ l. The mixture was incubated at 37°C for 30 minutes in a thermo mixer. To stop the reaction, the 0.1 volume of inactivation reagent was added to the mixture. The tube was incubated for 5 min and flicked several times to keep the inactivation beads in suspension. The beads and bound RNase were removed by centrifugation at 13,000 g for 2 min and transferring the DNase-free RNA to a new tube. Concentration was measured photometrically before use in reverse transcription or storage at -80°C.

Methods

7.2.2 Reverse transcription of RNA

DNA-free RNA was transcribed to cDNA by use of RevertAid Reverse transcriptase and oligo dT22 primers using the following protocol:

The reactions were set up in 0.5 ml reaction tubes. For detection of remaining DNA contaminations for each sample a RT- control reaction was set up in parallel.

	RT+ reaction	RT- reaction
RNA	150 ng – 1 µg	150 ng – 1 µg
Oligo-dT primer (20 µM)	1 µl	1 µl
ddH2O (RNase-free)	ad 12,5 µl	ad 13 µl

All reactions were incubated at 56°C for 5 min in to allow primer annealing to mRNAs. All reactions were chilled on ice for 1 min prior to addition of the following reagents.

	RT+ reaction	RT- reaction
5x RevertAid Buffer	4 µl	4 µl
dNTPs (10 mM)	2 µl	2 µl
RiboLock (20 U/µl)	0.5 µl	-
RevertAid Reverse Transcriptase (200 U/µl)	1 µl	-

All reactions were subsequently incubated for 1 h at 42°C and 10 min at 72°C.

The cDNAs, as well as the RT- controls, were used in different freshly prepared dilutions according to the purpose. Samples giving a signal in the respective RT- reaction were discarded. Samples negative in the RT-control reaction were further used.

7.2.3 Semi-quantitative polymerase chain reaction

Semi-quantitative polymerase chain reactions (RT-PCRs) were set up according to the following scheme:

Reagent	Volume
10x Green Buffer	2.5 μ l
dNTPs (2 mM)	2.5 μ l
Primer Mix (fw + rev, 20 μ M)	1.0 μ l
DreamTaq (5 U/ μ l)	0.15 μ l
cDNA (20-50 ng/ μ l)	1.0 μ l
ddH ₂ O (PCR grade)	ad 25 μ l

The following thermal cycling conditions were applied:

Initial Denaturation	95°C	3 min	z cycles
Denaturation	95°C	30 sec	
Annealing	x°C	30 sec	
Elongation	72°C	y sec	
Final Elongation	72°C	5 min	

6 x DNA Loading Dye was added to the reaction mixes. Amplified DNA fragments were separated by agarose gel electrophoresis in 1 % gels with 1 μ g/ml ethidium bromide added to the fluid gel. Amplified oligonucleotides were visualized at 260 nm in a documentation device. As size standard, GeneRuler 1 kb DNA ladder used.

7.3 Protein extraction

7.3.1 Protein extraction from cells

Culture medium was removed, and the cells were washed with 1 x PBS. Afterwards, the cells were harvested by scraping in ice-cold 1 x PBS and centrifuged at 8000 g for 2 min in 1.5 ml reaction tubes. According to the size of the cell pellets these were resuspended in 30-100 μ l of RIPA buffer supplemented with 1 x complete protease inhibitor cocktail and MG132 and were incubated for 30 min on ice. Afterwards the lysates were centrifuged at 13,000 g for 20 min (4°C) to clarify lysates from

Methods

solid, insoluble cell components. Supernatants were transferred to new 1.5 ml tubes and stored at -20°C until the protein content was quantified.

7.3.2 Nuclear/ cytosol protein extraction from cells

For the nuclear/cytosol protein extraction MaFi132 cells were seeded on 6 cm cell dish. After an incubation time of 24 h the medium was removed from the cells and the plates were washed with 1 x PBS twice. Cells were scraped off the plate and placed in a 15 ml reaction tube. After a 4 min centrifugation step (1400 rpm, 4°C) PBS was removed and the remaining cell pellet which was dissolved in 80 µl lysis buffer A. Next, cells were incubated for 1 h on ice before adding 5 µl 10% NP-40 to dissolve the cell membrane but not the nucleus membrane. After a centrifugation step (13,000 rpm, 4°C, 15 min) the supernatant containing the cytosolic proteins was removed and given into a fresh reaction tube. 10 µl of lysis buffer B was given directly to the remaining pellet containing the nuclear proteins. This mixture was incubated for 30 min on ice and vortexed every 5 min. After the incubation step, the lysates were centrifuged for 5 min (13,000 rpm, 4°C). The supernatant containing the nuclear proteins was given into a fresh reaction tube. 17 µl of 1 x Laemmli buffer was given to the cytosolic fractions and 2 µl of this loading dye to each nuclear fraction before boiling the samples for 10 min at 99°C. Lysates were analyzed afterwards using immunoblotting (see chapter 5.5.2.).

7.3.3 Protein extraction from FFPE Tissue

Tissue dissection from FFPE tissue was performed manually using a cannula. The use of a microscope during this process allowed precise extraction of the tissue from slides. Figure 39 shows an illustration of the removal procedure.

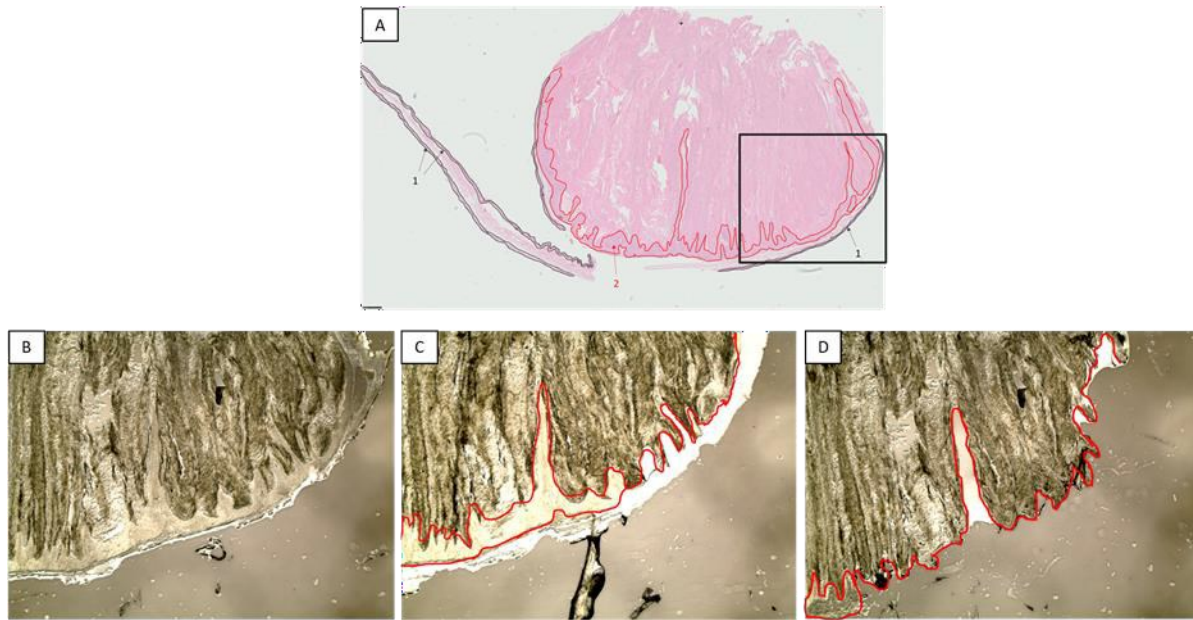


Figure 39: Illustration of the dissecting process of the tissue material from *Mastomys coucha* for the subsequent proteomic analysis. A) HE staining of a *Mastomys coucha* tumor section. Different areas that are to be extracted were outlined in black and red. Areas outlined in red show well-differentiated tumor tissue, control skin areas are outlined in black. The black box symbolizes the area magnified in panel B) – D) showing unstained tumor section. It can be seen in these panels that the dissection method using a cannula allows precise extraction of certain predefined areas within a tumor.

Tissue removed from a slide was transferred directly into 25 μ l of FFPE-RIPA lysis buffer. A new cannula was used for each sample to exclude possible contamination. Subsequently, samples were incubated at 99°C for 20 min. After this heating phase, samples were incubated at 60°C for 2 h, while mixing every 30 min for 5 sec followed by centrifugation at 1,000 g.

After this second incubation phase, the lysates were centrifuged at 4°C for 10 min at 15,000 g. The supernatant was transferred to a new tube. Low protein binding tubes were used throughout the procedure to guarantee highest possible protein concentration. The prepared lysates were handed over to Dr. Torsten Müller for further processing SP3 method. The procedure of protein purification

Methods

using this method is explained in more detail in chapter 5.7.2. To illustrate the entire process of extracting proteins from FFPE material, a schematic overview is shown in Figure 40.

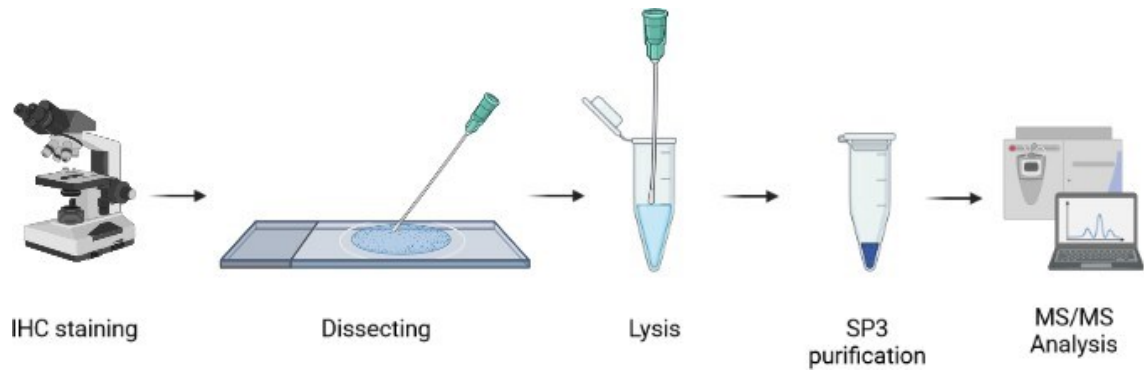


Figure 40: Schematic overview of partial-proteomics workflow. Created with BioRender.com

7.4 Quantification of protein concentration by Bradford assay

Total protein concentrations of cell lysates were determined *via* Bradford Assay. 5 μl of diluted cell lysates were added to 160 μl water in a 96-well plate. 40 μl /well of 5x Bradford Assay Reagent were added and mixed by pipetting. Potential bubbles were removed using a cannula. Standard curve was generated by serial dilutions of BSA (stock: 20 mg/ml) and measured in parallel with the samples.

Pipetting scheme of BSA standards is given in Table 8.

Table 8: Pipetting scheme of BSA standards. Protein concentrations were determined between 0 mg/ml to 7.5 mg/ml. For the measurement, BSA standards as well as samples were diluted 1:10 in ddH₂O.

desired concentration	PBS	BSA (from)
7.50 mg/ml	50 μ l	30 μ l (stock)
5.00 mg/ml	30 μ l	60 μ l (1)
2.50 mg/ml	30 μ l	30 μ l (2)
1.00 mg/ml	60 μ l	40 μ l (3)
0.75 mg/ml	25 μ l	75 μ l (4)
0.50 mg/ml	30 μ l	60 μ l (5)
0.25 mg/ml	30 μ l	30 μ l (6)
0.00 mg/ml	100 μ l	0 μ l

All samples and standards were tested in duplicates. The absorption of standards and protein samples was determined photometrically at 595 nm in a SPECTROstar Nano plate reader after 5 min of incubation. Concentrations of samples were validated according to the standard calibration curve.

7.5 Protein separation and visualization

7.5.1 SDS- PAGE

Proteins were separated *via* discontinuous SDS-polyacrylamide gel electrophoresis (discontinuous SDS-PAGE). Due to the denaturing conditions in the gel and the binding of negatively charged SDS molecules to the peptides a separation by size is achieved in the electrophoresis. Depending on the size of the target proteins, resolving gels of different bisacrylamide concentrations were used whereas the stacking gel was prepared with 5% bisacrylamide always. Quantified cell lysates were supplemented with 5x SDS loading dye and incubated for 5 min at 99°C. 50-100 μ g of total protein sample were applied to the gel together with PageRuler Prestained Protein Ladder. 80 V were applied

Methods

for 20 min until the sample entered the resolving gel. The voltage was increased afterwards to 120 V until a suitable separation was reached.

7.5.2 Western Blot

Separated proteins were electrophoretically transferred to a PVDF membrane in Mini Trans-Blot® Cell. Prior to transfer, the PVDF membrane was incubated in methanol for 2-5 min and then equilibrated in 1 × Towbin transfer buffer. The blotting cassette assembly using “sandwich” method [304]. For blotting, 0.4 A was applied to Mini Trans-Blot® Cell for 60 minutes and the cell was placed in 4°C room during the transfer. After blotting, the PVDF membranes were blocked with either 5% milk in 1 × TBST or with 5% BSA in 1 × TBST at room temperature for 45-60 min. The membranes were then incubated in primary antibodies with agitation at 4°C for overnight. The next day, the membrane was washed three times with 1 × TBST (10 minutes each) and incubated with the secondary antibody conjugated with horseradish peroxidase (HRP) for 1 hour at room temperature, followed by three times washing. Finally, the bound antibodies were visualized by an HRP-catalyzed enhanced chemiluminescent reaction (ECL) through exposure to X-ray films.

7.5.3 Immunofluorescence (IF)

Cells were seeded on glass slides and let grown on at 37°C. After cells attachment, the medium was removed and cells were washed twice with cold (4°C) 1x PBS. 4% formalin was added onto the cells to fix them onto glass slides. To permeabilize the cells, 0.5% Triton X-100 in 1x PBS was added onto cells and incubated at 4°C for 5 min. Afterwards fixed cells were washed again twice using PBS by dipping the glass slides into the prepared solution. To prevent unspecific binding, cells were blocked with 10 % goat serum in 1x PBS for 1 h at RT. Cells were washed after 1 h of incubation again by dipping glass slides into PBS twice before primary antibodies were added. All antibodies used in this thesis for Immunofluorescence were diluted in 5 % FCS/0.5 % Triton X-100 in 1x PBS. Primary antibodies were incubated over night at 4°C. Secondary antibodies were added after dipping glass slides into PBS five times and incubated at RT for 1 h. DAPI staining was performed after three more wash steps in PBS. Cells were mounted and signals were visualized using Keyence BZ-9000 Microscope.

7.5.4 Immunohistochemistry (IHC)

For immunohistochemical analyses, serial sections of 3 μm thickness of formalin-fixed, paraffin-embedded (FFPE) skin tumors of *Mastomys coucha* were rehydrated with xylene and a series of graded alcohols according to the following procedure.

solvent	duration
Xylol (100%)	10 min
Ethanol (100%)	10 min
Ethanol (90%)	5 min
Ethanol (70%)	5 min
1x PBS	5 min

After rehydration, heat-induced antigen retrieval was performed by boiling the sections for 10 min in citrate buffer (pH= 6.0) or Tris-EDTA (pH= 9.0) in a steam pot. The slides were cooled in the antigen retrieval solution for 10 minutes and then incubated for 10 min in 1x PBS. Endogenous peroxidases were blocked with Dako REAL peroxidase blocking solution for 10 minutes at room. Non-specific protein binding sites were blocked by incubating the slides for 45 minutes with 10% goat serum diluted in 1x PBS. After the blocking procedure the sections were incubated overnight at 4°C with primary antibodies diluted in 1x PBS with 1% goat serum. The next day, sections were washed thoroughly in 0.1% PBS-T. Expression was visualized using secondary antibodies mentioned in 5.7.2. Nuclei were counterstained with 0.3 $\mu\text{g}/\text{ml}$ in 1x PBS 4',6-diamidino-2-phenylindole (DAPI). The sections were mounted with Dako Faramount Aqueous Mounting Medium and covered with cover slides. Analysis of IHCs was done by light microscopy (Keyence BZ-9000 Microscope) at magnification up to 200X.

Methods

7.6 Protein-protein interaction studies

7.6.1 BioID

MaFi132 BirA*-GFP, MaFi132 MnPVE6-BirA*, MaFi132 MnPVE7-BirA* as well as NOK BirA*-GFP, NOKs 38E6-BirA* and NOKs 38E7-BirA* were seeded in 10 cm dishes. MaFi132 were seeded in DMEM supplemented with 10% FBS, L-Glutamine and Pen/Strep while NOK cells were seeded in K-SFM medium. 24 hours after seeding, the culture medium was refreshed with corresponding medium supplemented 50 μ M biotin. 18 hours later cells were harvested. After briefly washing the cells with 1x PBS, 1 mL of modified RIPA buffer was added to the cell monolayer in the dishes and collected in 15 ml tubes with a cell scraper. Lysates were incubated on a rotator at 4°C for 1 h. The lysates were centrifuged at 13,000 rpm at 4°C for 30 minutes to remove cell debris. The supernatants were collected for pull-down experiment. All lysates were prepared in triplicates.

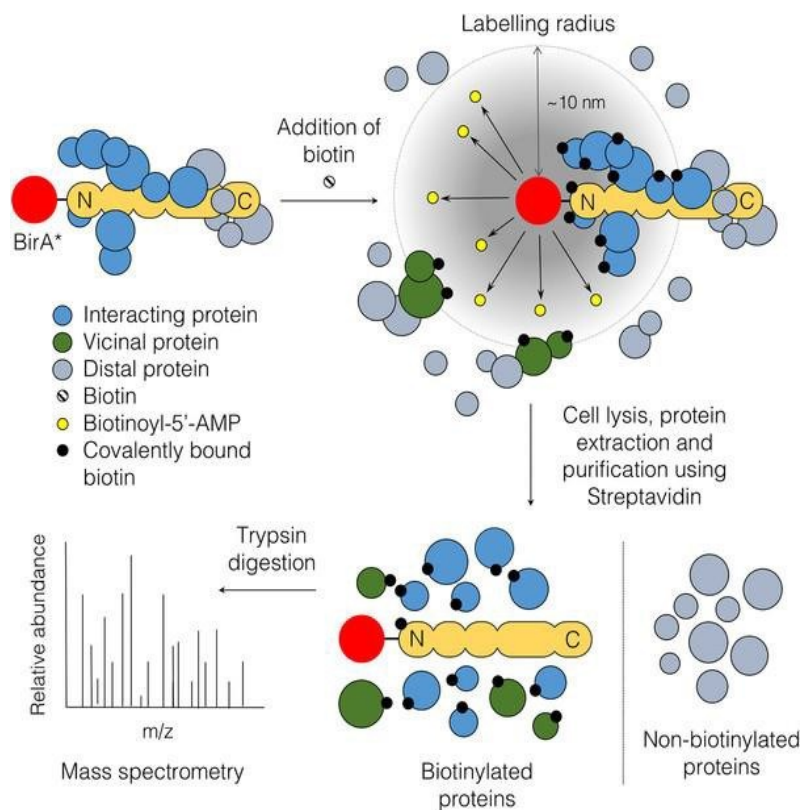


Figure 41: Interactome studies via BioID. Schematic overview of the BioID screening method which allows to identify protein interactions (Figure modified from [8]). BioID fusion protein induces proximal protein biotinylation. Purification of labeled proteins was done by streptavidin pull-down. Isolated proteins were identified by mass spectrometric analysis.

7.6.2 Immunoprecipitation (IP)

MaFi132 cells were lysed for 2 h at 4°C on a rotator in 200 µl RIPA-special lysis buffer for immunoprecipitation assay. Afterwards the protein mixture was centrifuged for 10 min at 4°C and 13,000 rpm. 20 µl of each sample were taken as input sample and supplemented with 4 µl of 5x Laemmli buffer. Residual protein mixture was given onto previously blocked anti-FlagM2 agarose beads. For each sample 30 µl beads suspension was blocked in 5% BSA in 1x PBS for 1 h at 4°C on a rotator and afterwards washed 3 times with 1x PBS. For each wash step, 500 µl PBS was added to the beads and incubated for 5 min at a rotator before a 1 min centrifugation step at 3,000 rpm. After the washing the 180 µl lysate was added to the beads. The bead-lysate incubation step was performed at 4°C on a rotator overnight.

The next day the beads were washed three times with RIPA lysis buffer and bound proteins were eluted in 1x Laemmli buffer using a 10 min boiling step at 99°C. In addition, the previously prepared input samples were boiled together with the IP-samples to prepare them for further analysis by either WB (5.5.2.) or MS (5.7.3.).

7.7 Protein purification

7.7.1 Streptavidin Pull down

Previously described protocols [165, 305] were used to pull down biotinylated proteins. 50 µl of streptavidin coupled beads were mixed with 300 µl of modified RIPA buffer in a 1.5 ml reaction tube. The bead suspension was mixed at room temperature on a rotor for 5 min. After equilibration, the beads were spun down at 2,000 rpm for 2 min and supernatant was removed afterwards. Lysates prepared as described in 5.3.1. were incubated with the equilibrated beads using a rotator at 4°C, overnight. The next day, beads were spun down again with a centrifugation step at 2,000 rpm for 2 min. The supernatant was removed and beads were washed with 500 µl of modified RIPA buffer at room temperature on a rotator for 10 min. Beads were collected by centrifugation at 2,000 rpm for 2 min. The beads were washed five times with 50 mM ammonium bicarbonate (pH= 8.3) buffer. After the last wash step, beads were mixed with 35 µl 1x Laemmli buffer and boiled at 99 °C for 10 minutes. Samples were frozen at -20°C until sent for mass spectrometry analysis.

Methods

7.7.2 Protein purification using SP3-method

SP3 method was performed by Dr. Torsten Müller according to the following protocol.

Samples were thawed, vortexed, and subsequently transferred to AFA-TUBE TPX PCR stripes (Covaris, Inc.) for adaptive focused acoustics (AFA) ultrasonication in a LE220plus Covaris device. Here, the peak incidence power (PIP) was set to 450, the duty factor (DF) to 50%, the cycles per burst (CPB) to 600, and the time to 300 seconds per TPX PCR stripe. Dithering of the AFA focus was applied with a 3 mm z-offset. Samples were centrifuged at 15,000 g for 10 minutes before proceeding with a protein quantification assay (Pierce, Thermo Fisher Scientific). For each sample, 10 µg of extracted protein was transferred to a 96-well PCR plate for processing with autoSP3 on an Agilent Bravo liquid handling system. In brief, the plate was prepared with each sample in a total volume of 12 µL 1% SDS, 100 mM ammonium bicarbonate (ABC). Proteins were automatically reduced and alkylated by addition of 10 mM tris(2-carboxyethyl)phosphine (TCEP), 40 mM chloroacetamide (CAA), 1x protease inhibitor cocktail (PIC) in 100 mM ABC and incubation for 5 minutes at 95°C. Subsequently, proteins were immobilized on paramagnetic, carboxylate-modified SP3 beads by establishing a >50% organic environment with acetonitrile (ACN). The bead:protein conjugates were extensively washed twice with 200 µL 80% Ethanol and once with 100% ACN. The digestion of proteins was performed using trypsin at a 1:60 protease to protein ratio for 16 hours in 100 mM ABC. Upon overnight digestion, the reaction was quenched by acidification to 0.5% trifluoro acetic acid (TFA). The peptide-containing supernatant was recovered to a new 96-well plate without the transfer of residual beads. MS injection-ready samples were stored at -20°C until data acquisition.

7.7.3 Peptide analysis using mass spectrometry analysis

Protein samples were separated in SDS-PAGE. Gel pieces were cut out, cysteines were reduced by DTT and carbamidomethylated using iodoacetamide followed by 4 h trypsin digestion. Resulting peptides were loaded on a cartridge trap column, packed with Acclaim PepMap300 C18, 5µm, 300Å wide pore (Thermo Scientific) and separated *via* a gradient from 3% to 40% ACN on a nanoEase MZ Peptide analytical column (300 Å, 1.7 µm, 75 µm x 200 mm, Waters) using a 120 min MS-method. Eluted peptides were analyzed by an online coupled Orbitrap Exploris 480 mass spectrometer. Data analysis was carried out by MaxQuant (version 1.6.14.0). Two data sets were created. One is intensity based absolute quantification (iBAQ) in which all identified peptide intensities is summarized to measure protein abundance and the other hand label free quantification (LFQ) data, which is the simplest form

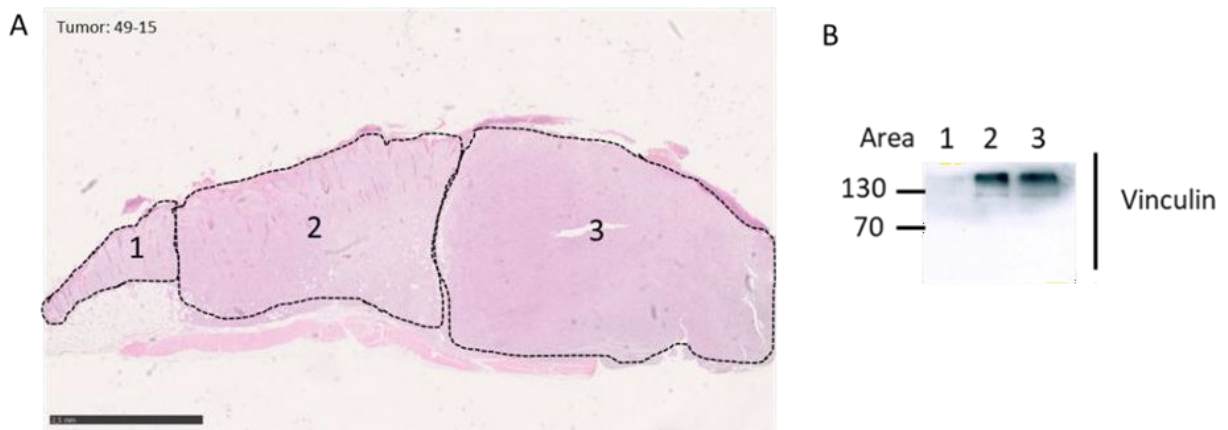
of quantitative proteomics, in which different samples are quantified in separate MS runs. Match between runs option was enabled to transfer peptide identifications across raw files based on accurate retention time and m/z. Quantification was done using a label free quantification (LFQ) approach based on the MaxLFQ algorithm [135]. A minimum number of quantified peptides were required for protein quantification.

7.8 Visualization of MnPV DNA by *in-situ* hybridization (ISH)

FFPE tissue section (3 μm thickness) were incubated on at 56°C to enable a gently rehydration the next day. For this, the same xylene and a series of graded alcohols was used as for IHC stainings (see 5.5.4.). After rehydration, the slides were boiled in citrate buffer (pH= 6.0) in a steam pot as described for IHC. Meanwhile, protease K (2 $\mu\text{g}/\text{ml}$ in 50 ml 0.05 M Tris/HCl, pH= 7.5) was heated up to 37°C. After the washing step, slides were dried at RT. FixoGum was used to skirt the tissue and enable a precise apply of blocking and hybridization solutions. After FixoGum was dried Protease K digestion was performed at 37°C for 12 min and stopped after 12 min using 50 mM glycine in 1x TBS. Endogenous peroxidases were blocked with 3% H_2O_2 in TBS for 10 min at RT and rinsed for 30 sec with TBS at RT as well. Sections were dried at RT for 5 min until no visible liquid was left. Meanwhile, the (pre)hybridization mixture was prepared. The mixture was split in half one of those was used as pre-hybridization mixture, the other one as hybridization mixture. Before giving pre-hybridization mixture onto slides, the mix was incubated at 98°C for 2 min. After 3 h of incubation time at RT hybridization mixture was given onto slides. Hybridization mixture was prepared by addition 300 ng/ml probe DNA. The hybridization mixture was given onto the slides and incubated for 5 min on heat plate (98°C) before covering with a coverslip to avoid evaporation of the hybridization mix. The slides were then incubated over night at 42°C in wet chamber. 2x SSC was preheated on at 42°C as well and used as first wash solution the next day. Hybridization mixture was washed off the slides using the pre heated 2x SSC in glass chamber with magnetic stirrer (10 min, RT). Afterwards, the slides were subsequently washed with 1x SSC and 0.5x SSC (each for 10 min at RT) followed by two washing steps with TBS (RT, 3 min). Thereafter, sections were blocked using 20% goat serum (GS) in TBS/TNB buffer. Goat serum was diluted in TBS/TNB buffer (1:3). After 45 min incubation time at RT in wet chamber the blocking mixture was removed. Then, the slides were incubated for 30 min at RT with HRP-SAP (from TSA-Kit) diluted 1:250 in 10% GS in TBS/TNB buffer. Afterwards slides were washed three times using TBS (3 min, RT). To gain best results, signal enhancer biotinyltyramide was used which was attenuated in

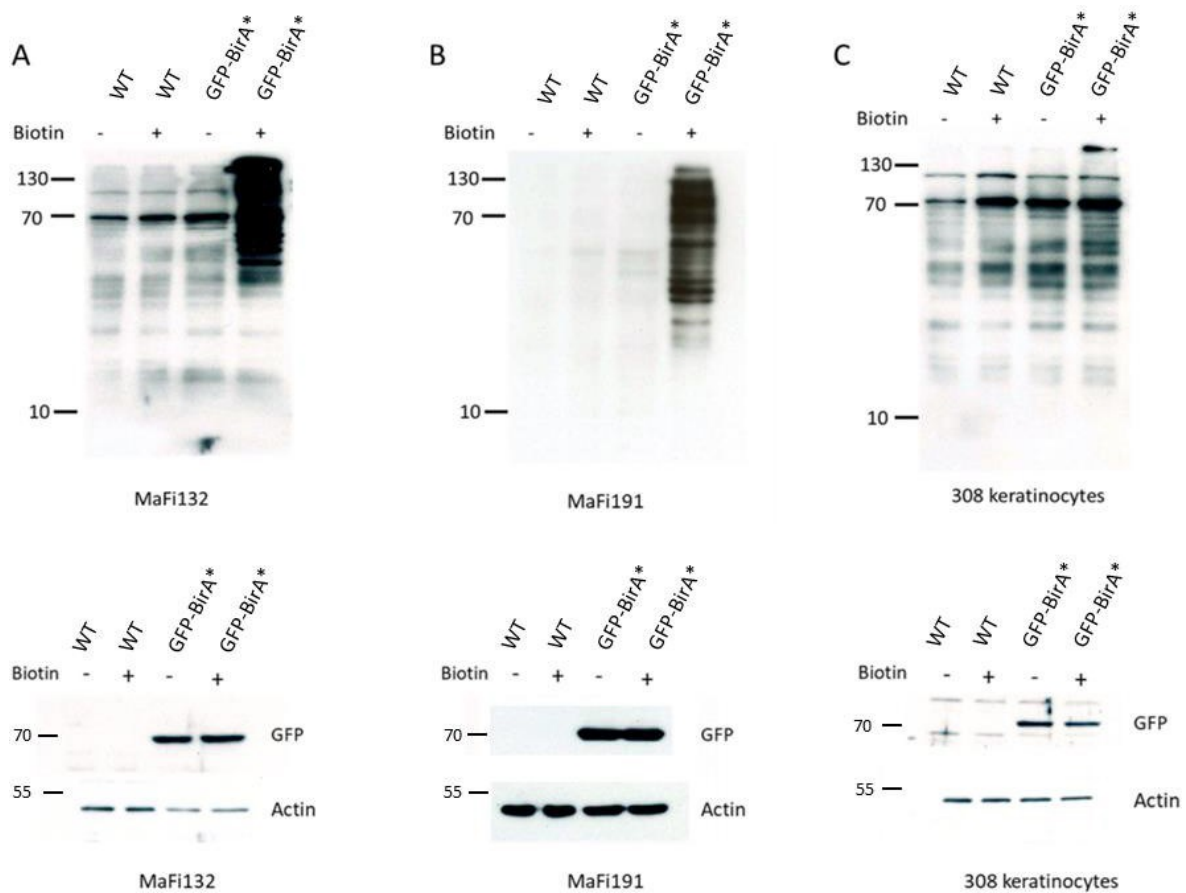
Methods

amplification diluent according to instructions in TSA- Kit. After three wash steps (TBS, RT, 3 min each step) slides were again incubated with HRP-SAP diluted 1:250 in GS/ TBS/TNB buffer mixture for 30 min at RT. Three more washing steps followed (TBS, RT, three min each). Staining was performed using AEC substrate under permanent observation. The color reaction was stopped with ddH₂O. Counterstain was performed using undiluted haematoxylin. The sections were mounted with Dako Faramount Aqueous Mounting Medium and covered with cover slides. The imaging was performed using a Keyence BZ-9000 Microscope.



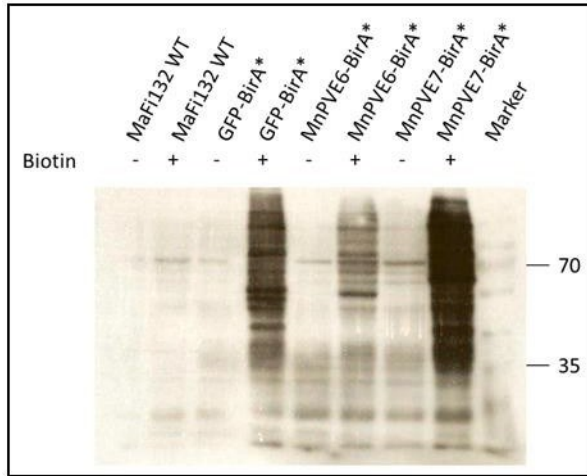
Supplemental Figure 1: Examination of smallest volume usable for lysis and further proteomic analyses. A) Subdivision of a tumor into three areas of different sizes. Scale bar: 2.5 mm. **B)** Dissected material of each area was lysed and analyzed via western blot to investigate the usage in further mass-spectrometric analyses. Area 1: 2.548 mm² (0.03 mm³); Area 2: 11.276 mm² (0.135 mm³); Area 3: 16.706 mm² (0.2 mm³)

8 Supplemental Figures

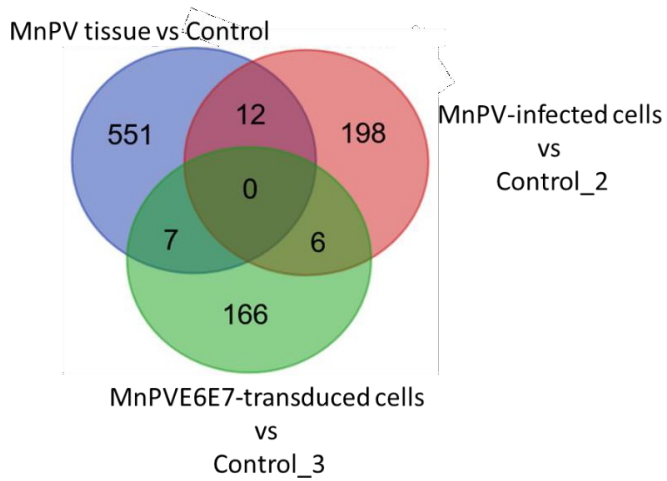


Supplemental Figure 2: Biotinylation assays to determine the cell line to be used for BioID experiments on MnPV oncoproteins. **A)** Biotinylation assay for MaFi132. Cells were transiently transfected with pLenti_GFP-BirA*. After 24 h, biotin-rich medium was added to the cells and 24 h later cells were lysed. 50 μ g of total cell lysate was applied per lane and then tested for successful biotinylation in WB against biotin. The same procedure was done for **B)** MaFi191 and **C)** 308 keratinocytes. WB against GFP served as transfection controls. Actin was used as a loading control. The best biotinylation could be achieved with MaFi132. This cell line was used for subsequent BioID experiments for MnPVE6 and E7.

Supplemental Figures



Supplemental Figure 3: Western blot analysis using anti-biotin antibody to detect protein biotinylation levels in cells after the addition of biotin. Fusion protein-expressing MaFi132 and WT control cells were treated with biotin, lysed and lysates were used in WB against biotin. MnPVE6-BirA* shows weak biotinylation compared to MnPVE7-BirA* or GFP-BirA* control.



Supplemental Figure 4: Venn diagram depicting a comparison of differentially expressed proteins found in in vivo proteomic results compared to in vitro proteomic results.

9 Supplemental Tables

Supplemental Table 1: Results of partial proteomics; iBAQ values. Red indicates upregulation, blue shows downregulation. **A)** MnPV-positive tissue vs skin **B)** Well-differentiated tissue vs skin **C)** Dedifferentiated tissue vs skin **D)** MnPV-positive tissue vs well-differentiated **E)** MnPV-positive tissue vs dedifferentiated **F)** Dedifferentiated tissue vs well-differentiated. For simplicity, only the top 5 up-regulated hits and top 5 down-regulated hits are shown. Red indicates upregulation, blue shows downregulation.

A

MnPV-positive tissue vs skin		
Gene names	Log2FC	p-value
MnPVE1_E4	9,96	<0.05
Brcc3	8,92	<0.05
MnPVE2	8,32	<0.05
Mcm6	6,92	<0.05
Pus7	6,7	<0.05
Acot7	-3,67	<0.05
Scarb2	-3,76	<0.05
Ephx1	-3,78	<0.05
Krt81	-4,02	<0.05
Hmgcs2	-5,86	<0.05

B

Well-differentiated tissue vs skin		
Gene names	Log2FC	p-value
Hba	8,57	<0.05
Fga	5,93	<0.05
C4b	5,1	<0.05
Ttr	4,94	<0.05
Txnrd1	4,29	<0.05
Bbox1	-3,81	<0.05
Ephx1	-3,83	<0.05
Krt33a	-4	<0.005
Aldh3a2	-4,82	<0.05
Hmgcs2	-5,63	<0.05

C

Dedifferentiated tissue vs skin		
Gene names	Log2FC	p-value
Acp2	4,8	<0,05
Park7	4,7	<0,05
Fkbp1a	4,59	<0,05
Gns	4,48	<0,05
Siglec1	4,32	<0,05
Hmgcs2	-5,78	<0,05
Krt1	-5,87	<0,05
Casp14	-6,15	<0,05
Krt10	-6,41	<0,05
Rik	-9,08	<0,05

D

MnPV-positive tissue vs well-differentiated		
Gene names	Log2FC	p-value
MnPVL1	10,6	<0.05
MnPVE1_E4	9,53	<0.05
MnPVE2	9,29	<0.05
Sumo3	6,01	<0.05
Krt73	5,77	<0.0005
Ak3	-2,42	<0.05
Cpm	-2,54	<0.05
Ca2	-2,59	<0.005
Map2k4	-2,75	<0.05
Try10	-3,56	<0.05

E

MnPV-positive tissue vs dedifferentiated		
Gene names	Log2FC	p-value
MnPVE1_E4	10,28	<0.05
MnPVL1	9,98	<0.05
MnPVE2	9,02	<0.05
Krt2	7,85	<0.05
Casp14	6,46	<0.05
Plekho2	-4,05	<0.05
Dclk1	-4,11	<0.05
Hm13;H13	-4,25	<0.05
Bak1	-4,56	<0.05
Crabp1	-4,73	<0.05

F

Dedifferentiated tissue vs well-differentiated		
Gene names	Log2FC	p-value
Gda	3,79	<0.05
Clic4	3,77	<0.05
Siglec1	3,65	<0.05
Atp2b1	3,2	<0.05
Gmppa	3,17	<0.05
S100a14	-5	<0.05
Tgm1	-5,33	<0.05
Pkp3	-5,36	<0.05
Trim29	-5,52	<0.05
Krt2	-6,3	<0.05

Supplemental Table 2: Results of proteomics performed on infected 308 keratinocytes (iBAQ values). Red indicates upregulation, blue shows downregulation. For simplicity, only the top 5 up-regulated hits and top 5 down-regulated hits are shown.

MnPV-infected vs control		
Gene names	Log2FC	p-value
Ddx19b	5.28	<0.05
Gramd4	4.56	<0.05
Nat9	2.91	<0.05
Adar	2.81	<0.05
Dock11	2.47	<0.05
Dhrs4	-2.81	<0.005
Stfa3	-2.98	<0.05
Pea15	-3.43	<0.05
Sde2	-3.80	<0.05
Fkbp5	-4.67	<0.05
Pdzrn3	-6.52	<0.05

Supplemental Table 3: Proteomic results of transduced 308 keratinocytes expressing MnPV oncoproteins (iBAQ values). A) MnPVE6 vs control B) MnPVE7 vs control C) MnPVE6E7 vs control. Red indicates upregulation, blue shows downregulation when compared to control. For simplicity, only the top 5 up-regulated hits and top 5 down-regulated hits are shown.

MnPVE6 vs control			MnPVE7 vs control			MnPVE6E7 vs control		
Gene names	Log2FC	p-value	Gene names	Log2FC	p-value	Gene names	Log2FC	p-value
Mau2	3.65	<0.005	Ppfibp2	4.80	<0.05	Igfbp3	5.74	<0.05
Pdcd11	3.38	<0.05	Serpinb2	4.08	<0.05	Fat2	4.34	<0.05
Smn1	2.96	<0.05	Kdelr2	3.90	<0.05	Col12a1	3.01	<0.05
Glyr1	2.87	<0.005	Slc20a2	3.66	<0.05	Jag1	2.90	<0.05
Lrrc8d	2.67	<0.05	Itga2	3.53	<0.05	Hmces	2.63	<0.05
Bst1	-4.50	<0.005	Smn1	-2.82	<0.05	Akr1c18	-3.38	<0.005
Kdelr2	-4.62	<0.05	Gan	-2.86	<0.05	Wdr35	-3.70	<0.05
Mtch1	-4.98	<0.05	Cars2	-2.90	<0.05	Cox6a1	-4.02	<0.005
Ppfibp2	-5.42	<0.005	Mrpl13	-3.21	<0.05	Kdelr2	-4.21	<0.05
Ccna2	-6.03	<0.05	Tdp1	-3.44	<0.005	Atpaf2	-4.90	<0.005

Supplemental Table 4: Proteomic results of HPV38 oncoprotein-expressing NOK cells (iBAQ values).

A) HPV38E6 vs control B) HPV38E7 vs control C) HPV38E6E7 vs control. Red indicates upregulation, blue shows downregulation when compared to control. For simplicity, only the top 5 up-regulated hits and top 5 down-regulated hits are shown. For HPV38E6E7 expressing cells, CUL7 expression value is given additionally.

A

HPV38E6 vs control		
Gene names	Log2FC	p-value
CHPF	8,37	<0.05
ATOX1	7,69	<0.05
STMN2	7,30	<0.05
C7orf50	6,97	<0.05
FECH	6,54	<0.05
CARS	-5,82	<0.05
PRSS1	-6,11	<0.05
LSM2	-6,19	<0.05
MYCBP	-6,22	<0.05
HERPUD1	-7,45	<0.05

B

HPV38E7 vs control		
Gene names	Log2FC	p-value
STMN2	8,12	<0.05
ACTBL2	7,98	<0.05
ATOX1	7,03	<0.05
MIOS	6,87	<0.05
C7orf50	6,70	<0.0005
S100A9	-6,60	<0.0005
HERPUD1	-7,12	<0.05
METTL14	-7,17	<0.05
MTRR	-7,19	<0.05
S100A8	-7,98	<0.05

C

HPV38E6E7 vs control		
Gene names	Log2FC	p-value
CAP1	8,64	<0.05
STMN2	7,68	<0.05
GYG1	6,91	<0.05
OR4K3	6,71	<0.05
H1FO	6,37	<0.05
TOMM20	-6,99	<0.05
METTL14	-7,25	<0.0005
TOMM22	-7,67	<0.05
TOMM40	-7,70	<0.05
SLC33A1	-8,51	<0.05
CUL7	-1,51	<0.05

Supplemental Table 5: Gene names of proteins found to be significantly altered in MnPV as well as in HPV38 oncoprotein- expressing cells.

Altered proteins in E6-expressing cells	Altered proteins in E7-expressing cells	Altered proteins in E6E7-expressing cells
Cobll1	Cyth2	Akap1
Commd8	Ecm1	Apaf1
Ctnna2	Gan	Cdc20
Cttnbp2nl	Gcc2	Cox5a
Ecm1	Med14	Cul7
Numa1	Mki67	Cux1
Rbm27	Mrpl13	Dyrk1a
Smn1	Nop14	Ecm1
Snx18	Pdcl	Fat2
Tacc2	Ptpn13	Gba
Tdp1	Smn1	H1f0
	Tdp1	Jag1
		Mrpl14
		Ncbp2
		R3hcc1l
		Rpf2
		Sgk3
		Slc4a2
		Tomm22
		Trmt112
		Ube2j1
		Uxs1

10 List of Figures

Figure	Title
Figure 1	The diversity of human papillomaviruses
Figure 2	Schematic genome organization of HPVs and MnPV.
Figure 3	Protein expression map of high-risk mucosal HPVs.
Figure 4	The two HPV oncoproteins E6 and E7.
Figure 5	Risk factors for cutaneous squamous cell carcinoma (SCC).
Figure 6	The preclinical animal model <i>Mastomys coucha</i> .
Figure 7	<i>Schematic overview of the experiments and methods performed within this thesis.</i>
Figure 8	IF staining of a MnPV-positive <i>Mastomys</i> skin tumor.
Figure 9	Exemplary HE stained nKSCC tumor to visualize the subdivision of micro-dissected areas.
Figure 10	The analysis of the <i>in vivo</i> proteome results shows a successful application of the new method.
Figure 11	Volcano blots show overview of comparison between different <i>in vivo</i> proteomes.
Figure 12	Top 15 altered canonical pathways identified by IPA in <i>in vivo</i> proteomic data sets.
Figure 13	Upstream analysis generated with Ingenuity pathway analysis (IPA) revealed p53 as potentially inhibited in its activation in MnPV- positive tissue when compared to skin control.
Figure 14	IF and ISH stainings confirm K10 reduction in MnPV-positive tissue when compared to negative tissue.
Figure 15	Volcano blot provides a general impression of the comparison of the proteomes between MnPV-infected keratinocytes vs control.
Figure 16	Altered canonical pathways (top 15) of infected murine keratinocytes when compared to control.
Figure 17	Establishment of 308 keratinocyte cell lines expressing MnPVE6, E7 or E6 and E7.
Figure 18	Comparison of the proteome of cells expressing MnPV oncoproteins and control proteome of lentivirally transduced 308 keratinocytes.
Figure 19	Venn diagram comparing the results from transduced 308 <i>in vitro</i> proteomics.
Figure 20	Altered top 15 canonical pathways in <i>in vitro</i> proteomic data sets of transduced 308 cells.
Figure 21	Wwp2 is reduced in MnPVE7- and MnPVE6E7-expressing cells when compared to control.
Figure 22	Downregulation of Cul7 in MnPVE7- and MnPVE6E7-expressing cells shown by WB.
Figure 23	Establishment of NOK cell lines expressing HPV38 oncoproteins.
Figure 24	Comparison of the proteomes of HPV38 oncoprotein-expressing and control transduced NOK cells.
Figure 25	Venn diagrams show comparison of altered proteins of <i>in vitro</i> proteomic studies of MnPV and HPV38 oncoprotein-expressing cells compared to the respective controls.

List of Figures

Figure 26	Establishment of MaFi132 cell lines to describe the interactome of MnPV E6 and E7 by BioID.
Figure 27	Illustration of MnPVE6 and E7 interaction partners identified by BioID.
Figure 28	Establishment of stable NOK cell lines to describe the interactome of E6 and E7 of HPV38 <i>via</i> BioID.
Figure 29	Comparison between interactors revealed for MnPVE6 and E7 in IP.
Figure 30	Immunoblotted IPs verifies PtpN14 as interaction partner of MnPVE7 and Maml1 binding to MnPVE6.
Figure 31	Comparison of interactomes for E6 and E7 of MnPV and HPV38 analyzed by BioID and IP.
Figure 32	PtpN14 reduction in MnPVE7-expressing murine keratinocytes.
Figure 33	Translocation of Yap/Taz towards the nucleus.
Figure 34	Members of the CUL-protein family influence various signaling pathways in the cell which are associated with the development of cancer.
Figure 35	Hypothetical consequence of MnPVE6 binding to MAML1 and SMAD2/3 on NOTCH and TGF- β signaling pathway.
Figure 36	<i>Core components of the HIPPO signaling pathway in mammals base on the dynamic change in localization of the two main effectors YAP and TAZ between nucleus and cytoplasm.</i>
Figure 37	Schematic representation of the domains of YAP and TAZ as well as their interactors and interaction binding sites.
Figure 38	Schematic illustration of the infection process of 308 murine keratinocytes using MnPV-infected tumor tissue.
Figure 39	Illustration of the dissecting process of the tissue material from <i>Mastomys coucha</i> for the subsequent proteomic analysis
Figure 40	Schematic overview of partial-proteomics workflow.
Figure 41	Interactome studies <i>via</i> BioID.
Supplemental Figure 1	Examination of smallest volume usable for lysis and further proteomic analyses.
Supplemental Figure 2	Biotinylation assays to determine the cell line to be used for BioID experiments on MnPV oncoproteins.
Supplemental Figure 3	Western blot analysis using anti-biotin antibody to detect protein biotinylation levels in cells after the addition of biotin.
Supplemental Figure 4	Venn diagram depicting a comparison of differentially expressed proteins found in <i>in vivo</i> proteomic results compared to <i>in vitro</i> proteomic results.

11 List of Tables

Table	Title
Table 1	Composition of the 308 keratinocyte medium.
Table 2	Cell lines used in this study
Table 3	Primers used in this study
Table 4	Plasmids used in this study.
Table 5	Primary antibodies used in this study.
Table 6	Secondary antibodies used in this study.
Table 7	Software and programs used in this study.
Table 8	Pipetting scheme of BSA standards.
Supplemental Table 1	Results of partial proteomics; iBAQ values.
Supplemental Table 2	Results of proteomics performed on infected 308 keratinocytes (iBAQ values).
Supplemental Table 3	Proteomic results of transduced 308 keratinocytes expressing MnPV oncoproteins (iBAQ values).
Supplemental Table 4	Proteomic results of HPV38 oncoprotein-expressing NOK cells (iBAQ values).
Supplemental Table 5	Gene names of proteins found to be significantly altered in MnPV as well as in HPV38 oncoprotein- expressing cells.

12 References

1. Scarth, J.A., et al., *The human papillomavirus oncoproteins: a review of the host pathways targeted on the road to transformation*. J Gen Virol, 2021. **102**(3).
2. Hasche, D. and F. Rosl, *Mastomys Species as Model Systems for Infectious Diseases*. Viruses, 2019. **11**(2).
3. Cid-Arregui, A., *Therapeutic vaccines against human papillomavirus and cervical cancer*. Open Virol J, 2009. **3**: p. 67-83.
4. Piccolo, S., S. Dupont, and M. Cordenonsi, *The biology of YAP/TAZ: hippo signaling and beyond*. Physiol Rev, 2014. **94**(4): p. 1287-312.
5. Chen, Z., et al., *Cullin family proteins and tumorigenesis: genetic association and molecular mechanisms*. J Cancer, 2015. **6**(3): p. 233-42.
6. Didona, D., et al., *Non Melanoma Skin Cancer Pathogenesis Overview*. Biomedicines, 2018. **6**(1).
7. Doorbar, J., et al., *The biology and life-cycle of human papillomaviruses*. Vaccine, 2012. **30 Suppl 5**: p. F55-70.
8. Varnaite, R. and S.A. MacNeill, *Meet the neighbors: Mapping local protein interactomes by proximity-dependent labeling with BioID*. Proteomics, 2016. **16**(19): p. 2503-2518.
9. Ma, S., et al., *The Hippo Pathway: Biology and Pathophysiology*. Annu Rev Biochem, 2019. **88**: p. 577-604.
10. Van Doorslaer, K., et al., *The Papillomavirus Episteme: a major update to the papillomavirus sequence database*. Nucleic Acids Res, 2017. **45**(D1): p. D499-D506.
11. Doorbar, J., et al., *Human papillomavirus molecular biology and disease association*. Rev Med Virol, 2015. **25 Suppl 1**: p. 2-23.
12. Roden, R.B.S. and P.L. Stern, *Opportunities and challenges for human papillomavirus vaccination in cancer*. Nat Rev Cancer, 2018. **18**(4): p. 240-254.
13. Arbyn, M., et al., *EUROGIN 2011 roadmap on prevention and treatment of HPV-related disease*. Int J Cancer, 2012. **131**(9): p. 1969-82.
14. Brisson, M., et al., *Population-level impact, herd immunity, and elimination after human papillomavirus vaccination: a systematic review and meta-analysis of predictions from transmission-dynamic models*. Lancet Public Health, 2016. **1**(1): p. e8-e17.
15. Joura, E., O. Bautista, and A. Luxembourg, *A 9-Valent HPV Vaccine in Women*. N Engl J Med, 2015. **372**(26): p. 2568-9.
16. Muhr, L.S.A., C. Eklund, and J. Dillner, *Towards quality and order in human papillomavirus research*. Virology, 2018. **519**: p. 74-76.
17. Antonsson, A., et al., *The ubiquity and impressive genomic diversity of human skin papillomaviruses suggest a commensalic nature of these viruses*. J Virol, 2000. **74**(24): p. 11636-41.
18. de Koning, M.N.C., et al., *Prevalence and associated factors of betapapillomavirus infections in individuals without cutaneous squamous cell carcinoma*. J Gen Virol, 2009. **90**(Pt 7): p. 1611-1621.
19. Bouwes Bavinck, J.N., et al., *Multicenter study of the association between betapapillomavirus infection and cutaneous squamous cell carcinoma*. Cancer Res, 2010. **70**(23): p. 9777-86.
20. Hsu, J.Y., et al., *Shared and persistent asymptomatic cutaneous human papillomavirus infections in healthy skin*. J Med Virol, 2009. **81**(8): p. 1444-9.
21. Antonsson, A., et al., *General acquisition of human papillomavirus infections of skin occurs in early infancy*. J Clin Microbiol, 2003. **41**(6): p. 2509-14.

22. Weissenborn, S.J., et al., *Intrafamilial transmission and family-specific spectra of cutaneous betapapillomaviruses*. J Virol, 2009. **83**(2): p. 811-6.
23. Plasmeyer, E.I., et al., *Epidemiology of cutaneous human papillomavirus infections*. Cancer Treat Res, 2009. **146**: p. 143-57.
24. Egawa, N., et al., *Human Papillomaviruses; Epithelial Tropisms, and the Development of Neoplasia*. Viruses, 2015. **7**(7): p. 3863-90.
25. Howley, P.M. and H.J. Pfister, *Beta genus papillomaviruses and skin cancer*. Virology, 2015. **479-480**: p. 290-6.
26. Orth, G., *Host defenses against human papillomaviruses: lessons from epidermodysplasia verruciformis*. Curr Top Microbiol Immunol, 2008. **321**: p. 59-83.
27. Orth, G., et al., *Characterization of two types of human papillomaviruses in lesions of epidermodysplasia verruciformis*. Proc Natl Acad Sci U S A, 1978. **75**(3): p. 1537-41.
28. Blakaj, D.M., et al., *Evolutionary and biophysical relationships among the papillomavirus E2 proteins*. Front Biosci (Landmark Ed), 2009. **14**(3): p. 900-17.
29. Doorbar, J., *Molecular biology of human papillomavirus infection and cervical cancer*. Clin Sci (Lond), 2006. **110**(5): p. 525-41.
30. Borgogna, C., et al., *Characterization of beta papillomavirus E4 expression in tumours from Epidermodysplasia Verruciformis patients and in experimental models*. Virology, 2012. **423**(2): p. 195-204.
31. de Freitas, A.C., et al., *hrHPV E5 oncoprotein: immune evasion and related immunotherapies*. J Exp Clin Cancer Res, 2017. **36**(1): p. 71.
32. Ashrafi, G.H., et al., *Down-regulation of MHC class I is a property common to papillomavirus E5 proteins*. Virus Res, 2006. **120**(1-2): p. 208-11.
33. Florin, L., et al., *Assembly and translocation of papillomavirus capsid proteins*. J Virol, 2002. **76**(19): p. 10009-14.
34. Bodily, J. and L.A. Laimins, *Persistence of human papillomavirus infection: keys to malignant progression*. Trends Microbiol, 2011. **19**(1): p. 33-9.
35. Johansson, C. and S. Schwartz, *Regulation of human papillomavirus gene expression by splicing and polyadenylation*. Nat Rev Microbiol, 2013. **11**(4): p. 239-51.
36. Trosko, J.E., *Human adult stem cells as the target cells for the initiation of carcinogenesis and for the generation of "cancer stem cells"*. Int J Stem Cells, 2008. **1**(1): p. 8-26.
37. Blanpain, C. and E. Fuchs, *Epidermal homeostasis: a balancing act of stem cells in the skin*. Nat Rev Mol Cell Biol, 2009. **10**(3): p. 207-17.
38. Blanpain, C., V. Horsley, and E. Fuchs, *Epithelial stem cells: turning over new leaves*. Cell, 2007. **128**(3): p. 445-58.
39. Santos, M., et al., *The expression of keratin k10 in the basal layer of the epidermis inhibits cell proliferation and prevents skin tumorigenesis*. J Biol Chem, 2002. **277**(21): p. 19122-30.
40. Coulombe, P.A., R. Kopan, and E. Fuchs, *Expression of keratin K14 in the epidermis and hair follicle: insights into complex programs of differentiation*. J Cell Biol, 1989. **109**(5): p. 2295-312.
41. Murphy, G.F., et al., *Involucrin expression in normal and neoplastic human skin: a marker for keratinocyte differentiation*. J Invest Dermatol, 1984. **82**(5): p. 453-7.
42. Wikramanayake, T.C., O. Stojadinovic, and M. Tomic-Canic, *Epidermal Differentiation in Barrier Maintenance and Wound Healing*. Adv Wound Care (New Rochelle), 2014. **3**(3): p. 272-280.
43. Blanpain, C. and E. Fuchs, *Epidermal stem cells of the skin*. Annu Rev Cell Dev Biol, 2006. **22**: p. 339-73.

References

44. Hasche, D., et al., *The interplay of UV and cutaneous papillomavirus infection in skin cancer development*. PLoS Pathog, 2017. **13**(11): p. e1006723.
45. Friedmann-Morvinski, D. and I.M. Verma, *Dedifferentiation and reprogramming: origins of cancer stem cells*. EMBO Rep, 2014. **15**(3): p. 244-53.
46. Jogi, A., et al., *Cancer cell differentiation heterogeneity and aggressive behavior in solid tumors*. Ups J Med Sci, 2012. **117**(2): p. 217-24.
47. Gestblom, C., et al., *In vivo spontaneous neuronal to neuroendocrine lineage conversion in a subset of neuroblastomas*. Am J Pathol, 1997. **150**(1): p. 107-17.
48. Hedborg, F., et al., *IGF2 expression is a marker for paraganglionic/SIF cell differentiation in neuroblastoma*. Am J Pathol, 1995. **146**(4): p. 833-47.
49. DiGiuseppe, S., et al., *Cruising the cellular highways: How human papillomavirus travels from the surface to the nucleus*. Virus Res, 2017. **231**: p. 1-9.
50. Day, P.M., et al., *Establishment of papillomavirus infection is enhanced by promyelocytic leukemia protein (PML) expression*. Proc Natl Acad Sci U S A, 2004. **101**(39): p. 14252-7.
51. Zheng, Z.M. and C.C. Baker, *Papillomavirus genome structure, expression, and post-transcriptional regulation*. Front Biosci, 2006. **11**: p. 2286-302.
52. Maglennon, G.A., P. McIntosh, and J. Doorbar, *Persistence of viral DNA in the epithelial basal layer suggests a model for papillomavirus latency following immune regression*. Virology, 2011. **414**(2): p. 153-63.
53. Berg, M. and A. Stenlund, *Functional interactions between papillomavirus E1 and E2 proteins*. J Virol, 1997. **71**(5): p. 3853-63.
54. Dreer, M., et al., *Interaction of NCOR/SMRT Repressor Complexes with Papillomavirus E8^{E2C} Proteins Inhibits Viral Replication*. PLoS Pathog, 2016. **12**(4): p. e1005556.
55. Doorbar, J., *The E4 protein; structure, function and patterns of expression*. Virology, 2013. **445**(1-2): p. 80-98.
56. Doorbar, J., et al., *Specific interaction between HPV-16 E1-E4 and cytokeratins results in collapse of the epithelial cell intermediate filament network*. Nature, 1991. **352**(6338): p. 824-7.
57. Chen, S.L. and P. Mounts, *Transforming activity of E5a protein of human papillomavirus type 6 in NIH 3T3 and C127 cells*. J Virol, 1990. **64**(7): p. 3226-33.
58. Leechanachai, P., et al., *The E5 gene from human papillomavirus type 16 is an oncogene which enhances growth factor-mediated signal transduction to the nucleus*. Oncogene, 1992. **7**(1): p. 19-25.
59. Leptak, C., et al., *Tumorigenic transformation of murine keratinocytes by the E5 genes of bovine papillomavirus type 1 and human papillomavirus type 16*. J Virol, 1991. **65**(12): p. 7078-83.
60. Kabsch, K., et al., *The HPV-16 E5 protein inhibits TRAIL- and FasL-mediated apoptosis in human keratinocyte raft cultures*. Intervirology, 2004. **47**(1): p. 48-56.
61. Supryniewicz, F.A., et al., *The human papillomavirus type 16 E5 oncoprotein inhibits epidermal growth factor trafficking independently of endosome acidification*. J Virol, 2010. **84**(20): p. 10619-29.
62. Thomsen, P., et al., *The HPV16 E5 oncogene inhibits endocytic trafficking*. Oncogene, 2000. **19**(52): p. 6023-32.
63. McBride, A.A., *The papillomavirus E2 proteins*. Virology, 2013. **445**(1-2): p. 57-79.
64. Banerjee, N.S., et al., *Human papillomavirus (HPV) E7 induces prolonged G2 following S phase reentry in differentiated human keratinocytes*. J Biol Chem, 2011. **286**(17): p. 15473-82.

65. Wang, H.K., et al., *Robust production and passaging of infectious HPV in squamous epithelium of primary human keratinocytes*. *Genes Dev*, 2009. **23**(2): p. 181-94.
66. Longworth, M.S. and L.A. Laimins, *Pathogenesis of human papillomaviruses in differentiating epithelia*. *Microbiol Mol Biol Rev*, 2004. **68**(2): p. 362-72.
67. Tsunokawa, Y., et al., *Transforming activity of human papillomavirus type 16 DNA sequence in a cervical cancer*. *Proc Natl Acad Sci U S A*, 1986. **83**(7): p. 2200-3.
68. Yasumoto, S., et al., *Human papillomavirus type 16 DNA-induced malignant transformation of NIH 3T3 cells*. *J Virol*, 1986. **57**(2): p. 572-7.
69. Arbeit, J.M., et al., *Progressive squamous epithelial neoplasia in K14-human papillomavirus type 16 transgenic mice*. *J Virol*, 1994. **68**(7): p. 4358-68.
70. Lambert, P.F., et al., *Epidermal cancer associated with expression of human papillomavirus type 16 E6 and E7 oncogenes in the skin of transgenic mice*. *Proc Natl Acad Sci U S A*, 1993. **90**(12): p. 5583-7.
71. Riley, R.R., et al., *Dissection of human papillomavirus E6 and E7 function in transgenic mouse models of cervical carcinogenesis*. *Cancer Res*, 2003. **63**(16): p. 4862-71.
72. Shai, A., et al., *The human papillomavirus E6 oncogene dysregulates the cell cycle and contributes to cervical carcinogenesis through two independent activities*. *Cancer Res*, 2007. **67**(4): p. 1626-35.
73. Gariglio, P., et al., *The role of retinoid deficiency and estrogens as cofactors in cervical cancer*. *Arch Med Res*, 2009. **40**(6): p. 449-65.
74. Arbeit, J.M., P.M. Howley, and D. Hanahan, *Chronic estrogen-induced cervical and vaginal squamous carcinogenesis in human papillomavirus type 16 transgenic mice*. *Proc Natl Acad Sci U S A*, 1996. **93**(7): p. 2930-5.
75. Liu, Y., et al., *Determinants of stability for the E6 protein of papillomavirus type 16*. *J Mol Biol*, 2009. **386**(4): p. 1123-37.
76. Barbosa, M.S., D.R. Lowy, and J.T. Schiller, *Papillomavirus polypeptides E6 and E7 are zinc-binding proteins*. *J Virol*, 1989. **63**(3): p. 1404-7.
77. Roman, A., *The human papillomavirus E7 protein shines a spotlight on the pRB family member, p130*. *Cell Cycle*, 2006. **5**(6): p. 567-8.
78. Collins, A.S., et al., *Interactions with pocket proteins contribute to the role of human papillomavirus type 16 E7 in the papillomavirus life cycle*. *J Virol*, 2005. **79**(23): p. 14769-80.
79. White, E.A., et al., *Systematic identification of interactions between host cell proteins and E7 oncoproteins from diverse human papillomaviruses*. *Proc Natl Acad Sci U S A*, 2012. **109**(5): p. E260-7.
80. White, E.A. and P.M. Howley, *Proteomic approaches to the study of papillomavirus-host interactions*. *Virology*, 2013. **435**(1): p. 57-69.
81. Martinez-Zapien, D., et al., *Structure of the E6/E6AP/p53 complex required for HPV-mediated degradation of p53*. *Nature*, 2016. **529**(7587): p. 541-5.
82. Patel, D., et al., *The E6 protein of human papillomavirus type 16 binds to and inhibits co-activation by CBP and p300*. *EMBO J*, 1999. **18**(18): p. 5061-72.
83. Schwarz, T. and A. Schwarz, *DNA repair and cytokine responses*. *J Investig Dermatol Symp Proc*, 2009. **14**(1): p. 63-6.
84. Viarisio, D., et al., *Beta HPV38 oncoproteins act with a hit-and-run mechanism in ultraviolet radiation-induced skin carcinogenesis in mice*. *PLoS Pathog*, 2018. **14**(1): p. e1006783.
85. Viarisio, D., et al., *Novel ss-HPV49 Transgenic Mouse Model of Upper Digestive Tract Cancer*. *Cancer Res*, 2016. **76**(14): p. 4216-25.
86. Smith, J.S., et al., *Human papillomavirus type distribution in invasive cervical cancer and high-grade cervical lesions: a meta-analysis update*. *Int J Cancer*, 2007. **121**(3): p. 621-32.

References

87. Accardi, R., et al., *Skin human papillomavirus type 38 alters p53 functions by accumulation of deltaNp73*. EMBO Rep, 2006. **7**(3): p. 334-40.
88. Giampieri, S. and A. Storey, *Repair of UV-induced thymine dimers is compromised in cells expressing the E6 protein from human papillomaviruses types 5 and 18*. Br J Cancer, 2004. **90**(11): p. 2203-9.
89. Wallace, N.A., et al., *HPV 5 and 8 E6 abrogate ATR activity resulting in increased persistence of UVB induced DNA damage*. PLoS Pathog, 2012. **8**(7): p. e1002807.
90. Muench, P., et al., *Cutaneous papillomavirus E6 proteins must interact with p300 and block p53-mediated apoptosis for cellular immortalization and tumorigenesis*. Cancer Res, 2010. **70**(17): p. 6913-24.
91. Hufbauer, M., et al., *Human papillomavirus mediated inhibition of DNA damage sensing and repair drives skin carcinogenesis*. Mol Cancer, 2015. **14**: p. 183.
92. Yu, H., *Chk1: a double agent in cell cycle checkpoints*. Dev Cell, 2007. **12**(2): p. 167-8.
93. Adams, J.M. and S. Cory, *Apoptosomes: engines for caspase activation*. Curr Opin Cell Biol, 2002. **14**(6): p. 715-20.
94. Quint, K.D., et al., *Human Beta-papillomavirus infection and keratinocyte carcinomas*. J Pathol, 2015. **235**(2): p. 342-54.
95. Cardoso, J.C. and E. Calonje, *Cutaneous manifestations of human papillomaviruses: a review*. Acta Dermatovenerol Alp Pannonica Adriat, 2011. **20**(3): p. 145-54.
96. Wieland, C.N., et al., *The role of CD10 in distinguishing atypical fibroxanthoma from sarcomatoid (spindle cell) squamous cell carcinoma*. J Cutan Pathol, 2011. **38**(11): p. 884-8.
97. Jones, D.L. and K. Munger, *Interactions of the human papillomavirus E7 protein with cell cycle regulators*. Semin Cancer Biol, 1996. **7**(6): p. 327-37.
98. Lipinski, M.M. and T. Jacks, *The retinoblastoma gene family in differentiation and development*. Oncogene, 1999. **18**(55): p. 7873-82.
99. Caldeira, S., et al., *The E6 and E7 proteins of the cutaneous human papillomavirus type 38 display transforming properties*. J Virol, 2003. **77**(3): p. 2195-206.
100. Akgul, B., et al., *The E7 protein of cutaneous human papillomavirus type 8 causes invasion of human keratinocytes into the dermis in organotypic cultures of skin*. Cancer Res, 2005. **65**(6): p. 2216-23.
101. Akgul, B., et al., *Human papillomavirus type 8 oncoproteins E6 and E7 cooperate in downregulation of the cellular checkpoint kinase-1*. Int J Cancer, 2019. **145**(3): p. 797-806.
102. Heuser, S., et al., *The levels of epithelial anchor proteins beta-catenin and zona occludens-1 are altered by E7 of human papillomaviruses 5 and 8*. J Gen Virol, 2016. **97**(2): p. 463-472.
103. Lomas, A., J. Leonardi-Bee, and F. Bath-Hextall, *A systematic review of worldwide incidence of nonmelanoma skin cancer*. Br J Dermatol, 2012. **166**(5): p. 1069-80.
104. Kraft, S. and S.R. Granter, *Molecular pathology of skin neoplasms of the head and neck*. Arch Pathol Lab Med, 2014. **138**(6): p. 759-87.
105. Filosa, A. and G. Filosa, *Actinic keratosis and squamous cell carcinoma: clinical and pathological features*. G Ital Dermatol Venereol, 2015. **150**(4): p. 379-84.
106. Lober, B.A. and C.W. Lober, *Actinic keratosis is squamous cell carcinoma*. South Med J, 2000. **93**(7): p. 650-5.
107. Mofidi, A., et al., *The economic burden of occupational non-melanoma skin cancer due to solar radiation*. J Occup Environ Hyg, 2018. **15**(6): p. 481-491.
108. Fransen, M., et al., *Non-melanoma skin cancer in Australia*. Med J Aust, 2012. **197**(10): p. 565-8.
109. Jablonska, S., J. Dabrowski, and K. Jakubowicz, *Epidermodysplasia verruciformis as a model in studies on the role of papovaviruses in oncogenesis*. Cancer Res, 1972. **32**(3): p. 583-9.

110. Pfister, H., *Chapter 8: Human papillomavirus and skin cancer*. J Natl Cancer Inst Monogr, 2003(31): p. 52-6.
111. Borgogna, C., et al., *Improved detection reveals active beta-papillomavirus infection in skin lesions from kidney transplant recipients*. Mod Pathol, 2014. **27**(8): p. 1101-15.
112. Plasmeijer, E.I., et al., *Persistence of betapapillomavirus infections as a risk factor for actinic keratoses, precursor to cutaneous squamous cell carcinoma*. Cancer Res, 2009. **69**(23): p. 8926-31.
113. Karagas, M.R., et al., *Human papillomavirus infection and incidence of squamous cell and basal cell carcinomas of the skin*. J Natl Cancer Inst, 2006. **98**(6): p. 389-95.
114. Wang, J., et al., *Role of human papillomavirus in cutaneous squamous cell carcinoma: a meta-analysis*. J Am Acad Dermatol, 2014. **70**(4): p. 621-629.
115. Hampras, S.S., et al., *Cutaneous Human Papillomavirus Infection and Development of Subsequent Squamous Cell Carcinoma of the Skin*. J Skin Cancer, 2016. **2016**: p. 1368103.
116. Nindl, I., et al., *Detection of human papillomavirus DNA in primary squamous cell carcinoma and metastases*. Br J Dermatol, 2006. **154**(4): p. 797-9.
117. Meyer, T., et al., *Importance of human papillomaviruses for the development of skin cancer*. Cancer Detect Prev, 2001. **25**(6): p. 533-47.
118. Forslund, O., *Genetic diversity of cutaneous human papillomaviruses*. J Gen Virol, 2007. **88**(Pt 10): p. 2662-2669.
119. Genders, R.E., et al., *The presence of betapapillomavirus antibodies around transplantation predicts the development of keratinocyte carcinoma in organ transplant recipients: a cohort study*. J Invest Dermatol, 2015. **135**(5): p. 1275-1282.
120. Jackson, S., et al., *Role of Bak in UV-induced apoptosis in skin cancer and abrogation by HPV E6 proteins*. Genes Dev, 2000. **14**(23): p. 3065-73.
121. Forslund, O., et al., *A broad spectrum of human papillomavirus types is present in the skin of Australian patients with non-melanoma skin cancers and solar keratosis*. Br J Dermatol, 2003. **149**(1): p. 64-73.
122. Arron, S.T., et al., *Viral oncogenesis and its role in nonmelanoma skin cancer*. Br J Dermatol, 2011. **164**(6): p. 1201-13.
123. Nindl, I., M. Gottschling, and E. Stockfleth, *Human papillomaviruses and non-melanoma skin cancer: basic virology and clinical manifestations*. Dis Markers, 2007. **23**(4): p. 247-59.
124. Hasche, D., S.E. Vinzon, and F. Rosl, *Cutaneous Papillomaviruses and Non-melanoma Skin Cancer: Causal Agents or Innocent Bystanders?* Front Microbiol, 2018. **9**: p. 874.
125. Nafz, J., et al., *A novel rodent papillomavirus isolated from anogenital lesions in its natural host*. Virology, 2008. **374**(1): p. 186-97.
126. Nafz, J., et al., *Persistence of Mastomys natalensis papillomavirus in multiple organs identifies novel targets for infection*. J Gen Virol, 2007. **88**(Pt 10): p. 2670-2678.
127. Hardin, A., et al., *Comparative Genomic Characterization of the Multimammate Mouse Mastomys coucha*. Mol Biol Evol, 2019. **36**(12): p. 2805-2812.
128. Burtscher, H., W. Grunberg, and G. Meingassner, *[Infectious keratoacanthomas of the epidermis in Praomys (Mastomys) natalensis]*. Naturwissenschaften, 1973. **60**(4): p. 209-10.
129. Rudolph, R. and W. Thiel, *[Pathological anatomy and histology of spontaneous, epithelial skin tumors in Mastomys natalensis]*. Zentralbl Veterinarmed A, 1976. **23**(05): p. 429-41.
130. Rudolph, R.L., et al., *Morphology of experimentally induced so-called keratoacanthomas and squamous cell carcinomas in 2 inbred-lines of Mastomys natalensis*. J Comp Pathol, 1981. **91**(1): p. 123-34.
131. Schafer, K., et al., *Serological markers for papillomavirus infection and skin tumour development in the rodent model Mastomys coucha*. J Gen Virol, 2011. **92**(Pt 2): p. 383-94.

References

132. Hasche, D., et al., *Isoforms of the Papillomavirus Major Capsid Protein Differ in Their Ability to Block Viral Spread and Tumor Formation*. *Front Immunol*, 2022. **13**: p. 811094.
133. Tan, C.H., et al., *The Mastomys natalensis papillomavirus: nucleotide sequence, genome organization, and phylogenetic relationship of a rodent papillomavirus involved in tumorigenesis of cutaneous epithelia*. *Virology*, 1994. **198**(2): p. 534-41.
134. Hughes, C.S., et al., *Ultrasensitive proteome analysis using paramagnetic bead technology*. *Mol Syst Biol*, 2014. **10**: p. 757.
135. Cox, J., et al., *Accurate proteome-wide label-free quantification by delayed normalization and maximal peptide ratio extraction, termed MaxLFQ*. *Mol Cell Proteomics*, 2014. **13**(9): p. 2513-26.
136. Heppner, G.H., *Tumor heterogeneity*. *Cancer Res*, 1984. **44**(6): p. 2259-65.
137. Fidler, I.J. and I.R. Hart, *Biological diversity in metastatic neoplasms: origins and implications*. *Science*, 1982. **217**(4564): p. 998-1003.
138. Dick, J.E., *Stem cell concepts renew cancer research*. *Blood*, 2008. **112**(13): p. 4793-807.
139. Nicolson, G.L., *Generation of phenotypic diversity and progression in metastatic tumor cells*. *Cancer Metastasis Rev*, 1984. **3**(1): p. 25-42.
140. Curatolo, P., *Mechanistic target of rapamycin (mTOR) in tuberous sclerosis complex-associated epilepsy*. *Pediatr Neurol*, 2015. **52**(3): p. 281-9.
141. Bhat, M., et al., *Targeting the translation machinery in cancer*. *Nat Rev Drug Discov*, 2015. **14**(4): p. 261-78.
142. Grafanaki, K., et al., *Translation regulation in skin cancer from a tRNA point of view*. *Epigenomics*, 2019. **11**(2): p. 215-245.
143. Akgul, B., J.C. Cooke, and A. Storey, *HPV-associated skin disease*. *J Pathol*, 2006. **208**(2): p. 165-75.
144. Strickland, J.E., et al., *Development of murine epidermal cell lines which contain an activated rasHa oncogene and form papillomas in skin grafts on athymic nude mouse hosts*. *Cancer Res*, 1988. **48**(1): p. 165-9.
145. Harvey, K.F., C.M. Pflieger, and I.K. Hariharan, *The Drosophila Mst ortholog, hippo, restricts growth and cell proliferation and promotes apoptosis*. *Cell*, 2003. **114**(4): p. 457-67.
146. Udan, R.S., et al., *Hippo promotes proliferation arrest and apoptosis in the Salvador/Warts pathway*. *Nat Cell Biol*, 2003. **5**(10): p. 914-20.
147. Pantalacci, S., N. Tapon, and P. Leopold, *The Salvador partner Hippo promotes apoptosis and cell-cycle exit in Drosophila*. *Nat Cell Biol*, 2003. **5**(10): p. 921-7.
148. He, C., et al., *The Hippo/YAP pathway interacts with EGFR signaling and HPV oncoproteins to regulate cervical cancer progression*. *EMBO Mol Med*, 2015. **7**(11): p. 1426-49.
149. Webb Strickland, S., et al., *Human Papillomavirus E6 interaction with cellular PDZ domain proteins modulates YAP nuclear localization*. *Virology*, 2018. **516**: p. 127-138.
150. Hatterschide, J., et al., *PTPN14 degradation by high-risk human papillomavirus E7 limits keratinocyte differentiation and contributes to HPV-mediated oncogenesis*. *Proc Natl Acad Sci U S A*, 2019. **116**(14): p. 7033-7042.
151. Schwanhausser, B., et al., *Global quantification of mammalian gene expression control*. *Nature*, 2011. **473**(7347): p. 337-42.
152. Baggelaar, M.P., M. Maccarrone, and M. van der Stelt, *2-Arachidonoylglycerol: A signaling lipid with manifold actions in the brain*. *Prog Lipid Res*, 2018. **71**: p. 1-17.
153. Carracedo, A., et al., *The stress-regulated protein p8 mediates cannabinoid-induced apoptosis of tumor cells*. *Cancer Cell*, 2006. **9**(4): p. 301-12.
154. Sarfaraz, S., et al., *Cannabinoids for cancer treatment: progress and promise*. *Cancer Res*, 2008. **68**(2): p. 339-42.

155. Laezza, C., et al., *Anandamide inhibits the Wnt/beta-catenin signalling pathway in human breast cancer MDA MB 231 cells*. Eur J Cancer, 2012. **48**(16): p. 3112-22.
156. Vara, D., et al., *Anti-tumoral action of cannabinoids on hepatocellular carcinoma: role of AMPK-dependent activation of autophagy*. Cell Death Differ, 2011. **18**(7): p. 1099-111.
157. Chen, W., X. Jiang, and Z. Luo, *WWP2: a multifunctional ubiquitin ligase gene*. Pathol Oncol Res, 2014. **20**(4): p. 799-803.
158. Chen, A., et al., *The HECT-type E3 ubiquitin ligase AIP2 inhibits activation-induced T-cell death by catalyzing EGR2 ubiquitination*. Mol Cell Biol, 2009. **29**(19): p. 5348-56.
159. Li, H., et al., *Wwp2-mediated ubiquitination of the RNA polymerase II large subunit in mouse embryonic pluripotent stem cells*. Mol Cell Biol, 2007. **27**(15): p. 5296-305.
160. Sarikas, A., et al., *The cullin7 E3 ubiquitin ligase: a novel player in growth control*. Cell Cycle, 2008. **7**(20): p. 3154-61.
161. Wang, H., et al., *The CUL7/F-box and WD repeat domain containing 8 (CUL7/Fbxw8) ubiquitin ligase promotes degradation of hematopoietic progenitor kinase 1*. J Biol Chem, 2014. **289**(7): p. 4009-17.
162. Hu, C. and N. Wallace, *Beta HPV Deregulates Double-Strand Break Repair*. Viruses, 2022. **14**(5).
163. Aubin, F., et al., *Effect of Infliximab on the UVB-Induced Apoptosis of Keratinocytes Infected by HPV38 E6/E7*. ISRN Dermatol, 2013. **2013**: p. 907189.
164. Viarisio, D., et al., *Correction: E6 and E7 from Beta Hpv38 Cooperate with Ultraviolet Light in the Development of Actinic Keratosis-Like Lesions and Squamous Cell Carcinoma in Mice*. PLoS Pathog, 2016. **12**(10): p. e1006005.
165. Roux, K.J., et al., *BioID: A Screen for Protein-Protein Interactions*. Curr Protoc Protein Sci, 2018. **91**: p. 19 23 1-19 23 15.
166. Gersten, D.M. and J.J. Marchalonis, *A rapid, novel method for the solid-phase derivatization of IgG antibodies for immune-affinity chromatography*. J Immunol Methods, 1978. **24**(3-4): p. 305-9.
167. Roux, K.J., et al., *A promiscuous biotin ligase fusion protein identifies proximal and interacting proteins in mammalian cells*. J Cell Biol, 2012. **196**(6): p. 801-10.
168. Hasche, D., et al., *Establishment of an Immortalized Skin Keratinocyte Cell Line Derived from the Animal Model Mastomys coucha*. PLoS One, 2016. **11**(8): p. e0161283.
169. Khammanivong, A., et al., *S100A8/A9 (calprotectin) negatively regulates G2/M cell cycle progression and growth of squamous cell carcinoma*. PLoS One, 2013. **8**(7): p. e69395.
170. Silva, E.J., et al., *S100A8/A9 regulates MMP-2 expression and invasion and migration by carcinoma cells*. Int J Biochem Cell Biol, 2014. **55**: p. 279-87.
171. Cormier, K., et al., *Intracellular expression of inflammatory proteins S100A8 and S100A9 leads to epithelial-mesenchymal transition and attenuated aggressivity of breast cancer cells*. Anticancer Agents Med Chem, 2014. **14**(1): p. 35-45.
172. Shabani, F., et al., *Calprotectin (S100A8/S100A9): a key protein between inflammation and cancer*. Inflamm Res, 2018. **67**(10): p. 801-812.
173. Khammanivong, A., et al., *Involvement of calprotectin (S100A8/A9) in molecular pathways associated with HNSCC*. Oncotarget, 2016. **7**(12): p. 14029-47.
174. Altomare, D., et al., *Partial loss of Smad signaling during in vitro progression of HPV16-immortalized human keratinocytes*. BMC Cancer, 2013. **13**: p. 424.
175. Brimer, N., C.M. Drews, and S.B. Vande Pol, *Association of papillomavirus E6 proteins with either MAML1 or E6AP clusters E6 proteins by structure, function, and evolutionary relatedness*. PLoS Pathog, 2017. **13**(12): p. e1006781.

References

176. Tan, M.J., et al., *Cutaneous beta-human papillomavirus E6 proteins bind Mastermind-like coactivators and repress Notch signaling*. Proc Natl Acad Sci U S A, 2012. **109**(23): p. E1473-80.
177. Liu, X., et al., *PTPN14 interacts with and negatively regulates the oncogenic function of YAP*. Oncogene, 2013. **32**(10): p. 1266-73.
178. Sero, J.E. and C. Bakal, *Multiparametric Analysis of Cell Shape Demonstrates that beta-PIX Directly Couples YAP Activation to Extracellular Matrix Adhesion*. Cell Syst, 2017. **4**(1): p. 84-96 e6.
179. Sorrentino, G., et al., *Metabolic control of YAP and TAZ by the mevalonate pathway*. Nat Cell Biol, 2014. **16**(4): p. 357-66.
180. Wilkins, M.R., et al., *Progress with proteome projects: why all proteins expressed by a genome should be identified and how to do it*. Biotechnol Genet Eng Rev, 1996. **13**: p. 19-50.
181. Aslam, B., et al., *Proteomics: Technologies and Their Applications*. J Chromatogr Sci, 2017. **55**(2): p. 182-196.
182. Cox, J. and M. Mann, *Is proteomics the new genomics?* Cell, 2007. **130**(3): p. 395-8.
183. Di Domenico, F., F. De Marco, and M. Perluigi, *Proteomics strategies to analyze HPV-transformed cells: relevance to cervical cancer*. Expert Rev Proteomics, 2013. **10**(5): p. 461-72.
184. Carrillo, D., et al., *Upregulation of PIR gene expression induced by human papillomavirus E6 and E7 in epithelial oral and cervical cells*. Open Biol, 2017. **7**(11).
185. Cicchini, L., et al., *High-Risk Human Papillomavirus E7 Alters Host DNA Methylome and Represses HLA-E Expression in Human Keratinocytes*. Sci Rep, 2017. **7**(1): p. 3633.
186. Gyongyosi, E., et al., *Transcriptional regulation of genes involved in keratinocyte differentiation by human papillomavirus 16 oncoproteins*. Arch Virol, 2015. **160**(2): p. 389-98.
187. Peta, E., et al., *HPV16 E6 and E7 upregulate the histone lysine demethylase KDM2B through the c-MYC/miR-146a-5p axis*. Oncogene, 2018. **37**(12): p. 1654-1668.
188. Mwapagha, L.M., N. Tiffin, and M.I. Parker, *Delineation of the HPV11E6 and HPV18E6 Pathways in Initiating Cellular Transformation*. Front Oncol, 2017. **7**: p. 258.
189. Jopling, C., S. Boue, and J.C. Izpisua Belmonte, *Dedifferentiation, transdifferentiation and reprogramming: three routes to regeneration*. Nat Rev Mol Cell Biol, 2011. **12**(2): p. 79-89.
190. Delaunay, S., et al., *Mitochondrial RNA modifications shape metabolic plasticity in metastasis*. Nature, 2022. **607**(7919): p. 593-603.
191. Danhier, P., et al., *Cancer metabolism in space and time: Beyond the Warburg effect*. Biochim Biophys Acta Bioenerg, 2017. **1858**(8): p. 556-572.
192. Zou, Z., et al., *mTOR signaling pathway and mTOR inhibitors in cancer: progress and challenges*. Cell Biosci, 2020. **10**: p. 31.
193. Vadlakonda, L., M. Pasupuleti, and R. Pallu, *Role of PI3K-AKT-mTOR and Wnt Signaling Pathways in Transition of G1-S Phase of Cell Cycle in Cancer Cells*. Front Oncol, 2013. **3**: p. 85.
194. Chen, Y. and X. Zhou, *Research progress of mTOR inhibitors*. Eur J Med Chem, 2020. **208**: p. 112820.
195. Zhang, L., et al., *The role of the PI3K/Akt/mTOR signalling pathway in human cancers induced by infection with human papillomaviruses*. Mol Cancer, 2015. **14**: p. 87.
196. Wang, H., et al., *Pregnane X receptor activation induces FGF19-dependent tumor aggressiveness in humans and mice*. J Clin Invest, 2011. **121**(8): p. 3220-32.
197. Zhou, J., et al., *The antiapoptotic role of pregnane X receptor in human colon cancer cells*. Mol Endocrinol, 2008. **22**(4): p. 868-80.

198. Saradhi, M., et al., *Pregnane and Xenobiotic Receptor (PXR/SXR) resides predominantly in the nuclear compartment of the interphase cell and associates with the condensed chromosomes during mitosis*. *Biochim Biophys Acta*, 2005. **1746**(2): p. 85-94.
199. Masuyama, H., et al., *Down-regulation of pregnane X receptor contributes to cell growth inhibition and apoptosis by anticancer agents in endometrial cancer cells*. *Mol Pharmacol*, 2007. **72**(4): p. 1045-53.
200. Zucchini, N., et al., *Regulation of Bcl-2 and Bcl-xL anti-apoptotic protein expression by nuclear receptor PXR in primary cultures of human and rat hepatocytes*. *Biochim Biophys Acta*, 2005. **1745**(1): p. 48-58.
201. Xing, Y., J. Yan, and Y. Niu, *PXR: a center of transcriptional regulation in cancer*. *Acta Pharm Sin B*, 2020. **10**(2): p. 197-206.
202. Lee, S.W., et al., *Tumor cell growth inhibition by caveolin re-expression in human breast cancer cells*. *Oncogene*, 1998. **16**(11): p. 1391-7.
203. Stewart, D., et al., *Ubiquitination and proteasome degradation of the E6 proteins of human papillomavirus types 11 and 18*. *J Gen Virol*, 2004. **85**(Pt 6): p. 1419-1426.
204. Wise-Draper, T.M. and S.I. Wells, *Papillomavirus E6 and E7 proteins and their cellular targets*. *Front Biosci*, 2008. **13**: p. 1003-17.
205. Hatterschide, J., et al., *YAP1 activation by human papillomavirus E7 promotes basal cell identity in squamous epithelia*. *Elife*, 2022. **11**.
206. Pan, D., *The hippo signaling pathway in development and cancer*. *Dev Cell*, 2010. **19**(4): p. 491-505.
207. Halder, G. and R.L. Johnson, *Hippo signaling: growth control and beyond*. *Development*, 2011. **138**(1): p. 9-22.
208. Varelas, X., *The Hippo pathway effectors TAZ and YAP in development, homeostasis and disease*. *Development*, 2014. **141**(8): p. 1614-26.
209. Hatterschide, J., et al., *A Conserved Amino Acid in the C Terminus of Human Papillomavirus E7 Mediates Binding to PTPN14 and Repression of Epithelial Differentiation*. *J Virol*, 2020. **94**(17).
210. Dickson, M.A., et al., *Human keratinocytes that express hTERT and also bypass a p16(INK4a)-enforced mechanism that limits life span become immortal yet retain normal growth and differentiation characteristics*. *Mol Cell Biol*, 2000. **20**(4): p. 1436-47.
211. Nomura, N., et al., *Prediction of the coding sequences of unidentified human genes. I. The coding sequences of 40 new genes (KIAA0001-KIAA0040) deduced by analysis of randomly sampled cDNA clones from human immature myeloid cell line KG-1*. *DNA Res*, 1994. **1**(1): p. 27-35.
212. Bosu, D.R. and E.T. Kipreos, *Cullin-RING ubiquitin ligases: global regulation and activation cycles*. *Cell Div*, 2008. **3**: p. 7.
213. Ponyeam, W. and T. Hagen, *Characterization of the Cullin7 E3 ubiquitin ligase--heterodimerization of cullin substrate receptors as a novel mechanism to regulate cullin E3 ligase activity*. *Cell Signal*, 2012. **24**(1): p. 290-5.
214. Litterman, N., et al., *An OBSL1-Cul7Fbxw8 ubiquitin ligase signaling mechanism regulates Golgi morphology and dendrite patterning*. *PLoS Biol*, 2011. **9**(5): p. e1001060.
215. Paradis, V., et al., *Cullin7: a new gene involved in liver carcinogenesis related to metabolic syndrome*. *Gut*, 2013. **62**(6): p. 911-9.
216. Xu, X., et al., *The CUL7 E3 ubiquitin ligase targets insulin receptor substrate 1 for ubiquitin-dependent degradation*. *Mol Cell*, 2008. **30**(4): p. 403-14.
217. Kitagawa, K. and M. Kitagawa, *The SCF-type E3 Ubiquitin Ligases as Cancer Targets*. *Curr Cancer Drug Targets*, 2016. **16**(2): p. 119-29.

References

218. Chen, P. and G.D. Yao, *The role of cullin proteins in gastric cancer*. *Tumour Biol*, 2016. **37**(1): p. 29-37.
219. Yan, J., et al., *The 3M complex maintains microtubule and genome integrity*. *Mol Cell*, 2014. **54**(5): p. 791-804.
220. Qiu, N., et al., *Cullin 7 is a predictor of poor prognosis in breast cancer patients and is involved in the proliferation and invasion of breast cancer cells by regulating the cell cycle and microtubule stability*. *Oncol Rep*, 2018. **39**(2): p. 603-610.
221. Xi, J., et al., *High Expression of Cullin7 Correlates with Unfavorable Prognosis in Epithelial Ovarian Cancer Patients*. *Cancer Invest*, 2016. **34**(3): p. 130-6.
222. Zhi, J., et al., *Support vector machine classifier for prediction of the metastasis of colorectal cancer*. *Int J Mol Med*, 2018. **41**(3): p. 1419-1426.
223. Andrews, P., Y.J. He, and Y. Xiong, *Cytoplasmic localized ubiquitin ligase cullin 7 binds to p53 and promotes cell growth by antagonizing p53 function*. *Oncogene*, 2006. **25**(33): p. 4534-48.
224. Jung, P., et al., *Induction of cullin 7 by DNA damage attenuates p53 function*. *Proc Natl Acad Sci U S A*, 2007. **104**(27): p. 11388-93.
225. Kasper, J.S., et al., *Simian virus 40 large T antigen's association with the CUL7 SCF complex contributes to cellular transformation*. *J Virol*, 2005. **79**(18): p. 11685-92.
226. Choi, B.H., et al., *WWP2 is required for normal cell cycle progression*. *Genes Cancer*, 2015. **6**(9-10): p. 371-7.
227. Clements, A.E., et al., *WWP2 and its association with PTEN in endometrial cancer*. *Gynecol Oncol Rep*, 2015. **13**: p. 26-9.
228. Fukumoto, C., et al., *WWP2 is overexpressed in human oral cancer, determining tumor size and poor prognosis in patients: downregulation of WWP2 inhibits the AKT signaling and tumor growth in mice*. *Oncoscience*, 2014. **1**(12): p. 807-20.
229. Liang, J., et al., *Expression of WW domain-containing protein 2 is correlated with pathological grade and recurrence of glioma*. *J Cancer Res Ther*, 2017. **13**(6): p. 1032-1037.
230. Soond, S.M., et al., *Novel WWP2 ubiquitin ligase isoforms as potential prognostic markers and molecular targets in cancer*. *Biochim Biophys Acta*, 2013. **1832**(12): p. 2127-35.
231. Xu, S.Q., et al., *Inhibition of WWP2 suppresses proliferation, and induces G1 cell cycle arrest and apoptosis in liver cancer cells*. *Mol Med Rep*, 2016. **13**(3): p. 2261-6.
232. Yang, R., et al., *Elevated expression of WWP2 in human lung adenocarcinoma and its effect on migration and invasion*. *Biochem Biophys Res Commun*, 2016. **479**(2): p. 146-151.
233. Maddika, S., et al., *WWP2 is an E3 ubiquitin ligase for PTEN*. *Nat Cell Biol*, 2011. **13**(6): p. 728-33.
234. Graham, E.S., et al., *Induction of Krox-24 by endogenous cannabinoid type 1 receptors in Neuro2A cells is mediated by the MEK-ERK MAPK pathway and is suppressed by the phosphatidylinositol 3-kinase pathway*. *J Biol Chem*, 2006. **281**(39): p. 29085-95.
235. Guzman, M., *Cannabinoids: potential anticancer agents*. *Nat Rev Cancer*, 2003. **3**(10): p. 745-55.
236. Tanasescu, R. and C.S. Constantinescu, *Cannabinoids and the immune system: an overview*. *Immunobiology*, 2010. **215**(8): p. 588-97.
237. Saeidnia, S., A. Manayi, and M. Abdollahi, *From in vitro Experiments to in vivo and Clinical Studies; Pros and Cons*. *Curr Drug Discov Technol*, 2015. **12**(4): p. 218-24.
238. Huh, K.W., et al., *Association of the human papillomavirus type 16 E7 oncoprotein with the 600-kDa retinoblastoma protein-associated factor, p600*. *Proc Natl Acad Sci U S A*, 2005. **102**(32): p. 11492-7.

239. DeMasi, J., et al., *Bovine papillomavirus E7 transformation function correlates with cellular p600 protein binding*. Proc Natl Acad Sci U S A, 2005. **102**(32): p. 11486-91.
240. Lefort, K. and G.P. Dotto, *Notch signaling in the integrated control of keratinocyte growth/differentiation and tumor suppression*. Semin Cancer Biol, 2004. **14**(5): p. 374-86.
241. Rangarajan, A., et al., *Notch signaling is a direct determinant of keratinocyte growth arrest and entry into differentiation*. EMBO J, 2001. **20**(13): p. 3427-36.
242. Kopan, R., *Notch signaling*. Cold Spring Harb Perspect Biol, 2012. **4**(10).
243. Siebel, C. and U. Lendahl, *Notch Signaling in Development, Tissue Homeostasis, and Disease*. Physiol Rev, 2017. **97**(4): p. 1235-1294.
244. Meyers, J.M., et al., *Cutaneous HPV8 and MmuPV1 E6 Proteins Target the NOTCH and TGF-beta Tumor Suppressors to Inhibit Differentiation and Sustain Keratinocyte Proliferation*. PLoS Pathog, 2017. **13**(1): p. e1006171.
245. Brimer, N., et al., *Cutaneous papillomavirus E6 oncoproteins associate with MAML1 to repress transactivation and NOTCH signaling*. Oncogene, 2012. **31**(43): p. 4639-46.
246. Clark, M.D., et al., *Molecular Basis for the Mechanism of Constitutive CBP/p300 Coactivator Recruitment by CRTC1-MAML2 and Its Implications in cAMP Signaling*. Biochemistry, 2015. **54**(35): p. 5439-46.
247. Zimmermann, H., et al., *Interaction with CBP/p300 enables the bovine papillomavirus type 1 E6 oncoprotein to downregulate CBP/p300-mediated transactivation by p53*. J Gen Virol, 2000. **81**(Pt 11): p. 2617-2623.
248. Ingle, A., et al., *Novel laboratory mouse papillomavirus (MusPV) infection*. Vet Pathol, 2011. **48**(2): p. 500-5.
249. Cladel, N.M., et al., *Secondary infections, expanded tissue tropism, and evidence for malignant potential in immunocompromised mice infected with Mus musculus papillomavirus 1 DNA and virus*. J Virol, 2013. **87**(16): p. 9391-5.
250. Lopez-Pajares, V., et al., *Genetic pathways in disorders of epidermal differentiation*. Trends Genet, 2013. **29**(1): p. 31-40.
251. Datto, M.B., et al., *Transforming growth factor beta induces the cyclin-dependent kinase inhibitor p21 through a p53-independent mechanism*. Proc Natl Acad Sci U S A, 1995. **92**(12): p. 5545-9.
252. Reynisdottir, I., et al., *Kip/Cip and Ink4 Cdk inhibitors cooperate to induce cell cycle arrest in response to TGF-beta*. Genes Dev, 1995. **9**(15): p. 1831-45.
253. Wang, D., et al., *Analysis of specific gene mutations in the transforming growth factor-beta signal transduction pathway in human ovarian cancer*. Cancer Res, 2000. **60**(16): p. 4507-12.
254. Qiu, W., et al., *Disruption of transforming growth factor beta-Smad signaling pathway in head and neck squamous cell carcinoma as evidenced by mutations of SMAD2 and SMAD4*. Cancer Lett, 2007. **245**(1-2): p. 163-70.
255. Fleming, N.I., et al., *SMAD2, SMAD3 and SMAD4 mutations in colorectal cancer*. Cancer Res, 2013. **73**(2): p. 725-35.
256. Valcourt, U., et al., *Analysis of Epithelial-Mesenchymal Transition Induced by Transforming Growth Factor beta*. Methods Mol Biol, 2016. **1344**: p. 147-81.
257. Mendoza, J.A., et al., *Human papillomavirus type 5 E6 oncoprotein represses the transforming growth factor beta signaling pathway by binding to SMAD3*. J Virol, 2006. **80**(24): p. 12420-4.
258. Reuven, N., M. Shanzer, and Y. Shaul, *Tyrosine phosphorylation of WW proteins*. Exp Biol Med (Maywood), 2015. **240**(3): p. 375-82.
259. Michaloglou, C., et al., *The tyrosine phosphatase PTPN14 is a negative regulator of YAP activity*. PLoS One, 2013. **8**(4): p. e61916.

References

260. Huang, J.M., et al., *YAP modifies cancer cell sensitivity to EGFR and survivin inhibitors and is negatively regulated by the non-receptor type protein tyrosine phosphatase 14*. *Oncogene*, 2013. **32**(17): p. 2220-9.
261. Poernbacher, I., et al., *Drosophila Pez acts in Hippo signaling to restrict intestinal stem cell proliferation*. *Curr Biol*, 2012. **22**(5): p. 389-96.
262. Yun, H.Y., et al., *Structural basis for recognition of the tumor suppressor protein PTPN14 by the oncoprotein E7 of human papillomavirus*. *PLoS Biol*, 2019. **17**(7): p. e3000367.
263. Boggiano, J.C., P.J. Vanderzalm, and R.G. Fehon, *Tao-1 phosphorylates Hippo/MST kinases to regulate the Hippo-Salvador-Warts tumor suppressor pathway*. *Dev Cell*, 2011. **21**(5): p. 888-95.
264. Oka, T., V. Mazack, and M. Sudol, *Mst2 and Lats kinases regulate apoptotic function of Yes kinase-associated protein (YAP)*. *J Biol Chem*, 2008. **283**(41): p. 27534-27546.
265. Ni, L., et al., *Structural basis for Mob1-dependent activation of the core Mst-Lats kinase cascade in Hippo signaling*. *Genes Dev*, 2015. **29**(13): p. 1416-31.
266. Zhao, B., et al., *The Hippo-YAP pathway in organ size control and tumorigenesis: an updated version*. *Genes Dev*, 2010. **24**(9): p. 862-74.
267. Zhao, B., et al., *A coordinated phosphorylation by Lats and CK1 regulates YAP stability through SCF(beta-TRCP)*. *Genes Dev*, 2010. **24**(1): p. 72-85.
268. Guo, T., et al., *A novel partner of Scalloped regulates Hippo signaling via antagonizing Scalloped-Yorkie activity*. *Cell Res*, 2013. **23**(10): p. 1201-14.
269. Koontz, L.M., et al., *The Hippo effector Yorkie controls normal tissue growth by antagonizing scalloped-mediated default repression*. *Dev Cell*, 2013. **25**(4): p. 388-401.
270. Zhao, B., et al., *TEAD mediates YAP-dependent gene induction and growth control*. *Genes Dev*, 2008. **22**(14): p. 1962-71.
271. White, E.A., K. Munger, and P.M. Howley, *High-Risk Human Papillomavirus E7 Proteins Target PTPN14 for Degradation*. *mBio*, 2016. **7**(5).
272. Sanchez-Vega, F., et al., *Oncogenic Signaling Pathways in The Cancer Genome Atlas*. *Cell*, 2018. **173**(2): p. 321-337 e10.
273. Szalmas, A., et al., *The PTPN14 Tumor Suppressor Is a Degradation Target of Human Papillomavirus E7*. *J Virol*, 2017. **91**(7).
274. Hong, W. and K.L. Guan, *The YAP and TAZ transcription co-activators: key downstream effectors of the mammalian Hippo pathway*. *Semin Cell Dev Biol*, 2012. **23**(7): p. 785-93.
275. Zanconato, F., M. Cordenonsi, and S. Piccolo, *YAP/TAZ at the Roots of Cancer*. *Cancer Cell*, 2016. **29**(6): p. 783-803.
276. Liu, H., et al., *The Hippo pathway regulates stem cell proliferation, self-renewal, and differentiation*. *Protein Cell*, 2012. **3**(4): p. 291-304.
277. Moya, I.M. and G. Halder, *Hippo-YAP/TAZ signalling in organ regeneration and regenerative medicine*. *Nat Rev Mol Cell Biol*, 2019. **20**(4): p. 211-226.
278. Azzolin, L., et al., *YAP/TAZ incorporation in the beta-catenin destruction complex orchestrates the Wnt response*. *Cell*, 2014. **158**(1): p. 157-70.
279. Cai, J., et al., *The Hippo signaling pathway restricts the oncogenic potential of an intestinal regeneration program*. *Genes Dev*, 2010. **24**(21): p. 2383-8.
280. Gregorieff, A., et al., *Yap-dependent reprogramming of Lgr5(+) stem cells drives intestinal regeneration and cancer*. *Nature*, 2015. **526**(7575): p. 715-8.
281. Zanconato, F., et al., *Genome-wide association between YAP/TAZ/TEAD and AP-1 at enhancers drives oncogenic growth*. *Nat Cell Biol*, 2015. **17**(9): p. 1218-27.
282. Lei, Q.Y., et al., *TAZ promotes cell proliferation and epithelial-mesenchymal transition and is inhibited by the hippo pathway*. *Mol Cell Biol*, 2008. **28**(7): p. 2426-36.

283. Overholtzer, M., et al., *Transforming properties of YAP, a candidate oncogene on the chromosome 11q22 amplicon*. Proc Natl Acad Sci U S A, 2006. **103**(33): p. 12405-10.
284. Shao, D.D., et al., *KRAS and YAP1 converge to regulate EMT and tumor survival*. Cell, 2014. **158**(1): p. 171-84.
285. Astone, M., et al., *Zebrafish mutants and TEAD reporters reveal essential functions for Yap and Taz in posterior cardinal vein development*. Sci Rep, 2018. **8**(1): p. 10189.
286. Chen, Z., G.A. Friedrich, and P. Soriano, *Transcriptional enhancer factor 1 disruption by a retroviral gene trap leads to heart defects and embryonic lethality in mice*. Genes Dev, 1994. **8**(19): p. 2293-301.
287. Kim, J., et al., *YAP/TAZ regulates sprouting angiogenesis and vascular barrier maturation*. J Clin Invest, 2017. **127**(9): p. 3441-3461.
288. Murakami, M., et al., *A WW domain protein TAZ is a critical coactivator for TBX5, a transcription factor implicated in Holt-Oram syndrome*. Proc Natl Acad Sci U S A, 2005. **102**(50): p. 18034-9.
289. Wang, J., et al., *The Hippo pathway in the heart: pivotal roles in development, disease, and regeneration*. Nat Rev Cardiol, 2018. **15**(11): p. 672-684.
290. Wang, X., et al., *YAP/TAZ Orchestrate VEGF Signaling during Developmental Angiogenesis*. Dev Cell, 2017. **42**(5): p. 462-478 e7.
291. Plouffe, S.W., et al., *The Hippo pathway effector proteins YAP and TAZ have both distinct and overlapping functions in the cell*. J Biol Chem, 2018. **293**(28): p. 11230-11240.
292. Wang, H., et al., *Distinct and Overlapping Roles of Hippo Effectors YAP and TAZ During Human and Mouse Hepatocarcinogenesis*. Cell Mol Gastroenterol Hepatol, 2021. **11**(4): p. 1095-1117.
293. Pocaterra, A., P. Romani, and S. Dupont, *YAP/TAZ functions and their regulation at a glance*. J Cell Sci, 2020. **133**(2).
294. Beverdam, A., et al., *Yap controls stem/progenitor cell proliferation in the mouse postnatal epidermis*. J Invest Dermatol, 2013. **133**(6): p. 1497-505.
295. Elbediwy, A. and B.J. Thompson, *Evolution of mechanotransduction via YAP/TAZ in animal epithelia*. Curr Opin Cell Biol, 2018. **51**: p. 117-123.
296. Schlegelmilch, K., et al., *Yap1 acts downstream of alpha-catenin to control epidermal proliferation*. Cell, 2011. **144**(5): p. 782-95.
297. Totaro, A., et al., *YAP/TAZ link cell mechanics to Notch signalling to control epidermal stem cell fate*. Nat Commun, 2017. **8**: p. 15206.
298. Yuan, Y., et al., *YAP1/TAZ-TEAD transcriptional networks maintain skin homeostasis by regulating cell proliferation and limiting KLF4 activity*. Nat Commun, 2020. **11**(1): p. 1472.
299. Zhang, H., H.A. Pasolli, and E. Fuchs, *Yes-associated protein (YAP) transcriptional coactivator functions in balancing growth and differentiation in skin*. Proc Natl Acad Sci U S A, 2011. **108**(6): p. 2270-5.
300. Boon, S.S. and L. Banks, *High-risk human papillomavirus E6 oncoproteins interact with 14-3-3zeta in a PDZ binding motif-dependent manner*. J Virol, 2013. **87**(3): p. 1586-95.
301. Olmedo-Nieva, L., et al., *New insights in Hippo signalling alteration in human papillomavirus-related cancers*. Cell Signal, 2020. **76**: p. 109815.
302. Yuspa, S.H. and D.L. Morgan, *Mouse skin cells resistant to terminal differentiation associated with initiation of carcinogenesis*. Nature, 1981. **293**(5827): p. 72-4.
303. Tyanova, S., et al., *The Perseus computational platform for comprehensive analysis of (prote)omics data*. Nat Methods, 2016. **13**(9): p. 731-40.
304. Macville, M., et al., *Comprehensive and definitive molecular cytogenetic characterization of HeLa cells by spectral karyotyping*. Cancer Res, 1999. **59**(1): p. 141-50.

Abbreviation

305. Dingar, D., et al., *BioID identifies novel c-MYC interacting partners in cultured cells and xenograft tumors*. J Proteomics, 2015. **118**: p. 95-111.

13 Abbreviation

PV	Papillomavirus
HPV	human Papillomavirus
SCC	squamous cell carcinoma
EV	<i>Epidermodysplasia verruciformis</i>
URR	upstream regulatory region
K10	keratin 10
K14	keratin 14
HSPG	heparan sulphate proteoglycan
CR	conserved region
TM	transmembrane domain
CKII	Casein kinase II
IL-1 β	Interleukin 1 beta
UV	ultra violett
Rb	retinoblastoma protein
CER	complete early genomic region
NMSC	non-melanoma skin cancer
BCC	basal cell carcinomas
AK	actinic keratosis
MnPV	<i>Mastomys natalensis</i> papillomavirus
KSCC	keratinized squamous cell carcinoma
nKSCC	non-keratinized squamous cell carcinoma
FFPE	Formalin-fixed paraffin-embedded
PCA	Principal component analysis
FDR	false discovery rate
LFQ	label free quantification
IPA	Ingenuity Pathway Analysis
mTORC1	mTOR complex 1
mTORC2	mTOR complex 2
RNA	ribonucleic acid
Cav1	caveolin
IF	immunofluorescence
ISH	<i>In-situ</i> hybridization
WB	western blot
iBAQ	Intensity-based absolute quantification
MAP4K1/ HPK1	Mitogen-activated protein kinase kinase kinase kinase 1
Cul7	Cullin7

NOK	normal oral keratinocytes
MS	mass spectrometry
IP	immunoprecipitation
MaFi132	<i>Mastomys</i> fibroblasts 132
MaFi191	<i>Mastomys</i> fibroblasts 191
SNRPD1	small nuclear ribonucleoprotein Sm D1
GST	Glutathione S-transferase
HNSCC	head and neck squamous cell carcinoma
MAML1	Mastermind-like protein 1
PTPN14	Tyrosine-protein phosphatase non-receptor type 14
FC	fold change
MST1	mammalian STE20-like protein kinase 1
LATS1	large tumor suppressor 1
SAV1	Salvador homologue 1
MOB1A	MOB kinase activator 1A
YAP	Yes-associated protein
TAZ	Transcriptional co-activator with PDZ-binding motif
TEADs	TEA domain family members
PCR	Polymerase chain reaction
FBS	Fetal Bovine Serum
EDTA	Ethylenediaminetetraacetic acid
rpm	revolutions per minute
PBS	Phosphate-buffered saline
PEI	polyethylenimine
DNA	Deoxyribonucleic acid
RT	Reverse transcriptase
BSA	Bovine serum albumin
MEM	Minimal Essential Medium
TCEP	tris(2-carboxyethyl)phosphine
CAA	chloroacetamide
ABC	ammonium bicarbonate
CPB	cycles per burst
DF	duty factor
PIP	peak incidence power
AFA	adaptive focused acoustics
PIC	protease inhibitor cocktail
ACN	acetonitrile
TFA	trifluoro acetic acid
GS	goat serum
RT	room temperature
TEMED	Tetramethylethylenediamine
SDS	Sodium dodecyl sulfate
HRP	horseradish peroxidase

14 Danksagungen

Zunächst möchte ich mich herzlich bei Herrn Frank Rösl bedanken, der es mir ermöglichte, sowohl meine Masterarbeit als auch diese Doktorarbeit in seiner Arbeitsgruppe zu verfassen. Vielen Dank für das entgegengebrachte Vertrauen.

Ich danke meinen TAC-Mitgliedern Martin Müller und Baki Akgül für ihre wertvollen Beiträge in meinen TAC-Sitzungen.

Danke auch an die Mitglieder meines Verteidigungsausschusses, Ralf Bartenschlager und Karin Müller-Decker für ihr Interesse an meiner Arbeit und ihr freundliches Entgegenkommen während der Organisation der Verteidigung dieser Arbeit.

Danke an Daniel Hasche, der es mir durch seinen Einsatz ermöglichte, meine Doktorarbeit im Bereich der Hautkrebsforschung zu absolvieren.

Ein besonderer Dank gilt auch Martina Niebler, für die maßgebliche und hilfreiche Unterstützung während der gesamten Doktorarbeit. Danke, für Primer, Vektoren, Zellen, Rat und Tat und gute Worte, wann immer sie nötig waren.

Danke auch an meine PhD Kollegen, Rui, Ruwen, Melinda, Stefan und Katrin für die moralische Unterstützung und ihre große Hilfsbereitschaft.

Ein herzlicher Dank geht an Ilona, Sonja, Regina und Georg für die Geduld, die vielen Tipps und Tricks und ganz besonders die gemeinsame Zeit.

Außerdem möchte ich mich bei Diana Schalk bedanken für die Unterstützung im administrativen Bereich.

Ich wünsche Euch allen für die Zukunft nur das Allerbeste!

Nun zu den wichtigsten Menschen in meinem Leben.

Matthias, danke, dass du so bist, wie du bist. Danke für all die vielen Male, die du mich zum Lachen gebracht hast, obwohl mir zum Schreien zumute war. Danke für deine Unterstützung in so vielen Bereichen. Ich bin glücklich, dich an meiner Seite zu wissen und kann mit Überzeugung sagen: „Dich kennen zu lernen war das Beste in dieser ganzen Zeit!“ Ich liebe dich!

Mama, danke dass du immer da bist, wenn ich dich brauche und dafür, dass ich mit allen Sorgen und Freuden jeder Zeit zu dir kommen kann. Papa, danke, dass du der Mensch warst, der du warst. Du hast mich zu der mutigen, wissbegierigen und manchmal starrköpfigen Persönlichkeit gemacht, die ich heute bin. Dafür danke ich dir von Herzen! Ich hab' euch lieb!